On Stability and Surge in Turbocharger Compressors

BERTRAND KERRES

Doctoral Thesis
Stockholm, Sweden, 2017

TRITA MMK 2017:08
ISSN 1400-1179
ISRN KTH/MMK/R--17/08--SE
ISBN 978-91-7729-378-1

KTH School of Industrial Engineering and Management
SE-100 44 Stockholm
SWEDEN

Akademisk avhandling som med tillstånd av Kungl Tekniska högskolan framlägges till offentlig granskning för avläggande av teknologie doktorsexamen i maskinkonstruktion den 2 juni 2017, kl. 10:00 i D1, Lindstedtsvägen 17, Stockholm.

© Bertrand Kerres, 2017-06-02

Tryck: Universitetsservice US AB

Abstract

Turbochargers are used on many automotive internal combustion engines to increase power density. The broad operating range of the engine also requires a wide range of the turbocharger compressor. At low mass flows, however, turbo compressor operation becomes unstable and eventually enters surge. Surge is characterized by large oscillations in mass flow and pressure. Due to the associated noise, control problems, and possibility of mechanical component damage, this has to be avoided.

Different indicators exist to classify compressor operation as stable or unstable on a gas stand. They are based on pressure oscillations, speed oscillations, or inlet temperature increase. In this thesis, a new stability indicator is proposed based on the Hurst exponent of the pressure signal. The Hurst exponent is a number between zero and one that describes what kind of long-term correlations are present in a time series.

Data from three cold gas stand experiments are analyzed using this criterion. Results show that the Hurst exponent of the compressor outlet pressure signal has good characteristics. Stable operation is being indicated by values larger than 0.5. As compressor operation moves towards the surge line, the Hurst exponent decreases towards zero. An additional distinction between the long-term correlations of small and large amplitude fluctuations by means of higher order Hurst exponents can be used as an early warning indicator.

Further tests using compressor housing accelerometers show that the Hurst exponent is not a good choice for real-time surge detection on the engine. Reasons are the long required sampling time compared to competing methods, and the fact that other periodically repeating oscillations lead to Hurst exponents close to zero independent of compressor operation.

Sammanfattning

Turboladdare används ofta på förbränningsmotorer för att öka motorns effekttäthet. Motorns breda driftområde ställer krav på ett brett driftområde för turboladdarens kompressor. Vid låga massflöden blir kompressordriften dock mindre stabil, och surge kan uppträda. Surge innebär stora oscillationer i tryck och massflöde genom kompressorn. På grund av oljud, reglerproblem och risken för mekaniska skador vill man undvika surge.
Det finns indikatorer för att bedöma kompressorns stabilitet på ett gas stand. Indikatorerna är baserade på tryckoscillationer, varvtalsoscillationer, eller temperaturökning i gasen i kompressorinloppet. I denna avhandling presenteras en ny indikator baserad på Hurst-exponenten, beräknad på trycksignalen. Hurst-exponenten är ett tal mellan noll och ett som beskriver vilka typer av långtidskorrelationer det finns i signalen.
Mätningar från tre gas-stand-experiment har analyserats på detta sätt. Analyserna visar att Hurst-exponenten baserad på kompressorutloppstrycket fungerar bra som som surgeindikator. Stabil drift av kompressorn indikeras av att Hurst-exponenten är större än 0.5. När kompressordriftpunkten närmar sig surgelinjen faller Hurst-exponenten mot noll. En distinktion mellan oscillationer med små och stora amplituder kan används för att få en tidig varning.
Analyser av vibrationsmätningar på kompressorhuset vid motorapplikation visar att Hurst-exponenten inte är lämplig som realtidsindikator på en motor. Detta kommer sig dels av att data behöver samlas in under en längre tid än med andra tänkbara indikatorer, dels av att andra periodiska oscillationer i signalen kopplade till motorns naturliga beteende leder till Hurst-exponenter nära noll även vid stabil kompressordrift.

Preface

This doctoral thesis describes the results of my studies at the KTH Royal Institute of Technology. They were carried out as member of the Compressor off-Design research group within the Competence Center for Gas Exchange (CCGEx) from 2013 to 2017. The thesis is divided into two parts: The first part describes the motivation, gives an overview over relevant literature, and summarizes the results of my own studies. The second part consists of the collected papers and manuscripts that were created during this time.

I would like to thank my supervisors, Andreas Cronhjort and Mihai Mihaescu, for their guidance, support, and trust in me. Many thanks also to Nils Tillmark, former head of the KTH CICERO lab, for his help with performing the experiments, and the workshop team of Tomas Östberg, Jack Ivarsson, Kim Karlström, Jonas Vikström, and Rune Lindfors for their able help. Last but not least, thank you to all former colleagues for making the work environment so enjoyable.

Stockholm, May 2017
Bertrand Kerres

Contents

1 Introduction **1**
- 1.1 Charging the internal combustion engine . . . 2
- 1.2 Research questions and thesis outline . . . 5

2 Radial compressors **9**
- 2.1 Principle of operation . . . 9
  - 2.1.1 Classification of fluid machinery . . . 9
  - 2.1.2 Compressor characteristics . . . 10
  - 2.1.3 Work input . . . 13
  - 2.1.4 Loss mechanisms . . . 15
- 2.2 Description of the flow field . . . 18
  - 2.2.1 Impeller flow field . . . 18
  - 2.2.2 Vaneless diffuser flow field . . . 20
  - 2.2.3 Volute flow field . . . 20
- 2.3 Operating range and instabilities . . . 22
  - 2.3.1 Stall and rotating stall . . . 22
  - 2.3.2 Compressor surge . . . 24
  - 2.3.3 Modeling of compressor destabilization at off-design . . . 29
  - 2.3.4 Stability indicators . . . 35

3 Fractals and the Hurst exponent **41**
- 3.1 Fractals and self-similarity . . . 41
  - 3.1.1 Fractal dimensions and scaling laws . . . 41
  - 3.1.2 Self-similarity, self-affinity, and the Hurst exponent . . . 43
- 3.2 Estimating the Hurst exponent . . . 43
  - 3.2.1 Rescaled range approach . . . 44
  - 3.2.2 Detrended fluctuation analysis . . . 45
  - 3.2.3 Relation to spectral estimates . . . 47
  - 3.2.4 Multifractal detrended fluctuation analysis . . . 48
- 3.3 A note on the performance of the algorithm . . . 49
- 3.4 The Hurst exponent in mechanical engineering applications . . . 51
- 3.5 Application of the Hurst exponent as surge indicator . . . 51

4 Experimental setup **53**
4.1 The cold gas stand . . . 53
4.1.1 The CICERO lab . . . 53
4.1.2 The turbocharger . . . 54
4.2 Instrumentation and measurement . . . 55
4.2.1 Sensors and positioning . . . 55
4.2.2 Data acquisition . . . 56
4.2.3 Measurement accuracy and repeatability . . . 57

5 Results and discussion **59**
5.1 Verification . . . 59
5.1.1 The Hurst exponent as surge indicator . . . 59
5.1.2 Mono- and multifractality near surge . . . 62
5.2 Validation . . . 64
5.2.1 Benchmarking and sensor positioning . . . 65
5.2.2 Sampling frequency . . . 68
5.3 Application . . . 68
5.3.1 Analyzing a compressor map . . . 68
5.3.2 Bend positioning at the compressor inlet . . . 70
5.3.3 On-engine application . . . 72
5.4 Summary of the advantages and drawbacks . . . 75

6 Conclusions and future work **77**

7 Appended papers and authors' contributions **81**

Abbreviations and symbols **85**

Bibliography **93**

A DFA Performance **105**

B Errata **109**

1 Introduction

The internal combustion engine is the dominant propulsion system for street bound goods and passenger transport. Of all 372,318 newly registered passenger cars in Sweden in 2016, 93.7% are propelled by a combustion engine only, and a further 5.5% use a combustion engine as part of a hybrid powertrain. In addition, 58,167 trucks and 1,333 buses were newly registered, essentially all of them employing a combustion engine [BIL Sweden, 2017]. In the whole European Union (EU), this ratio is even more lopsided, with 97.1% of all newly registered cars having a combustion engine only, and 99.6% having a combustion engine as part of the powertrain [ACEA, 2017b, ACEA, 2017a]. Although the share of electrified passenger cars is predicted to increase significantly, it is expected that an internal combustion engine will be part of almost all new vehicles for the foreseeable future [KPMG, 2017].
The combustion engine has been around for more than a century. This has lead to a mature technology, a well-developed supporting infrastructure, and high social acceptance. Its enduring popularity is intimately connected to the fuels, mainly Diesel and gasoline. They can be refined from crude oil and have a very high energy density compared to electric energy storages. The combustion of these fossil fuels has negative ramifications, however: One of the main combustion products, carbon dioxide (CO_2), is a potent greenhouse gas. Other byproducts of the combustion process, such as nitrogen oxides (NO_x), soot and other particulate matter, carbon monoxide (CO), and unburned hydrocarbon chains, are hazardous for human and animal life. Another concern is the noise generated by combustion engines. Since these costs are not only born by the car operator, but by bystanders as well, they can be considered negative externalities.

Different approaches are employed by the governing bodies to limit the production of these externalities. CO_2 formation is a direct consequence of the combustion of hydrocarbons and can thus be internalized – the producer can be made to pay for them – by taxes on fuel. In the EU, additional limits are mandated for the fleet average of all large passenger car manufacturers, with penalties to be paid in case of exceeding these limits. Since 2015, the limit is 130 g/km in the New European Driving Cycle. The value is set to decrease to 95 g/km in 2021 [European Commission, 2017].
The hazardous byproducts collectively go under the name "emissions", although

CO_2 and noise are of course also emitted in the physical sense. Since the amount of emissions is not measured during driving, and thus the real driving emissions are not known, they cannot easily be internalized. The EU tries to deal with this problem by mandating maximum emission levels in the respective light and heavy duty standardized driving cycles. The current (2017) set of emission standards are called EURO 6 for light duty vehicles and EURO VI for heavy duty vehicles, respectively. Noise emission of vehicles is also legislated on EU level by imposing a maximum sound pressure level for drive-by at constant speed.

In Diesel engine operation, addressing one of these issues often has a negative effect on the other ones. For example, a very fast combustion when the piston is in top dead center position is efficient from a thermodynamic perspective, since the heat is added at high temperatures. It further helps the oxidation of soot particles. On the other hand, the fast pressure increase creates loud combustion noise, and high temperatures in combination with excess air lead to the formation of NO_x.
The combination of charging the engine, together with an intercooler, is attractive because it can help alleviating several issues [Pischinger, 2013b]. The high cylinder charge and pressure contribute to low soot emissions. The intercooler decreases charge temperature, which results in lower NO_x formation. Charging the engine in combination with a decrease in engine size, the so-called downsizing, can also improve fuel efficiency and thus CO_2 emissions. The fundamentals of engine charging are summarized in the next section.

1.1 Charging the internal combustion engine

Engine load is commonly expressed using mean effective pressures, which are work per swept volume. The work extracted per cylinder swept volume from the piston over the compression and expansion strokes – the High Pressure (HP) cycle – is called gross Indicated Mean Effective Pressure (IMEP). The same calculation over the intake and exhaust strokes – the Low Pressure (LP) cycle – gives the Pump Mean Effective Pressure (PMEP), p_{mp}. It is negative for naturally aspirated engines, but can be positive for supercharged ones. The sum of gross IMEP and PMEP is the indicated pressure over the whole cycle, the net IMEP. The definitions are thus

$$p_{\mathrm{mi,gr}} = \frac{\oint_{\mathrm{HP}} (p_{\mathrm{cyl}} - p_{\mathrm{cc}}) \mathrm{d}V}{V_{\mathrm{sw}}} \tag{1.1}$$

$$p_{\mathrm{mp}} = \frac{\oint_{\mathrm{LP}} (p_{\mathrm{cyl}} - p_{\mathrm{cc}}) \mathrm{d}V}{V_{\mathrm{sw}}} \tag{1.2}$$

$$p_{\mathrm{mi,net}} = p_{\mathrm{mi,gr}} + p_{\mathrm{mp}} \tag{1.3}$$

where $(p_{\mathrm{cyl}} - p_{\mathrm{cc}})$ is the net pressure acting on the piston and V_{sw} is the swept volume. These pressures are used to characterize the thermodynamic and fluid dynamic performance of the combustion and gas exchange systems. Figure 1.1 schematically

shows a $p-V$ diagram for a naturally aspirated engine. The shaded areas represent the work of the respective cycle. Also marked are the crankcase pressure p_{cc}, the intake manifold pressure p_{int} and the exhaust system backpressure p_{exh}. Other

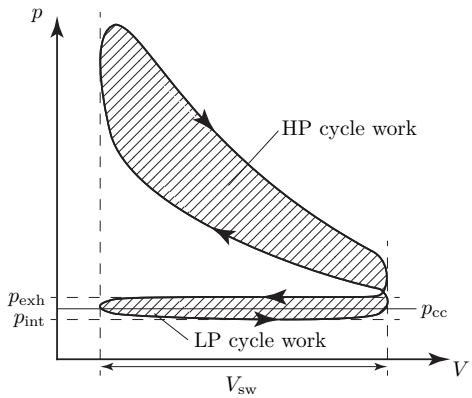

Figure 1.1: $p-V$ diagram showing the piston work of the HP and LP cycle as shaded areas.

mechanical losses in the engine, such as friction and the power needed to drive auxiliary devices, are summarized in the Friction Mean Effective Pressure (FMEP), p_{mf}. The friction work is difficult to measure directly, and is instead calculated as the difference between the net indicated work as calculated from cylinder pressures, and the work available at the brake:

$$p_{\mathrm{me}} = \frac{W_{\mathrm{e}}}{z_{\mathrm{cyl}} V_{\mathrm{sw}}} = \frac{\dot{W}_{\mathrm{e}}}{\frac{1}{2} n_{\mathrm{eng}} z_{\mathrm{cyl}} V_{\mathrm{sw}}} \tag{1.4}$$

$$p_{\mathrm{mf}} = p_{\mathrm{me}} - p_{\mathrm{mi,net}} \tag{1.5}$$

where z_{cyl} is the number of cylinders, n_{eng} is the crankshaft speed in revolutions per time, and the factor 1/2 is due to the fact that four-stroke engine cylinders have one power stroke per two revolutions. As a simple approximation, FMEP can be considered independent of load for a given engine [Pischinger, 2013a].
From Eq. (1.4), one can see that there are in principle three ways to increase engine power output: increase the engine speed, increase the cylinder volume or the number of cylinders, or increase the brake mean effective pressure. For spark-ignited engines, limits for increasing the engine speed are mainly determined by the mechanical stresses. They scale with the square of the engine speed [Pischinger, 2013b]. Compression-ignited engines are also limited to lower speeds by the ignition delay and the higher oscillating masses. Increasing the swept volume avoids these drawbacks, but leads to heavier and larger engines. A large engine will furthermore operate at very low IMEP when the torque demand is low. With FMEP constant, the mechanical efficiency – the ratio of BMEP to IMEP – will decrease.

Increasing IMEP is therefore an attractive way to increase the power output of an engine. The most obvious way to increase IMEP is to combust more fuel per cycle. The fuel mass that can be burned, however, is limited by the amount of oxygen available for combustion. Supplying the air demand is the task of the boosting system. From the state equation for ideal gases,

$$\rho = \frac{p}{RT} \ , \tag{1.6}$$

with ρ as density and R as specific gas constant, it can be seen that the density can be increased by increasing the pressure and by reducing the temperature at the inlet side. Engine boosting systems normally first increase the air pressure applying one or several supercharging devices. This also increases air temperature. Most of the excess air temperature is then removed using a charge air cooler.
Using the increased amount of air to combust more fuel leads to a higher specific power output of the engine, i.e. power output per swept volume. Thus, a smaller supercharged engine can deliver the same power as a larger, naturally aspirated one. Decreasing the swept volume while keeping the power approximately constant with the help of a boosting system is called downsizing, and one of the most popular concepts to increase efficiency at part load. These gains mainly come in two ways: The first one is the approximately constant FMEP, see above. For the same torque demand, a small engine will operate at higher BMEP, and thus the relative importance of friction decreases. The second way can be a reduction in pump losses, or even a positive PMEP.

The common power sources to drive the supercharging device are the crankshaft and the exhaust gas enthalpy flow. If the power is taken from the crankshaft, the supercharging device is a "mechanical supercharger", often just called a "supercharger". Mechanical superchargers exist in many different forms; the most common for automotive applications is the Roots blower. Since they are connected directly to the crankshaft, their speed is directly proportional to the engine speed. This results in a very fast response to transient load increases. At high engine speeds, they are often decoupled, since their power consumption would be very high. Mechanical superchargers improve PMEP, since the cylinder pressure during the intake stroke is increased without a corresponding penalty during the exhaust stroke. On the other hand, the driving torque for the supercharger reduces the available net torque on the crankshaft. This is accounted for through an increase in FMEP, using the budgeting described above.
The alternative to using crankshaft power for a mechanical supercharger, and much more popular today, is the exhaust gas turbocharger. It consists of a turbine driven by the exhaust gas flow and a turbo compressor in the intake system, mounted on a common shaft. Their speed is therefore not directly related to the engine speed, but a result of the difference in driving torque on the turbine side and resisting torque on the compressor side. This leads to a relatively slow response to engine load changes. The big advantage of turbochargers is their utilization of the exhaust gas enthalpy.

At high engine loads, this would otherwise be wasted, since the cylinder pressure at the exhaust valve opening is still significantly higher than the backpressure of the exhaust gas aftertreatment system. In these load cases, a positive PMEP is possible even with a turbocharger. At low loads, on the other hand, the flow resistance of the turbine has to be overcome by piston work during the exhaust stroke, and the effect on pump work is negative.

1.2 Research questions and thesis outline

In automotive applications, engines are typically operated over a wide range of speeds and loads. This in turn creates operating range requirements for the turbocharger compressor. In this thesis, only compressor operation is dealt with. When designing a turbo compressor, mass flow and compressor speed must be stipulated in order to estimate local flow conditions. The geometric design features of the compressor, such as blade angles and volute sizing, can then be chosen according to the flow conditions for this design operating point. Compressor operation at other combinations of mass flow and compressor speed is called "off-design operation", and is the common operation for turbocharger compressors in automotive applications. Besides a degradation in efficiency at off-design, compressor operation is limited by choked flow at high mass flows, and by unstable operation at low mass flows, called "compressor surge". These compressor operation limits influence the operational limits of the engine itself.

Given the frequent compressor operation at off-design in automotive turbochargers, some research objectives have been formulated for this thesis. The main objective is to introduce a new stability indicator, the Hurst exponent (see chapter 3), for turbocharger compressors. The motivation for these research questions lies in the different definitions of the surge line used in technical standards, and by turbocharger suppliers. It will be outlined in more detail in Section 2.3.4. The research questions concerned with the verification and validation of this method are as follows:

1.1 Can the Hurst exponent be used as an indicator of system stability on a gas stand?

1.2 Do the Hurst exponents indicating stability/instability differ significantly between different compression systems?

1.3 Can different orders of the Hurst exponent be used as a precursor to compressor surge?

These research questions are investigated in papers I, II, and III.

Following the verification and validation, the application of the method is tested on an engine for real-time surge detection. Possible benefits from a better real-time surge detection on-engine accrue due to the safety margin towards surge that is kept

in engine calibration. Figure 1.2 schematically depicts limitations to the maximum engine BMEP, the full load curve. A minimum air-fuel ratio needs to be maintained in order to keep engine-out soot emissions within limits. At low engine speeds, the charge air mass is limited by compressor surge. The maximum fuel injection amount is then proportional to the air mass, and BMEP approximately proportional to the fuel mass injected. Thus, reducing the safety margin improves low end torque and therefore the possible acceleration of the vehicle. Alternatively, one can use the increased BMEP to lower the gear ratios of the transmission while keeping vehicle acceleration similar. This lowers the vehicle fuel consumption.

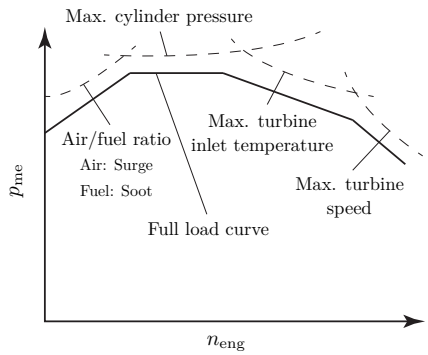

Figure 1.2: Limitations to engine BMEP imposed by different components, adapted from [Watson and Janota, 1982].

The related research question is

2.1 Can the Hurst exponent be used for on-engine surge detection?

The investigation into surge detection on the engine is summarized in paper IV. In contrast to the validation studies which were done with pressure sensors, knock accelerometers were used due to their low cost.

Research questions 1.1 to 1.3, as well as 2.1, form the core part of this thesis and will also mainly be dealt with on the summary part of this thesis. In addition to these investigations, other research related to turbocharger compressor operation at off-design has been performed. Two research questions are concerned with the difference in compressor operating range and performance between different inlet configurations:

3.1 How does a bend at the inlet change compressor operation compared to a straight inlet pipe?

3.2 How does the relative circumferential positioning of a bend at the inlet influence stability at low mass flows?

The interest in this question stems mainly from the fact that turbocharger performance is measured on a gas stand with long straight inlet pipes, while in application as part of an engine boosting system, the packaging constraints determine the possible inlet configurations. The result of the investigation is summarized in Section 5.3.2 and described in paper V.
Other research questions consider the use of lower order models to predict compressor performance. Due to their low computational cost, these models are popular in early design phases for the compressor, as well as when analyzing the compressor as part of a larger system such as the engine boosting system. The corresponding research questions are:

4.1 What is the accuracy penalty compared to 3D Reynols-Averaged Navier-Stokes (RANS) computations in different compressor operating points?

4.2 Can the different model loss terms be evaluated by means of comparison with the RANS computational data?

Papers VII, VI, and VIII summarize the results from the investigation of research questions 4.1 and 4.2. Some of the results are also used in Section 2.3.3.

The summary of the thesis is built up as follows: In chapter 2, the principles of radial compressors are described. A special focus is put on their range and instabilities at low mass flows, and surge indicators given in literature. In Chapter 3, the Hurst exponent and different methods to estimate it are explained. Chapter 4 describes the experimental setup used for those experiments that were performed by myself. The results from the investigations of research questions 1.1 to 2.1 are summarized in Chapter 5. The investigation is concluded and interesting questions for future work are outlined in Chapter 6.

2 Radial compressors

2.1 Principle of operation

2.1.1 Classification of fluid machinery

Compressors use mechanical work to increase the pressure of a compressible working fluid. This distinguishes them from pumps, where the working fluid is approximately incompressible. Both pumps and compressors can furthermore be divided with respect to their working principle into positive displacement machinery and turbomachinery.
In positive displacement pumps and compressors, the static pressure of the working fluid is increased directly via displacement, e.g. through a piston. The fluid is (nearly) at rest during this process. In turbomachinery, on the other hand, the static pressure is increased by indirect means: Moving blades accelerate the flow, thus increasing its dynamic and total pressure. The flow is then decelerated in a diffuser, where the dynamic pressure is converted into static pressure. Table 2.1 from [Eckert and Schnell, 1961] summarizes this classification.

—	incompressible	compressible
positive displacement	piston pump	piston compressor Roots compressor
turbomachinery	centrifugal pump	axial compressor radial compressor

Table 2.1: Classification of fluid machinery

Two very common types of turbo compressors are axial compressors and radial (also called centrifugal) compressors. The description axial or radial refers to the direction of the outflow of the compressor.
In the following, the operation of turbo compressors will be described in more detail. The current section 2.1 on the principle of operation is written in relatively general terms and approximately valid for both radial and axial compressors. Since compressors used as part of turbochargers are most commonly radial compressors, the remaining sections in this chapter will focus on radial compressors exclusively.

2.1.2 Compressor characteristics

In this part, some important compressor characteristics will be defined.
The main objective of using a compressor is to increase the pressure of the fluid by adding energy. An important parameter is therefore the work coefficient ψ. It relates the stagnation enthalpy increase Δh_t of the fluid to the blade tip speed u,

$$\psi = \frac{\Delta h_t}{u^2} \ . \tag{2.1}$$

If the fluid is assumed to be incompressible. this can be rewritten using $\Delta h = \Delta p/\rho$ as

$$\psi = \frac{\Delta p}{\rho u^2} \ . \tag{2.2}$$

From an operational perspective, the increase in pressure is often expressed through the pressure ratio

$$\mathrm{PR} = \frac{p_{\mathrm{out}}}{p_{\mathrm{in}}} \ . \tag{2.3}$$

If inlet and outlet pressure are total pressures, the pressure ratio is qualified as Total Pressure Ratio (TPR). It is commonly used if the kinetic energy of the fluid at the compressor outlet can still be used.
In order to define the efficiency, a look at the $h - s$ diagram as in Fig. 2.1(a) is useful. It shows an ideal (isentropic) and a real compression. Assuming adiabatic walls, the work input is equal to the total enthalpy increase to reach the desired outlet pressure, $\Delta h_{\mathrm{t,s}}$ in the ideal case and Δh_t in the real case. The isentropic efficiency is then defined as the ratio between the ideal work input and the real work input,

$$\eta_{\mathrm{is,tt}} = \frac{\Delta h_{\mathrm{t,s}}}{\Delta h_t} \ . \tag{2.4}$$

The subscript tt (total-to-total) is used here to clarify that stagnation states at the inlet and outlet are used. If the kinetic energy at the outlet cannot be used anymore, it is often replaced by the total-to-static efficiency. For calorically perfect gases with constant heat capacities c_{v} and c_{p}, Eq. (2.4) can be rewritten as

$$\eta_{\mathrm{is,tt}} = \frac{{\mathrm{PR}_{\mathrm{tt}}}^{(\kappa-1)/\kappa} - 1}{T_{t,\mathrm{out}}/T_{t,\mathrm{in}} - 1} \ . \tag{2.5}$$

where $\kappa = c_{\mathrm{p}}/c_{\mathrm{v}}$ is the ratio of specific heats. Using the relation

$$T = \left(\frac{\partial h}{\partial s}\right)_p \tag{2.6}$$

to determine the slope of the isobar in Fig. 2.1(a), the efficiency can also be estimated as a first order Taylor series approximation as

$$\eta_{\mathrm{is,tt}} \approx 1 - \frac{T_{t,\mathrm{out}} \Delta s}{\Delta h_t} \tag{2.7}$$

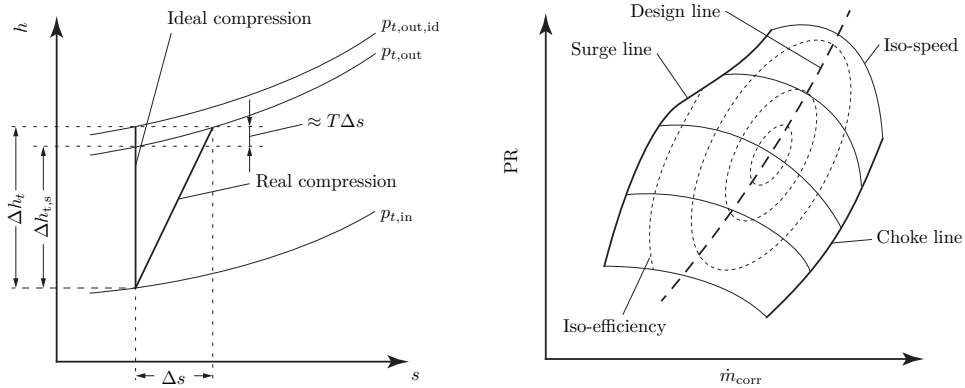

(a) $h - s$ diagram (b) Compressor map

Figure 2.1: Schematic depiction of a compressor operation through an $h - s$ diagram and a compressor map. The map is drawn to mimic typical radial compressor maps.

With the pressure ratio and efficiency defined, two additional similarity parameters will be introduced. They characterize the volume or mass flow through the compressor, as well as the blade speed. The volume and mass flow through a compressor are proportional to the inlet axial velocity $c_{x,1}$. There are two common ways to non-dimensionalize this velocity: with the ambient speed of sound or with the blade velocity. If the speed of sound is chosen, the inlet axial Mach number is conserved. This leads to reduced volume and mass flows

$$\dot{V}_{\text{red}} = \frac{\dot{V}}{\sqrt{T_1}} \tag{2.8}$$

$$\dot{m}_{\text{red}} = \dot{m} \cdot \frac{\sqrt{T_1}}{p_1} \tag{2.9}$$

where $\dot{V}$ is the physical volume flow and $\dot{m}$ is the physical mass flow. A drawback of this kind of reduction is that it leads to very uncommon units and numerical values. By correcting the inlet temperature and pressure with reference values, this drawback can be alleviated. The resulting volume and mass flows are denoted as corrected.

$$\dot{V}_{\text{corr}} = \frac{\dot{V}}{\sqrt{T_1/T_{\text{ref}}}} \tag{2.10}$$

$$\dot{m}_{\text{corr}} = \dot{m} \cdot \frac{\sqrt{T_1/T_{\text{ref}}}}{p_1/p_{\text{ref}}} \tag{2.11}$$

If the blade speed u is chosen to non-dimensionalize the inlet axial velocity, the mass flow parameter ϕ results:

$$\phi = \frac{\dot{V}}{\frac{\pi}{4} D_2^2 u_2} = \frac{\dot{m}}{\rho \frac{\pi}{4} D_2^2 u_2} \ , \tag{2.12}$$

where D_2 is the impeller exit diameter and u_2 is the blade speed at the exit. It can thus be seen as a measurement of the relative flow angle at the impeller inlet, provided there is no pre-swirl.
The blade velocity itself is commonly non-dimensionalized with the ambient speed of sound, so that the result is a blade Mach number

$$\mathrm{Ma_{u2}} = \frac{u_2}{\sqrt{\kappa R T_{t,1}}} \ , \tag{2.13}$$

with specific gas constant R. If the speed is instead given as revolutions per time, the result is the corrected speed n_{corr}

$$n_{\mathrm{corr}} = \frac{N}{\sqrt{T_1 / T_{\mathrm{ref}}}} \ , \tag{2.14}$$

where the reference temperature again helps in obtaining easily understandable units and numerical values.
Since the fluid in the compressor is in general a viscous fluid, a form of the Reynolds number can be defined in similitude investigations. The most common form for compressors is [Korpela, 2011]

$$\mathrm{Re_{D_2}} = \frac{D_2 u_2}{\nu} \tag{2.15}$$

with kinematic viscosity ν. Due to high tip speeds u_2, the Reynolds number is very high in compressors, and viscosity plays a role in the boundary layer only. Boundary layers are more important in small compressors than in large compressors, a phenomenon known as the scale effect. However, the adverse pressure gradients that must exist in compressors can lead to boundary layer separation. Thus, viscosity and boundary layer effects are also important. The boundary layer ability to withstand adverse pressure gradients is strongly dependent on the Reynolds number.

A compressor map is used to graphically show the possible operating points of a compressor in terms of corrected mass flow, pressure ratio, corrected speed, and isentropic efficiency. Figure 2.1(b) gives a schematic example of a compressor map. The corrected mass flow or volume flow is shown on the horizontal axis, the pressure ratio on the vertical axis. The compressor speed and efficiency are displayed via iso-lines. The limits of the compressor operating range are also displayed: At high mass flows, compressor operation is limited by choked flow in a throat. The choke line is often determined as an efficiency threshold at high mass flows. At low mass flows, compressor operation is limited by surge. Surge denotes an unstable operation of the compression system with severe pressure and mass flow oscillations. Much more detail on surge is given in subsection 2.3.2.

2.1.3 Work input

In the following, an Cartesian system with the three main directions axial (x), radial (r), and tangential (θ) will be used. The absolute flow velocity is therefore $\vec{c} = (c_x, c_r, c_\theta)$. A further important direction is the meridional direction (m), which describes the flow if projected into an axial-radial plane. The rotor rotates with angular velocity Ω. Its local velocity at location $\vec{r}$ can be written as

$$\vec{u} = \vec{\Omega} \times \vec{r} \; . \tag{2.16}$$

The velocity relative to the rotor, $\vec{w}$, is then

$$\vec{w} = \vec{c} - \vec{u} \; . \tag{2.17}$$

The absolute flow angle α,

$$\alpha = \angle(\vec{c}, \vec{u}) = \arctan \frac{c_m}{c_\theta} \; , \tag{2.18}$$

describes the angle between the absolute flow direction and the circumferential direction. The relation between the different velocity components in sketched in Fig. 2.2 for a rotating coordinate system as employed in the rotor. In the stator, $\vec{u} = 0$ and therefore $\vec{c} = \vec{w}$.

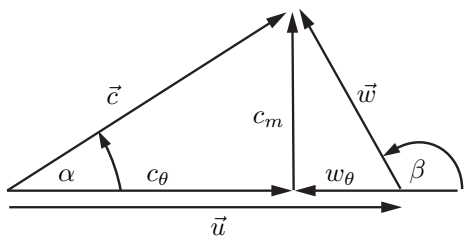

Figure 2.2: Velocities in a compressor rotor, taken from [Kerres, 2012].

Using the index 1 for the impeller inlet and the index 2 the impeller outlet, Euler's turbomachinery equation for adiabatic, steady-state flow can be written as

$$\Delta h_t = u_2 \, c_{\theta,2} - u_1 \, c_{\theta,1} \; . \tag{2.19}$$

With the help of the cosine rule, one gets

$$w^2 = c^2 + u^2 - 2\,u\,c\cos\alpha \quad \Leftrightarrow \quad u\,c_\theta = \frac{1}{2}(c^2 + u^2 - w^2) \; , \tag{2.20}$$

and with the help of (2.19):

$$h_{\mathrm{t},2} - h_{\mathrm{t},1} = \frac{1}{2}[\underbrace{(c_2^2 - c_1^2)}_{(I)} + \underbrace{(u_2^2 - u_1^2)}_{(II)} + \underbrace{(w_1^2 - w_2^2)}_{(III)}] \; . \tag{2.21}$$

The three terms in (2.21) are three ways in which the rotor increases the total enthalpy of the fluid: (I) is the increase in kinetic energy, (II) is the increase in static enthalpy due to centrifugal forces, and (III) is the increase in static enthalpy due to relative diffusion in the rotor.

In radial compressors, the fluid exits the rotor at a larger radius than its inlet radius, $r_2 > r_1$, and the term (II) is large. It is sketched in Fig. 2.3. The figure shows velocity triangles at the inlet and exit of an impeller projected onto the radial-circumferential plane. One can see that a large part of the stagnation enthalpy increase is caused by the higher exit radius. This is a main difference between the radial compressor and axial compressors. In axial compressors, streamlines exit the rotor at approximately the same radius they enter it, $r_2 \approx r_1$. Therefore, the term (II) is approximately zero. The additional enthalpy increase in radial compressors leads directly to two advantages over axial compressors:

- A higher pressure increase per stage is possible; radial compressors can reach pressure ratios $\mathrm{PR_{tt}} = 10$, while axial compressors are in the range of $\mathrm{PR_{tt}} = 1.5 - 1.7$ [Eckert and Schnell, 1961].
- Since the term (II) is independent of the flow itself, even stalled blades can increase pressure in radial compressors. Therefore, the operating range is wider.

The disadvantages of radial compressors, on the other hand, are a lower efficiency for large compressors and lower possible mass flow rates. The reasons for the lower efficiency are mainly a longer flow path and the difficulties in optimizing the blade profiles, since the flow is rotating. Additional problems arise from the need to diffuse the flow from a very high impeller exit velocity c_2 [Cumpsty, 2004]. The reason for the lower possible mass flow is a smaller throat cross-section in the inducer. A factor that reduces the work input for radial compressors is the slip factor. It relates the real outlet circumferential velocity $c_{\theta,2}$ to its ideal counterpart if the flow would follow the blade angles, $c_{\theta,2,id}$. The slip factor is defined as

$$\sigma = \frac{c_{\theta,2}}{c_{\theta,2,id}} \ , \tag{2.22}$$

and normally takes values in the range $\sigma = 0.8...0.95$ [Cumpsty, 2004]. A method to estimate the slip factor developed by Stodola, described e.g. in [Traupel, 2001], assumes irrotational inviscid inlet flow. The core flow through the impeller is not affected by viscosity. If the baroclinic term is also neglected since density gradients are small, the core is still irrotational at the impeller outlet. The rotation of the blade passage must then be counteracted by a passage vortex in the opposite direction so that vorticity is still zero at the impeller outflow. The resulting equation is

$$\sigma = 1 - \frac{\pi}{Z} \cdot \frac{\sin \beta_{2\mathrm{bl}}}{1 - \phi_2 \cot \beta_{2\mathrm{bl}}} \ , \tag{2.23}$$

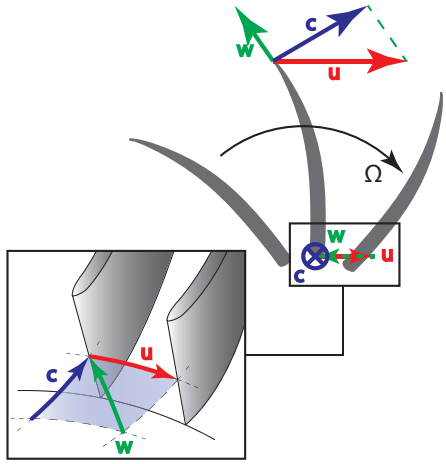

Figure 2.3: Velocity triangles in radial compressors. The increase in u from inlet to outlet of a centrifugal impeller is a major reason for the high increase in total enthalpy per stage.

where Z is the number of blades and ϕ_2 is the mass flow parameter from Eq. (2.12) using the impeller outlet conditions for normalization. Increasing the number of blades reduces the slip factor. Above a certain number of blades, however, the large blockage induced by the boundary layers can actually increase slip. The slip factor does not constitute a loss. The work transferred to the fluid is reduced, but so is the shaft work on the impeller shaft.

2.1.4 Loss mechanisms

As can be seen from Eq. (2.7) and Fig. 2.1(a), any losses in an adiabatic compressor are inherently connected to an increase in entropy. Important sources of irreversible entropy increase are viscous dissipation, e.g. in the boundary layer or other shear layers, heat transfer over a temperature difference, and discontinuities such as compression shocks. A useful summary of losses in turbomachines is given in [Denton, 1993].

Entropy generation in the boundary layer

For a two-dimensional boundary layer, the entropy production per unit length can be estimated as

$$\dot{S} = C_d \frac{\rho c_\infty^3}{T} \ , \tag{2.24}$$

where C_d is a dissipation coefficient and c_∞ is the free stream velocity. Common relations for the dissipation coefficient take into account whether the boundary

layer is laminar or turbulent, its shape factor, and the Reynolds number based on the momentum loss thickness δ_2. For laminar boundary layers, [Denton, 1993] gives the relation $C_d \approx 0.17\mathrm{Re}_{\delta_2}^{-1}$, with Re_{δ_2} as the Reynolds number based on the momentum loss thickness of the boundary layer. For turbulent boundary layers, [Schlichting and Gersten, 2017] proposes the estimate $C_d = 0.0056\mathrm{Re}_{\delta_2}^{-1/6}$ in the range of Reynolds numbers $10^3 < \mathrm{Re}_{\delta_2} < 10^5$ and no pressure gradient. Boundary layers in compressors are for the most part affected by an adverse pressure gradient, which increases the dissipation coefficient. In the passages of centrifugal compressor impellers, the rotation dampens turbulent fluctuations on the suction side (compared to a stationary passage) and amplifies them on the pressure side [Johnston, 1973]. This limits the possible flow adverse pressure gradient before separation occurs. The deceleration of the flow in the impeller is often quantified by a generalization of the diffusion factor by [Lieblein et al., 1953],

$$\mathrm{DF} = \frac{w_1 + w_2 + \Delta w}{2w_2} \tag{2.25}$$

which can also be used to estimate the momentum loss thickness, see also [Aungier, 2000]. In this equation, Δw is a theoretical estimate of the average blade velocity difference between the suction and the pressure side.

Entropy generation through mixing

For the mixing of two streams, an equation can be derived using a control volume approach and the conservation of mass, momentum, and energy. In its simplest form with incompressible flow and equal total temperature in both streams, the result given by [Denton, 1993] is

$$\dot{S} = \frac{1}{T}\dot{m}_c \left(c_\infty^2 - c_\infty c_c \cos\alpha_0\right) \tag{2.26}$$

where the subscript c refers to the stream joining the main flow with an angle α_0, see also Fig. 2.4. For more complicated cases, the reader is referred to [Greitzer et al., 2004]. An important occurrence of a mixing process in radial compressors is the jet-wake mixing at the impeller outlet as described by [Johnston and Dean, 1966], that will be discussed in more detail later in this section.

Entropy generation in compression shocks

The entropy increase of a compression shock is a result of the combined effects of viscous dissipation and heat transfer in the shock [Greitzer et al., 2004]. Since the continuum assumption is no longer valid within the shock, however, they require separate treatment. [Denton, 1993] gives the approximation for the entropy increase of a normal shock as

$$\Delta s\big|_{\mathrm{shock}} \sim \left(\mathrm{Ma}^2 - 1\right)^3 \ , \tag{2.27}$$

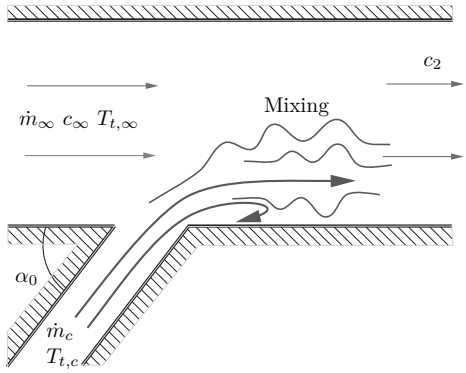

Figure 2.4: Entropy increase through the mixing of two streams (adapted from [Denton, 1993])

with Ma as the Mach number before the shock. At the same time, shocks increase the fluid pressure, which is after all the aim of a compressor. Therefore, compressors are often designed to have flow velocities in the transonic range, which can be a good compromise between the pressure and entropy increases. Another phenomenon that needs to be taken into account when dealing with shocks is their interaction with the boundary layer, which can lead to separation and thus additional losses. [Aungier, 2000] incorporates an empirical model for the losses due to shock – boundary layer interaction into his loss collection.

Entropy generation through heat transfer

The compressor is often assumed to be adiabatic when modeling compressor losses, since external heat addition is of minor importance for most machines [Denton, 1993]. This means that the only entropy increase from heat transfer can come from heat diffusion within the fluid (with heat transfer through advection being dealt with as mixing of streams, see above). Since the ratio of advection to diffusion, the Peclet number, is very large, entropy increase through heat diffusion is normally negligible.
Due to their proximity to the turbine driven by hot exhaust gases, turbocharger compressors are actually affected by heat addition. This effect was found to be most important at low speeds by several authors [Cormerais et al., 2009, Shaaban and Seume, 2012, Marelli et al., 2017]. At higher speeds, the compressor is much warmer than the surrounding air, and the heat loss to the environment approximately compensates for the heat addition from the turbine. The compressor can therefore even here be considered adiabatic [Shaaban and Seume, 2012]. If the ratio of heat transfer to work input is constant along a streamline, a polytropic process can be used to model the state changes within the compressor.

2.2 Description of the flow field

2.2.1 Impeller flow field

Coriolis force The Coriolis force appears due to the relative motion of fluid $\vec{w}$ to rotation of the coordinate system $\vec{\Omega}$. The Coriolis force per volume is

$$\frac{\vec{F}_\mathrm{C}}{V} = -2\,\rho\,(\vec{\Omega} \times \vec{w}) \quad . \tag{2.28}$$

The main effect of the Coriolis force in radial impeller flow is the contribution in circumferential direction,

$$\frac{F_{C,\theta}}{V} = -2\,\rho\,\Omega\,w_r \quad , \tag{2.29}$$

which becomes large in the radial part of the impeller. This force corrects for the apparent increase in angular momentum of fluid moving radially outwards. It will push the flow towards the pressure side of the blades and against the angular velocity, with a force proportional to the radial velocity.

Blade pressure force The blade pressure force mainly acts in the opposite direction to the Coriolis force, from the blade pressure side to the suction side. As a first approximation, the pressure is constant over the blade height, so that the pressure force is also independent of blade height. The blade pressure force points therefore mainly in the circumferential direction. Blade lean can be used to redirect the pressure force.

Jet-wake model The combination of Coriolis force and blade pressure force leads to a jet-wake model at the impeller exit: As described above, these two forces mainly acts against each other. The Coriolis force, however, is proportional to the radial velocity w_r, while the blade pressure force does not depend on it. The core flow is therefore strongly affected by the Coriolis force, while the boundary layer flow at hub and shroud is driven by the blade pressure force. The boundary layer flow is directed towards the suction side, and the core flow towards the pressure side. This creates a strong jet-wake flow at the impeller outlet, as first described by [Dean and Senoo, 1960]. Figure 2.5 shows the Coriolis force, the pressure and suction side, and the resulting jet-wake flow at the impeller outlet schematically.

Impeller curvature Another influence on the impeller flow is the curvature, which bends the impeller flow from the axial into the radial direction. At the shroud, the curvature radius is smaller than at the hub. This mean that there has to be a pressure gradient from hub to shroud, and that the boundary layer at the shroud has a stronger adverse pressure gradient than the one at the hub. For a shrouded impeller, the boundary layer at the shroud is therefore thicker and more prone to separation.

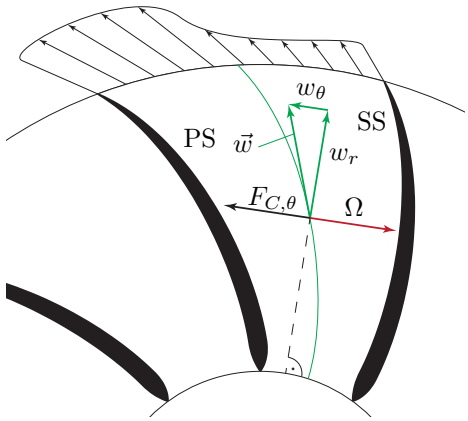

Figure 2.5: Coriolis force, blade pressure force, and jet-wake model shown in a blade passage.

Additional effects for unshrouded impellers In unshrouded impellers, there is a gap between the (rotating) blade top and the (non-rotating) shroud. A Couette-type flow enters the blade passage from the suction side at the shroud; its direction is therefore opposite to the shroud boundary layer flow in a shrouded impeller. This is schematically depicted in Fig. 2.6.

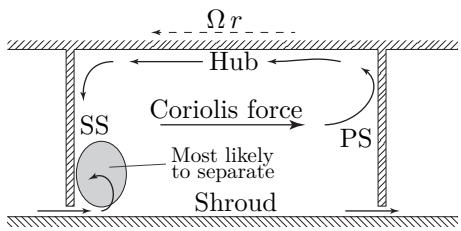

Figure 2.6: Schematic depition of the secondary flow in an impeller plane normal to the meanline (S3-plane).

The combined effect is that the low-momentum fluid is collected at the shroud and suction side. This is the area where boundary layer separation most likely occurs in radial impellers. This has been experimentally validated by [Moore, 1973] for a rotating passage, and by [Eckardt, 1975, Eckardt, 1976, Eckardt, 1979] for a real unshrouded impeller using Laser-Doppler velocimetry at the outlet. [Lennemann and Howard, 1970, Howard and Lennemann, 1971] used hydrogen bubble visualization and found the wake at the suction side for a shrouded impeller, but at the pressure side for an unshrouded one.

2.2.2 Vaneless diffuser flow field

Vaneless diffusers are commonly used in radial compressors that require a wide operating range, e.g. in automotive turbochargers. Due to the lack of vanes, there is no throat area that can choke, and no vane leading edge where the flow angle could be important for separation. Figure 2.7 shows a vaneless diffuser with constant width b, and the theoretical flowpath for incompressible and inviscid flow. The diffuser cross-section increases linearly with the radius r. From the conservation

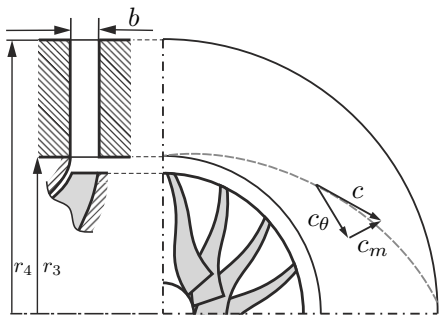

Figure 2.7: Incompressible and inviscid flow in a vaneless diffuser.

of mass, the radial velocity then decreases as well. The circumferential velocity also decreases linearly with increased radius due to the conservation of angular momentum. Thus, for zero axial velocity, the angle between the radial and the circumferential velocities is also constant,

$$\alpha = \arctan \frac{c_r}{c_\theta} = \text{const.} \quad . \tag{2.30}$$

The flow follows a logarithmic spiral through the vaneless diffuser, with an adverse pressure gradient. For high circumferential velocities c_θ (i.e. high impeller speed), and low radial velocities c_r (i.e. low mass flows), the angle α becomes very small, and the fluid travels along a long trajectory in the diffuser. In real viscid flow, this leads to high pressure losses and can lead to boundary layer separation at the hub or shroud side. An advantage of vaneless diffusers is that they facilitate a good mixing between the jet and wake flow coming from the impeller.

2.2.3 Volute flow field

In order to collect the radially outwards directed flow from the diffuser and guide it to the outlet pipe, a volute is often used. The volute is part of the stator. It can be likened to a single vane around the whole circumference [van den Braembussche, 2013]. The flow enters the volute with both a meridional (often only radial) and a tangential velocity component. Differently from the vaneless diffuser, the tangential velocity is the one that is responsible for the mass flow in the volute. The meridional

velocity component at the diffuser exit $c_{m,4}$ is turned inwards by the outer wall and becomes a swirling component $c_{sw,5}$. This is schematically drawn in Fig. 2.8. The

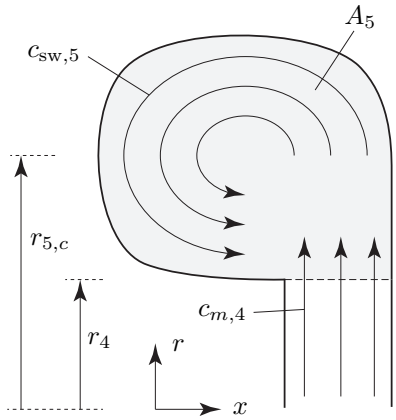

Figure 2.8: Transformation of the meridional velocity into swirl in the volute.

volute is continuously filled with fluid exiting the diffuser along its circumference. At its design mass flow, the cross-sectional area A_5 increases proportionally with the amount of fluid, so that the density and tangential velocity are approximately constant. A vortex forms in the outer part of the volute. Close to the vortex center, the shear forces become dominant and the vortex is of the forced vortex type [van den Braembussche, 2013]. The kinetic swirl energy is dissipated here.
At mass flows lower than the design mass flow, A_5 increases faster than the fluid mass along the circumference. Therefore, the tangential velocity decreases in tangential direction and the volute acts as an additional diffuser. The tangential velocity $c_{\theta,5}$ is high under the tongue, with a small flow angle. The pressure increases in circumferential direction and imposes non-uniform outlet boundary conditions on the diffuser upstream. Extensive investigations into diffuser and volute flow near the surge line can be found in e.g. [Gancedo et al., 2012] experimentally and [Semlitsch and Mihaescu, 2016] numerically using Large Eddy Simulation.
At mass flows higher than design flow, the same reasoning holds and leads to the opposite results. The volute acts as a nozzle, with the highest pressure and lowest tangential velocity under the tongue. High meridional velocities from the diffuser create a large amount of swirl in the volute which is dissipated.
In all mass flow cases, the increase in centerline radius $R_{5,c}$ along the circumference reduces the tangential velocity compared to a vortex tube due to the conservation of angular momentum around the machine axis.

2.3 Operating range and instabilities

2.3.1 Stall and rotating stall

A blade or vane is said to be stalled when the flow is no longer fully attached to its surface. Stall occurs due to an adverse pressure gradient which cannot be overcome by the low momentum of the flow in the boundary layer. It is a local phenomenon [van den Braembussche, 2013] that is stationary in its location.
Rotating stall denotes a flow separation that is not spatially fixed in its position within the respective rotating (impeller) or stationary (stator) coordinate system. Instead, it rotates with the impeller direction, but at a fraction of the impeller speed. In this section, a systematic distinction between different stall types will be attempted, following the categorization given in [Frigne and van den Braembussche, 1984]. The main characteristics of the rotating stall types are also summarized in Table 2.2 at the end of this section.

Impeller stall

In radial compressors, the impeller suction side is stalled in many operating points due to the accumulation of low momentum flow here as described in Section 2.2.1. A radial compressor impeller can still increase the enthalpy of the separated flow through the centrifugal effect, term (II) in Eq. (2.21). Stall does therefore not necessarily prohibit a stable operation of the whole compressor.
A stationary type of stall that has been found to be linked with the stability of the compression system is inducer stall. [Senoo et al., 1979] tested an impeller without a diffuser in order to eliminate a possible destabilization of the flow through downstream effects. They found that inducer stall is a function of the incidence angle at the inlet, leading to flow separation and reversal. At low compressor speeds, the compression system can still operate stable with inducer stall present. At high compressor speeds, the system enters surge when the inducer stalls. [Kämmer and Rautenberg, 1986] investigated a full radial compressor with a vaneless diffuser. They also detected stationary inducer stall due to flow incidence at low impeller speeds, which generates a swirling backflow. This backflow could negatively affect the system stability through the pre-swirl added to the incoming flow. Pre-swirl in the direction of the impeller rotation reduces the work input from the impeller, cp. Eq. (2.19) with $c_{\theta,1} > 0$. A reduction in work input at lower mass flows destabilizes the compression system, as will be shown in Section 2.3.2.
Impeller rotating stall (IRS) can be further divided into abrupt IRS and progressive IRS according to [Frigne and van den Braembussche, 1984]. Abrupt IRS occurs suddenly (hence the name) both at impeller inlet and impeller outlet with relative amplitudes $\Delta c/(2c_{\mathrm{rms}}) \approx 0.3$ and a rotating speed of $\omega_{\mathrm{st}}/\Omega \approx 0.2...0.3$ relative to the impeller rotation. It has been demonstrated experimentally in [Frigne and van den Braembussche, 1984] and [Abdelhamid, 1981], and discussed theoretically in [Abdelhamid, 1980]. It is believed that abrupt IRS occurs due to an interaction

between the diffuser and impeller, and may be triggered by vaneless diffuser rotating stall. The occurrence of abrupt IRS is strongly affected by eventual backsweep of the impeller blades, which makes it less likely.
Progressive IRS has been characterized experimentally by [Mizuki et al., 1978], [Frigne and van den Braembussche, 1984], and [Kämmer and Rautenberg, 1982]. It is believed to originate from the inducer [van den Braembussche, 2013] due to a high incidence, similar to rotating stall in axial compressors. Typical for this type of rotating stall is an increase in the stall cell rotating speed when the mass flow is decreased; their relative values are in the range $\omega_{\mathrm{st}}/\Omega \approx 0.7...1$.

Diffuser stall

A theoretical derivation of Vaneless Diffuser Rotating Stall (VDRS) was done in [Jansen, 1964]. He assumed the flow in the diffuser to consist of a free vortex mean flow with a superimposed perturbation, modeled by a wave equation for inviscid incompressible flow. Neglecting the non-linear terms in the equation, he showed that the perturbations are amplified if a local return flow exists, which triggers rotating stall. The local return flow appears due to a separation of the boundary layer. The theory predicts a rotational speed of the stall cells of $\omega_{\mathrm{st}}/\Omega \approx 0.05...0.22$. [Frigne and van den Braembussche, 1985] also use an inviscid incompressible core flow, but also model the boundary layers via their momentum equation. Core flow and boundary layer equations are coupled via an entrainment approach with empirically determined coefficients. They found that the occurrence of rotating stall in the vaneless diffuser depends on the inflow angle and the number of assumed stall cells. The predictions about the number of stall cells and their rotating speed agree very well with experimental investigations in [Kämmer and Rautenberg, 1986] and [Frigne and van den Braembussche, 1984].
Given the importance of the inlet flow angle derived theoretically, [Senoo and Kinoshita, 1977] investigate the influence of other geometric and flow parameters on the critical flow angle. Parameters that negatively affect the critical flow angle are inlet velocity distortions, high inlet Mach numbers, a long diffuser (r_4/r_4 large), and a wide diffuser (b/r_3 large), see also Fig. 2.7. [Senoo and Kinoshita, 1978] estimate a relation between the flow angle where local return flow starts to appear, α_{rt}, and the critical flow angle for the onset of rotating stall α_{cr} as

$$90^\circ - \alpha_{\mathrm{cr}} = 0.88(90^\circ - \alpha_{\mathrm{rt}}) \ . \tag{2.31}$$

This equation is shown to give good predictions about the onset of rotating stall for three vaneless diffusers in [Kinoshita and Senoo, 1985], where a very slowly rotating impeller is used to prevent impeller stall from occurring. A much more comprehensive study of available experimental data, presented e.g. in [van den Braembussche, 2013], shows a less positive figure.

An observation that several authors have made, e.g. [Senoo and Kinoshita, 1977], [Frigne and van den Braembussche, 1984], [Kämmer and Rautenberg, 1982], and

Type of stall	Progressive IRS	Abrupt IRS	VDRS
No. of stall cells	1...3	1...3	2...3
Rot. speed $\omega_{\mathrm{st}}/\Omega$	0.7...1	0.2...0.3	0.13...0.21 (exp.) 0.05...0.22 (theory)
Max ampl. $\Delta c/(2c_{\mathrm{rms}})$	0.1	0.3	0.1

Table 2.2: Types of rotating stall in radial compressors, summarized from literature. In this table, ω_{st} is the angular rotating stall propagation speed, Ω is the angular impeller speed, Δc is the maximum amplitude of the velocity fluctuations, and c_{rms} is the RMS of the absolute velocity.

[Kämmer and Rautenberg, 1986], is that impeller stall appears before diffuser stall at low compressor speeds. At high compressor speeds, DRS appears first, and the compressor enters surge when the impeller also becomes stalled. This is the basis for a surge prediction model by [Yoshinaka, 1977], also described in the next section.

2.3.2 Compressor surge

While rotating stall is a local phenomenon in the compressor, surge is an instability that affects the whole compression system. This system includes not only the compressor itself, but also ducts, volumes, and flow resistances such as orifices or throttle valves up- and downstream of the compressor. The system is said to be unstable if it does not return to its former steady operating point after a small perturbation. Instead, the perturbation is amplified into large pressure and mass flow oscillations, called compressor surge.
Surge is often divided into two different types: mild surge and deep surge. Mild surge denotes pressure and mass flow oscillations with a system natural frequency where the global mass flow is positive throughout the surge cycle. In deep surge, the global mass flow becomes negative for parts of the surge cycle. Different kinds of deep surge cycles have been observed in literature. A very common observation is that it can be divided into phases of quiescence, instability growth (as mild surge with increasing amplitude), a blow-down, and recovery, see [Fink et al., 1992] for a detailed description, but also [Dean and Young, 1977, Toyama et al., 1977] for earlier results. Other authors, e.g. [Hansen et al., 1981, Galindo et al., 2008, Dehner et al., 2013, Guillou, 2011] and also [Kerres et al., 2016b, Kerres et al., 2016a] report deep surge oscillations that do not consist of different phases, but are more similar to those of an harmonic oscillator. Their deep surge frequency is slightly below their mild surge frequency. It should be noted here that the authors reporting different surge behavior also report different B values. B is a non-dimensional parameter that characterizes a systems surge behavior. It will be defined in the next section. The given B values are in the range $B = 0.45...0.95$ for the systems that show harmonic oscillations in deep surge. It is $B = 2.7$ for the large B system in [Fink et al., 1992], which exhibits the different phases of deep surge. No B value is given for [Toyama

et al., 1977].
Besides the very common types of mild and deep surge, some authors further use the term classic surge [De Jager, 1995]. Its oscillations are harmonic with larger amplitude and slightly lower frequency than the mild surge frequency. Different from the deep surge oscillations described above, however, global backflow does not occur. In the following, it will only be distinguished between mild and deep surge.

Surge modeling

A common way to model compressor surge is by using a lumped parameter approach [Emmons et al., 1955], which is described in detail in [Greitzer, 1976a, Greitzer, 1976b] for axial compressors. It was later applied to radial compressors in [Hansen et al., 1981] and [Fink et al., 1992]. The compression system is modeled as a Helmholtz resonator with an actuator disk in the pipe symbolizing the compressor, and a second outlet to the compressible plenum that releases the fluid through a throttle. Figure 2.9 shows such a system schematically together with an analogous harmonic damped mechanical oscillator. The air mass in the pipe is the equivalent of the oscillating mass in the mechanical system, the compressible plenum acts as a spring (i.e. an energy storage), and the compressor and throttle are modeled as dampers. The damping coefficient of the "compressor damper" is positive at most operating points, since it feeds energy into the system. The system can be described

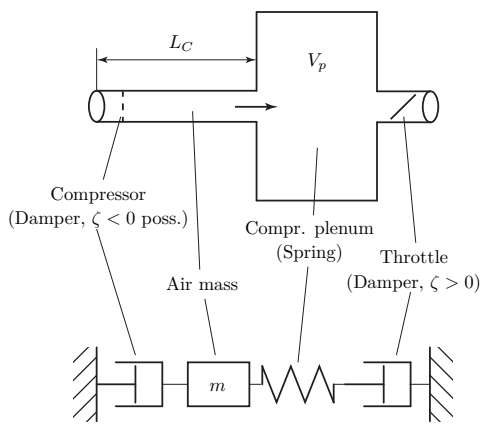

Figure 2.9: Idealized compression system as a Helmholtz resonator, and an analogous mechanical oscillator (adapted from [Greitzer, 1981])

by conserving momentum and mass throughout the system, i.e. the vector

$$\begin{bmatrix} p' \\ \rho a c' \end{bmatrix} , \tag{2.32}$$

where the velocity fluctuations c' are multiplied with the speed of sound a and the density ρ in order to have the same dimension as the pressure fluctuations p' [Greitzer et al., 2004]. a and ρ are assumed to be constant throughout the system. The perturbations are assumed to be of the form $e^{i\omega t}$, i.e. periodic disturbances. The transfer of pressure and velocity by means of incompressible flow through the duct is then

$$\begin{bmatrix} p' \\ \rho a c' \end{bmatrix}_{\text{in}} = \underbrace{\begin{bmatrix} 1 & (iL\omega/a) \\ 0 & 1 \end{bmatrix}}_{\mathbf{D}} \begin{bmatrix} p' \\ \rho a c' \end{bmatrix}_{\text{out}} . \tag{2.33}$$

Note that the inlet conditions on the left hand side are calculated from the outlet conditions on the right hand side. Since the flow is assumed to be incompressible, the pipe cannot store any mass and thus the second row of the transfer matrix just conserves the inlet velocity. The duct can be considered an inductance using the impedance analogy with electrical systems. For this simple system, the component is symmetric since $\det \mathbf{D} = 1$ and $D_{11} = D_{22}$ [Brennen, 1994]; switching inlet and outlet would result in the same transfer matrix. For the compression system described later as a series connection of matrices, this is not necessarily true. One has to pay attention to the direction.
The plenum is considered to be the counterpart to the pipe: it conserves the static pressure, but can store mass. It can be considered a capacitance using the impedance analogy. Its transfer matrix is then

$$\mathbf{P} = \begin{bmatrix} 1 & 0 \\ (i\omega V_{\text{p}}/(aA_{\text{C}})) & 1 \end{bmatrix} , \tag{2.34}$$

where V_{p} is the plenum volume (a constant) and A_{C} is the cross-sectional area of the inlet and exit ducts. For the throttle, the transfer matrix of small perturbations is given by

$$\mathbf{T} = \begin{bmatrix} 1 & k\,\text{Ma} \\ 0 & 1 \end{bmatrix} , \tag{2.35}$$

with k as the local throttle slope,

$$k = \frac{\Delta p}{0.5\rho c^2} , \tag{2.36}$$

which relates the pressure drop over the throttle to the velocity of the flow. The product $k \cdot \text{Ma}$ was derived as "acoustic throttle slope" in [Gysling, 1993]. As can be seen from Eq. (2.35) it is assumed that as for ducts, the density and hence the velocity at inlet and outlet of the throttle are the same, and the throttle has no capability to store mass. Equation (2.35) can be rewritten using the pressure parameter from Eq. (2.1) and the mass flow parameter from Eq. (2.12). The pressure parameter is here defined positive for the pressure drop and the reference area of the mass flow parameter is equal the duct cross-sectional area A_{C} instead of $\frac{\pi}{4}D_2^2$

in Eq. (2.12). The throttle transfer matrix is then

$$\mathbf{T} = \begin{bmatrix} 1 & u/(2a) \cdot \partial\psi_\mathrm{T}/\partial\phi_\mathrm{T} \\ 0 & 1 \end{bmatrix} , \tag{2.37}$$

with u as impeller blade speed and $\partial\psi_\mathrm{T}/\partial\phi_\mathrm{T}$ as non-dimensional local throttle slope. A similar approach is taken for the compressor. Its transfer matrix is given by

$$\mathbf{C} = \begin{bmatrix} 1 & -u/(2a) \cdot \partial\psi_\mathrm{C}/\partial\phi_\mathrm{C} \\ 0 & 1 \end{bmatrix} , \tag{2.38}$$

where $\partial\psi_\mathrm{C}/\partial\phi_\mathrm{C}$ is the local slope of the compressor characteristic.
Using these transfer matrices, the response of the compression system in Fig. 2.9 can be modeled by a serial connection of its components, namely the pipe, the compressor, the plenum, and the throttle. The resulting equation is

$$\begin{bmatrix} p' \\ \rho a c' \end{bmatrix}_\mathrm{in} = \mathbf{D} \cdot \mathbf{C} \cdot \mathbf{P} \cdot \mathbf{T} \cdot \begin{bmatrix} p' \\ \rho a c' \end{bmatrix}_\mathrm{out} . \tag{2.39}$$

The system natural frequencies can be calculated from the characteristic polynomial of the matrix product,

$$\det\left(\mathbf{D} \cdot \mathbf{C} \cdot \mathbf{P} \cdot \mathbf{T} - \omega\mathbf{E}\right) = 0 , \tag{2.40}$$

where $\mathbf{E}$ is the identity matrix. As boundary conditions, zero pressure oscillations at the inlet and outlet of the system are assumed. Since all matrices are of size 2x2, the characteristic polynomial has two solutions, cp. [Greitzer et al., 2004]:

$$\omega_{1,2} = -i\frac{a}{2}K_1 \pm i\frac{a}{2}\sqrt{K_1^2 + \frac{4A_\mathrm{C}}{V_\mathrm{p}L_\mathrm{C}}\left(\frac{\partial\psi_\mathrm{T}}{\partial\phi_\mathrm{T}}\right)^{-1}\left[\frac{\partial\psi_\mathrm{C}}{\partial\phi_\mathrm{C}} - \frac{\partial\psi_\mathrm{T}}{\partial\phi_\mathrm{T}}\right]} , \tag{2.41}$$

where

$$K_1 = \frac{u}{2aL_\mathrm{C}}\left[\frac{\partial\psi_\mathrm{C}}{\partial\phi_\mathrm{C}} - \frac{L_\mathrm{C}A_\mathrm{C}}{V_\mathrm{p}}\left(\frac{2a}{u}\right)^2\left(\frac{\partial\psi_\mathrm{T}}{\partial\phi_\mathrm{T}}\right)^{-1}\right] . \tag{2.42}$$

Since the disturbances are of form $e^{i\omega t}$ as stated above, they will grow if the imaginary part of the eigenvalues $\omega_{1,2}$ is negative. In this case, the system is unstable. In Eq. (2.41), all terms except the compressor characteristic slope are always positive. Therefore, one possibility for instability of the compression system is either that $K_1 > 0$, i.e. that the term in the bracket in Eq. (2.42) is positive. The terms that are not characteristic slopes are commonly summarized in the non-dimensional B parameter from [Greitzer, 1976a, Greitzer, 1976b],

$$B = \frac{u_2}{2a}\sqrt{\frac{V_\mathrm{p}}{A_\mathrm{C}L_\mathrm{C}}} = \frac{u_2}{2L_\mathrm{C}\omega_H} . \tag{2.43}$$

In this equation, ω_H is the eigenfrequency of a Helmholtz resonator with equivalent dimensions to the compression system. The first stability criterion becomes then

$$\frac{\partial \psi_C}{\partial \phi_C} \leq \frac{1}{B^2} \left(\frac{\partial \psi_T}{\partial \phi_T} \right)^{-1} . \tag{2.44}$$

This is called the dynamic stability criterion, since a violation consists of oscillations with an exponentially growing amplitude. Another instability is possible if the term in the square brackets in Eq. (2.41) is positive, so that the square root becomes larger than K_1. In this case, the exponent $i\omega t$ is real and positive for either ω_1 or ω_2, and the disturbance grows exponentially without oscillating. Due to this lack of oscillation, this instability is called static instability. Its stability criterion is

$$\frac{\partial \psi_C}{\partial \phi_C} \leq \frac{\partial \psi_T}{\partial \phi_T} , \tag{2.45}$$

i.e. a compressor slope less than the throttle slope. Comparing Eqs. 2.44 and 2.45, and taking into account that the throttle slope is relatively steep since the pressure drop increases with the square of the mass flow, we can see that the dynamic stability criterion is normally the stricter one. Figure 2.10 schematically shows the static (2.10(a)) and dynamic (2.10(b)) stability criteria in a non-dimensionalized compressor map. One can also see that a small B value increases the system stability.

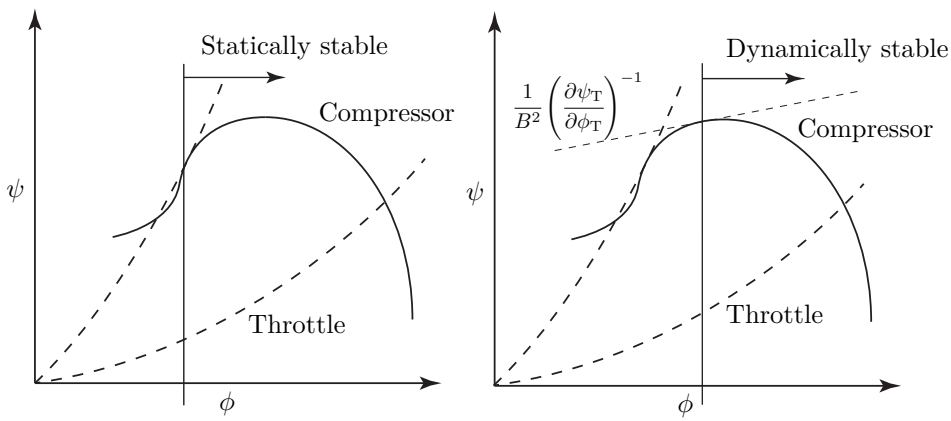

(a) Static stability (b) Dynamic stability

Figure 2.10: Schematic representation of the stability criteria in a compressor map

B can be thought of as a measurement that describes the ratio of pressure forces duct to inertia forces [Greitzer, 1981]. In a large B system, the compressor is able to strongly accelerate or decelerate the fluid in the duct, and the system is more easily provoked into surge. From Eq. (2.43), it can be seen that a small compressible

plenum after the compressor, a relatively large equivalent compressor length and cross-section, and a low tip speed Mach number all contribute to system stability. If the plenum volume is very small, e.g. due to a close-coupled valve, or its capacitance is very small (e.g. due to incompressible fluid in pumps), surge can theoretically be avoided.
Independent of the value of B, a negative slope on the compressor characteristic,

$$\frac{\partial \psi_C}{\partial \phi_C} < 0 \ , \tag{2.46}$$

results in linear stability of the system. In this case, a small perturbation in the mass flow $\mathrm{d}\phi_C$ in either direction leads to a reduced energy input $\mathrm{d}\phi_C \cdot \mathrm{d}\psi_C$ (keeping all other variables constant), since the change in pressure increase has the opposite sign. The oscillation energy can be dissipated by e.g. the throttle. It is only if the compressor slope is positive that the energy input increases compared to the steady-state operation after a mass flow perturbation.

The equation system as presented above uses linearized equations and is therefore only valid for small oscillations. For larger oscillations, non-linear effects can no longer be ignored. A delay time for the time it takes for the compressor speedline to adjust to the new operating conditions is needed to close the system. [Greitzer, 1976a, Greitzer, 1976b] numerically integrated the system of equations and showed that it can be used in its non-linear form to successfully predict surge amplitudes. For radial compressors, a similar investigation undertaken by [Fink et al., 1992] showed the necessity to include rotor wheel inertia effects due to the capability of the wheel to store additional energy, fulfilling a similar function to the plenum. More recently other authors [Theotokatos and Kyrtatos, 2001, Galindo et al., 2008, Bozza and De Bellis, 2010, Dehner et al., 2016] implemented this model for turbochargers in automotive internal combustion engines, establishing it as the standard surge model for these compression systems.

2.3.3 Modeling of compressor destabilization at off-design

Modeling approaches

Given the importance of the speedline slope for the stability of the compression system, a stability parameter SP was developed by Dean, see e.g. [Cumpsty, 2004]. The compressor stage is divided into its components i like impeller and diffuser. The overall pressure ratio is then

$$\mathrm{PR}_{\mathrm{stage}} = \prod \mathrm{PR}_{\mathrm{i}} \ . \tag{2.47}$$

Differentiating with respect to the mass flow leads to each components stability parameter SP_{i}

$$\mathrm{SP}_{\mathrm{i}} = \frac{1}{\mathrm{PR}_{\mathrm{i}}} \frac{\partial \mathrm{PR}_{\mathrm{i}}}{\partial \dot{m}} \tag{2.48}$$

and the condition for stability

$$\sum \mathrm{SP_i} \leq 0 \ . \tag{2.49}$$

where individual components can be divided into those that contribute to stability ($\mathrm{SP_i} < 0$) and those that destabilize the system ($\mathrm{SP_i} > 0$). A vaned diffuser or a passage diffuser is inherently unstable, since its pressure recovery increases with the inlet meridional velocity, i.e. the flow rate [Cumpsty, 2004]. This is one reason why compressor stages that need a wide operating range, like turbocharger in an automotive context, often use vaneless diffusers despite their lower efficiency.
In the following, different factors that influence component stability will be discussed, starting with the impeller. Not all of these factors are losses. If the impeller blades are forward swept, i.e. in rotational direction, work input will increase with increasing mass flow due to the higher outlet tangential velocity $c_{\theta,2}$. Forward swept blade tips are very rare. Backward swept blades, on the other hand, increase operating range. A similar effect is achieved by adding pre-swirl in the impeller rotation direction at the compressor inlet. For guide vanes in a fixed position, the pre-swirl $c_{\theta,1}$ will increase with the inlet axial velocity $c_{x,1}$, which is proportional to the mass flow. At low mass flows, the work input is thus increased (cp. Eq. (2.19)) and the system stability is increased. The choke line was found to be unaffected, leading to a wider compressor map [Figurella et al., 2015].
Losses in the compressor stage are destabilizing if they increase with lower mass flows. Several authors [Galvas, 1974, Aungier, 1995, Oh et al., 1997, Gravdahl et al., 2004] have developed sets of different loss terms for the impeller, where each loss term is connected to a flow property. Traditionally, these loss terms are expressed as an adiabatic enthalpy head loss coefficient

$$\lambda = \frac{\Delta h_{\mathrm{t,loss}}}{u^2} \ , \tag{2.50}$$

where $\Delta h_{\mathrm{t,loss}}$ is the adiabatic enthalpy head loss, imposed at constant entropy to calculate the total pressure losses. While the exact loss terms vary, the following effects are generally included:

Incidence Incidence describes the difference between the flow angle and the leading edge angle. If the flow at the leading edge is not aligned with the blade surface, it will experience strong pressure gradients which turn the flow. This adverse pressure gradient increases the likelihood of boundary layer separation, i.e. inducer stall. Incidence losses are usually modeled as a loss of the kinetic energy associated with the excess relative circumferential velocity at the inducer inlet

$$\lambda_{\mathrm{inc}} \sim \left(\frac{w_{x,1} \sin(\beta_1 - \beta_{1\mathrm{bl}})}{u} \right)^2 \ . \tag{2.51}$$

The relative flow angle $\beta_1 = \arctan(w_{x,1}/w_{\theta,1})$ becomes very small at low mass flows, since $w_{x,1}$ is proportional to the mass flow. The blade angle $\beta_{1\mathrm{bl}}$ is constant, and the losses therefore increase strongly at low mass flows.

Throat losses Throat losses are caused by compression shocks, either directly or through their impact on the boundary layer. A requirement for shocks to occur is a local Mach number $\mathrm{Ma}_{\mathrm{th}} > 1$. Of the loss collection sets mentioned above, only [Aungier, 1995] provides a correlation, based on a polynomial where the highest term increases with order 7. Since high Mach number occur only at high mass flows and high speeds, throat losses are mainly important near the choke line.

Blade loading Blade loading losses stem from two pressure gradients: The pressure gradient from suction to pressure side, as well as the adverse pressure gradient on the suction side boundary layer where the flow is decelerated. The loss collection sets mentioned above use an estimate of the velocity difference between suction and pressure side, either directly or through the diffusion factor Eq. (2.25). Blade loading is also responsible for the creation of the wake zone [Dean and Senoo, 1960].

Jet-wake mixing The jet and the wake zones in the impeller exit mix, creating additional losses. Since jet and wake are assumed to have the same total temperature and flow incompressibility is assumed, see e.g. [Dean and Senoo, 1960], the losses grow quadratically with the velocity difference between jet and mixed state (cp. also Eq. (2.26))

$$\lambda_{\mathrm{jw-mix}} \sim \left(\frac{c_{\mathrm{jet}} - c_{\mathrm{mixed}}}{u} \right)^2 . \tag{2.52}$$

This difference grows as the other losses through incidence and blade loading increase, since the losses accumulate in the wake, while the jet is isentropic. Jet-wake mixing losses therefore increase as compressor operation approaches the surge line.

Skin friction Skin friction is estimated via a skin friction factor from an analogy to turbulent pipe flow. The skin friction factor itself is Reynolds-number dependent, and scales approximately with $k_{\mathrm{sf}} \sim \mathrm{Re}^{-0.3}$ in the range of interest [Schröder, 2004]. The friction head increases with the square of the relative meridional velocity in the blade passages, so that the loss coefficient scales at

$$\lambda_{\mathrm{sf}} \sim \left(\frac{w_{m,1} + w_{m,2}}{2} \right)^{1.7} \sim \dot{m}^{1.7} . \tag{2.53}$$

Of the losses described above, incidence, blade loading, and jet-wake mixing losses increase as compressor operation moves towards lower mass flows. Looking only at the losses itself and keeping the work input constant, they therefore contribute to the destabilization of the compression system on the left side of the compressor map by bending the characteristic slope downwards. Incidence and blade loading, however, are also associated with a pressure increase due to a high redirection and deceleration of the flow. The pressure increase stabilizes the system. Only when the

pressure losses grow faster than the pressure rise are these phenomena destabilizing.

Another way of looking at the impeller is the Two Elements In Series (TEIS) model by Japikse, see e.g. [Japikse et al., 2006]. The two elements model the flow in the inducer and the exducer. They are two diffusers for most operating points, but can also be nozzles at high mass flows. This model allows to use the large set of available experimental data [Japikse and Baines, 1998] for impeller design, and to estimate the stall points for the inducer and exducer.

Rotating stall in the impeller as described in Section 2.3.1 is another phenomenon that contributes to large losses at low mass flows, since it only appears in these operating points. While the connection between rotating stall and surge in radial compressors is a subject of debate, see e.g. [Greitzer, 1981, Cumpsty, 2004, van den Braembussche, 2013] for summaries, there is mostly agreement in literature that rotating stall contributes through the increased losses and as a source of flow perturbation which can be amplified into surge by the compression system. The exact relationship between rotating stall and surge is however much less clear for radial compressors than for axial compressors.

Vaneless diffuser Since the flow in a vaneless diffuser is much simpler than the one in the impeller, it is possible to use well-calibrated 1D flow descriptions [Aungier, 2000]. The differential equations for the conservation of mass, radial momentum, angular momentum, and energy are discretized and numerically integrated by marching radially outwards. Losses are collected in the boundary layer using empirical relations for channel flows with an adverse pressure gradient. At low mass flows, the diffuser inlet flow angle α_3 becomes very small, cp. Fig. 2.7. The flow path through the diffuser increases, which leads to higher losses. The vaneless diffuser is therefore, like vaned and passage diffusers, inherently destabilizing. Rotating stall is another phenomenon that destabilizes the system due to its occurrence at low mass flows.
If the diffuser is followed by a volute, the volute will also impose a circumferentially changing pressure at the diffuser outlet during off-design operation. This pressure increases along the volute at low mass flows, essentially acting as another diffuser. The flow in the vaneless diffuser has to overcome the circumferential adverse pressure gradient in addition to the radial one.

A surge model based on stall correlations Based on the observation that impeller stall occurs before diffuser stall at low impeller speeds, while the order is the other way round at high impeller speeds, [Yoshinaka, 1977] developed a different surge model from the one described above. The assumption is that the compression system enters surge when both the impeller and the diffuser are stalled. The model is described in [Yoshinaka, 1977] for a combined vaneless and vaned diffuser, but can in principle be applied to vaneless diffusers only as well. Using a correlation

between the inlet flow angle and stall for both components, a stability diagram as can be seen in Fig. 2.11 can be drawn. As has been found by many investigations, the diagram shows that at low impeller speeds (the $n_{\mathrm{corr}} = \text{const.}$ lines more to the left), inducer stall occurs before diffuser stall. With a stalled inducer, but a diffuser that is not stalled, the stage can still operate in a stable way. Surge at low speeds occurs when the diffuser also enters stall. At high impeller speeds, the relation is reversed. The stage can still operate in a stable way with only diffuser stall present. Once the inducer also stalls, the stage enters surge.

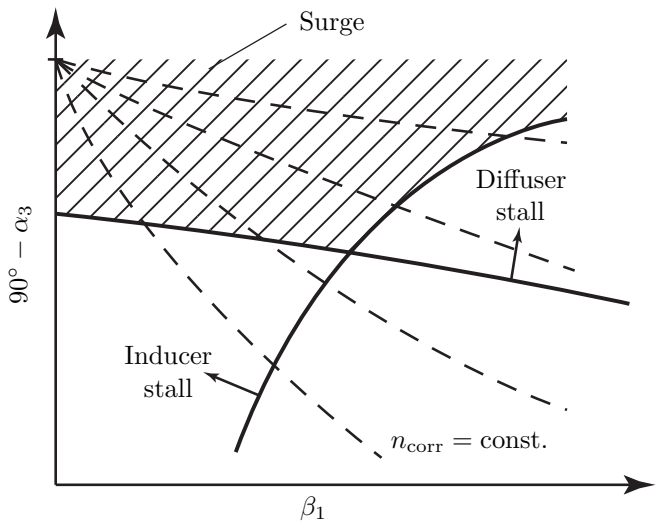

Figure 2.11: Surge model using impeller and diffuser stall correlations adapted from [Yoshinaka, 1977]

Accuracy of these modeling approaches

These models were mainly validated against experimental data for larger compressors. Impeller sizes used range from $D_2 = 144.8\,\mathrm{mm}$ for the [Galvas, 1974] model, and three impellers with sizes between $D_2 = 207.4\,\mathrm{mm}$ to the [Eckardt, 1975, Eckardt, 1976] impeller with $D_2 = 400\,\mathrm{mm}$ for the [Oh et al., 1997] model. The model of [Aungier, 1995] was validated against "a hundred" impeller designs as reported by the author without giving much more details.

Attempts to evaluate the accuracy for smaller compressors were mainly done using Computational Fluid Dynamics (CFD), e.g. by [Harley et al., 2013], [Schneider et al., 2015], as well as [Sundström et al., 2016, Kerres et al., 2017c, Sundström et al., 2017] which are also appended to this thesis as papers VI to VIII. [Harley et al., 2013] compare the model losses to RANS computations for the impeller and vaneless diffuser. Their results show that the sum of impeller loss coefficients does

not vary strongly with mass flow or impeller speed. There are significant differences between CFD and 1D model in the vaneless diffuser, mainly at low mass flows where the model loss coefficients are up to twice as high. [Schneider et al., 2015] compare the results of a two-zone impeller model and 1D diffuser model to RANS CFD and conclude that for the compressor and model investigated, the accuracy of 1D and RANS computations is comparable.
For two similar compressors in different sizes, the 1D model by [Aungier, 1995] and RANS computations are compared to the hot gas stand measurement provided by the supplier in [Kerres et al., 2017c] (paper VI) and [Sundström et al., 2017] (paper VIII). The relative accuracy of the total pressure ratio prediction is shown in Fig. 2.12, with the columns distinguishing between the large and small compressor, and the rows between the 1D model and RANS computations. All contour maps use the same coloring for the relative error, where blue colors indicate an underestimation of the pressure ratio, and the red colors an overestimation.
It can be seen that for both compressors, RANS simulations are much more accurate than the 1D models at low speeds and low mass flows. The 1D model predicts a relatively strong curvature of the speedline, which results in an underestimation of pressure ratios near surge, but reasonably accurate along the design line. If one would try to predict the surge line based on the 1D model results without knowing the results from the gas stand, the estimated surge line would be located to the right of the real surge line. At the choke line, the RANS overestimates the pressure ratio while the model underestimates it. High impeller speeds are difficult to estimate for both the 1D model and CFD.

A separation between impeller, diffuser, and volute losses for both compressors, and comparison to the RANS data is attempted in both papers. Since no measurements of the impeller and diffuser outlet conditions are available, these comparisons have to be done indirectly via the CFD results. It is assumed that the CFD predicts the flow field well if it predicts the total pressure ratio correctly; this is of course a very strong assumption, but was done nonetheless for lack of alternatives. The highest speedlines are exempted from this analysis, since the pressure ratio prediction is not good enough here.
The impeller loss coefficients are very similar between CFD and 1D model, with the best agreement at low mass flows and low speeds. Losses in the vaneless diffuser are much higher in the 1D model at low mass flows. This difference is especially large for the smaller compressor. This could be a result of the very long flow path through the diffuser near surge due to the small inlet flow angle. At high mass flows, the volute produces the largest losses in the 1D model due to the dissipation of the meridional velocity and the wrong sizing for this operation point. The combination of high volute losses near choke and high vaneless diffuser losses near surge leads to the strongly curved compressor characteristic in the 1D model.

Large Eddy Simulation (LES) is employed in [Sundström et al., 2016] as basis for an evaluation of the [Gravdahl and Egeland, 1999] model. The compressor in

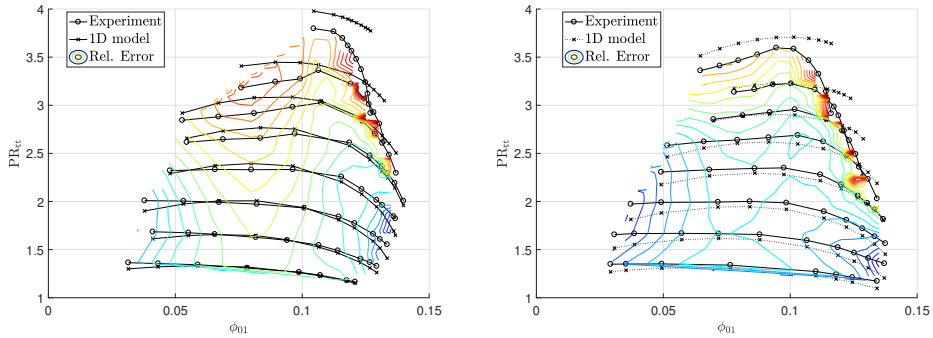

(a) 1D model, larger compressor

(b) 1D model, smaller compressor

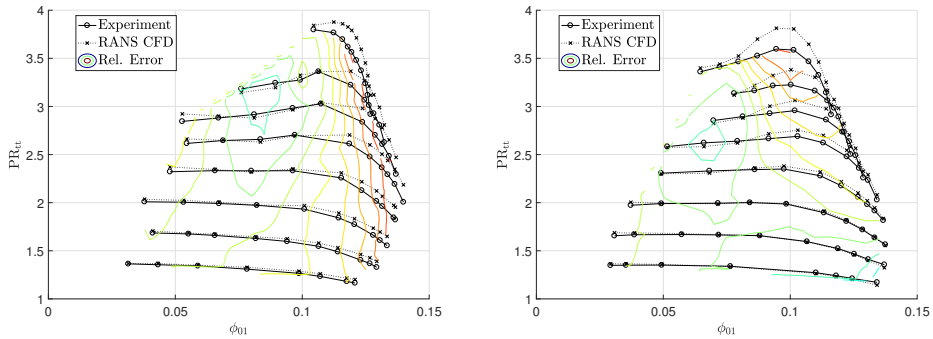

(c) RANS, larger compressor

(d) RANS, smaller compressor

Figure 2.12: Relative error of the 1D model and RANS predictions for two turbocharger similar compressors in different sizes

question is equipped with a ported shroud, which affects loss accounting in the impeller: in near surge operation, the backflow from the impeller through the ports mixes upstream the inducer with the inlet flow. Since large parts of the entropy increase through the impeller is contained in this backflow, the impeller itself appears approximately isentropic. Figure 2.13 schematically displays the averaged state changes the meridional coordinate.

2.3.4 Stability indicators

Considering the different types of surge (mild or deep) and their dependency on external devices such as throttles or plenums, the definition of a surge line is not straightforward. This is further complicated by the fact that much of the terminology has its origin in axial compressor theory, where rotating stall is the counterpart to surge for systems with small B values [Greitzer, 1976a, Greitzer, 1976b]. [Traupel,

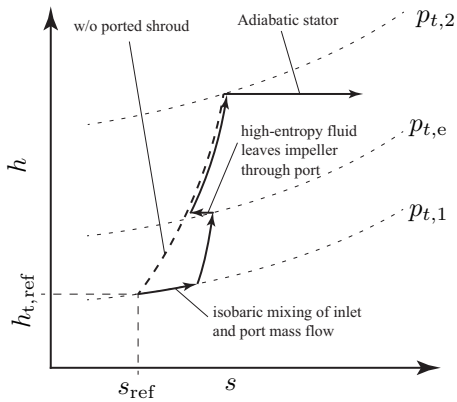

Figure 2.13: State changes of a compressor with a ported shroud in a $h-s$ diagram.

1982] calls the lower operational limit "stability limit", using a more general term that can also include rotating stall. He defines it as the mass flow at which a further reduction will lead to non-axissymmetric or pulsating throughflow. In [Cumpsty, 2004], the lower operational limit is called the surge line and is defined as "the point at which a further reduction in mass flow leads to an abrupt and definitive change in flow pattern in the compressor." This definition can also include rotating stall for axial compressors. The [SAE, 1995b] Turbocharger Nomenclature and Terminology, common for automotive turbochargers, defines surge as "severe flow reversal combined with audible coughing and banging."
Since the compressor mass flow often fluctuates slightly even at stable operation, it is important to keep a safety margin between the time-averaged mass flow and the surge line. [Dean and Young, 1977] compare the situation to a drunk person (the compressor) walking along a cliff (the surge line), careening to the left and right. Since it is not possible to recover once over the cliff, the margin must be larger than the maximum deviation from the mean path. The surge margin gives the distance of the compressor operation from the point of no return. A common definition, using the distance along the pressure ratio axis is

$$\mathrm{SM}_{\mathrm{PR}} = \frac{\mathrm{PR}_{\mathrm{SL}} - \mathrm{PR}_{\mathrm{OP}}}{\mathrm{PR}_{\mathrm{OP}}} \ , \tag{2.54}$$

where $\mathrm{PR}_{\mathrm{OP}}$ is the pressure ratio at current operation and $\mathrm{PR}_{\mathrm{SL}}$ is the pressure ratio at the surge point of the current speedline, cp. [Cumpsty, 2004]. This definition is common for axial compressors, where the speedlines have a strongly negative slope, and the surge line limits operation mainly towards higher pressure ratios. Radial compressors have almost flat or even positive speedline slopes, and thus the definition given in Eq. (2.54) is less useful along a speedline. Definitions based on

the mass flow,

$$\mathrm{SM}_{\mathrm{MF}} = \frac{\dot{m}_{\mathrm{OP}} - \dot{m}_{\mathrm{SL}}}{\dot{m}_{\mathrm{OP}}} \ , \tag{2.55}$$

or a combination of these two,

$$\mathrm{SM}_{\mathrm{MF,PR}} = 1 - \frac{\dot{m}_{\mathrm{OP}}}{\dot{m}_{\mathrm{SL}}} \cdot \frac{\mathrm{PR}_{\mathrm{SL}}}{\mathrm{PR}_{\mathrm{OP}}} \ , \tag{2.56}$$

are more common. The minimum surge margin is system specific, since the occurrence of surge also depends on system parameters other than the compressor. Furthermore, a short period of mild surge or even a few deep surge cycles might be considered non-catastrophic for systems like internal combustion engines, while it must absolutely be avoided if it leads to a catastrophic system failure as e.g. in jet engines. Quantitative values for the minimum surge margin are hard to come by, since they are normally considered an industrial secret. [Skoch, 2003] gives a value of $\mathrm{SM}_{\mathrm{MF,PR}} \approx 11.7\%$ for a baseline configuration of a centrifugal compressor.

A practical problem common to all surge line definitions given above is that they are defined based on mass flow oscillations. Measuring time resolved mass flows is no simple feat, especially if the measurement device should be able to distinguish between forward and reverse mass flows. Several authors have therefore used pressure, speed, and temperature measurements to determine system stability.A short review of these studies will be presented in the following.

Pressure oscillations Pressure oscillations are an inherent feature of compressor surge. Since time-resolved pressure measurements are comparably straightforward, using them as a surge indicator is popular in literature. A simple criterion, e.g. investigated in [Andersen et al., 2008, Galindo et al., 2005, Guillou, 2011, Gancedo, 2014], is the standard deviation of the pressure,

$$\sigma = \sqrt{\frac{1}{N} \sum_{i=1}^{N} \left(p - \langle p \rangle\right)^2} \ , \tag{2.57}$$

where $\langle \square \rangle$ is the mean value operator and N is the number of samples. The pressures are normally taken downstream of the compressor. A normalization of the pressure standard deviation by an impeller dynamic pressure, i.e. taking the standard deviation of the work coefficient as defined in Eq. (2.2), was undertaken by [Guillou, 2011, Gancedo, 2014, Karim et al., 2015] and found to lead to comparable values at the surge points of different impeller speeds. In order to isolate the fluctuations with the typical surge frequencies, i.e. the system natural frequency or very low frequency of blow-down cycles, the pressure signal can be filtered using a low-pass filter before calculating the standard deviation, see [Guillou, 2011, Gancedo, 2014]. A very similar approach is to estimate the power spectrum of the oscillations, see

Eq. (3.19), and integrate it in the frequency interval of interest. This approach was taken in [Dehner et al., 2011, Dehner et al., 2013] and in [Kerres et al., 2016a, Kerres et al., 2016b, Kerres et al., 2017a], where it is called signal power and calculated as

$$P = 10 \cdot \log_{10} \left(\frac{1}{p_{\text{ref}}^2} \int_{\omega_s - \Delta\omega}^{\omega_s + \Delta\omega} S_{xx} \mathrm{d}\omega \right) \text{[dB]} \ . \tag{2.58}$$

In Eq. (2.58), p_{ref} is a reference pressure, ω_s is the system surge frequency, $\Delta\omega$ is half the frequency interval size, and S_{xx} is the signal power spectral density. This approach is in principle the same as the standard deviation after applying a block bandpass filter, which can be shown using Parseval's theorem. It uses the quadratic spectrum. Other authors, e.g. [Galindo et al., 2005, Andersen et al., 2008] used the linear frequency spectrum obtained via Discrete Fourier Transform (DFT), and consequently use the height of the peak at surge frequency.
[Bright et al., 1995, Bright et al., 1997, Bright et al., 1999] use a method from chaotic time series analysis, the correlation integral, in order to detect the onset of system instabilities on an axial compressor. It can be thought of as a measurement of the complexity of the time series. At stable operation, the pressure signal is complex because many factors influence the instantaneous pressure value. At the onset of instabilities, the pressure signal is mainly governed by the instability, and the signal becomes less complex. The correlation integral can be used to estimate the correlation dimension, which is a measure of the fractal dimension and thus closely related to the Hurst exponent [Mandelbrot, 1985]. More details on fractal dimensions and the Hurst exponent are given in chapter 3.
The increase in noise generation when the compressor enters surge can also be used as a criterion. [Kabral et al., 2013] showed for a small turbocharger compressor that the acoustic dampening of low frequency sound waves decreases as compressor operation moves closer to the surge line. Beyond the surge line, the compressor was found to amplify these sound waves. As a more subjective criterion, [Skoch, 2005] defines the surge line as the points where "significant change in sound emanating from the compressor" is observed. For a turbocharger in on-engine operation in a passenger car, [Andersen et al., 2008] use subjective operator noise as logged during driving.

Temperature Temperature measurements with thermocouples have a low resolution in time due to the high thermal inertia of the thermocouple. Some authors, e.g. [Dehner et al., 2013], succeeded nonetheless in obtaining temperature with a sampling rate high enough to capture surge oscillations. Much more common, however, is the measurement of the temperature closely upstream the inducer. If the inducer is stalled, flow reversal occurs and the inducer ejects fluid with a higher temperature. The temperature increase at the inlet can then be used to estimate how close to surge the compressor is operating. This method was found to work well for low impeller speeds on an automotive turbocharger in [Andersen et al., 2008]. At high impeller speeds, surge occurred before a significant temperature increase could

be measured. This data point supports the hypothesis that the onset of inducer stall triggers surge at high impeller speeds, while it is compatible with system stability at low impeller speeds.

Impeller speed Mass flow and pressure oscillations lead to an oscillating torque τ from the pressure forces acting on the compressor wheel. If the shaft power coming from the turbine is constant, the difference in net torque will accelerate the wheel according to the conservation of angular momentum

$$J\frac{\mathrm{d}\Omega}{\mathrm{d}t} = \sum \tau \ , \tag{2.59}$$

where J is the moment of inertia. The moment of inertia includes also the shaft and the turbine wheel, which are typically made of metals with higher density than the compressor wheel. The value for the automotive turbochargers used in the experiments later is $J = 1.26{\cdot}10^{-}5\,\mathrm{kg\,m^2}$, see [Westin, 2005]. Estimating the time-averaged torque with the help of the equation in [Theotokatos and Kyrtatos, 2001] at the surge line results in values of $\bar{\tau} \approx 0.3\,\mathrm{Nm}$. The speed variation can therefore play a role in the dynamics of the system. Surge detection by speed variation is used to determine the onset of surge on gas stands, see e.g. [Bergmann and Parma, 2016]. On internal combustion engines, flow pulsation from the exhaust valves impose a fluctuating driving torque on the turbine side, making the application of this method more difficult.

As can be seen from the discussion above, many different surge indicators exist in literature today. The remainder of this thesis will mainly be concerned with introducing another one: The Hurst exponent, based on the integrated pressure time series. The Hurst exponent H is a non-dimensional number that contains information about long-term memory in the time series. If the time series is negatively autocorrelated, values are in the range $0 \leq H < 0.5$. For uncorrelated data, $H = 0.5$, and for positive autocorrelation, $H > 0.5$. One potential advantage is the well-defined limit of zero for the limit cycle oscillations. This could result in a system-independent $H = 0$ in surge, while values are $H = 0.5$ in uncorrelated noise during stable operation. Another potential advantage to be investigated are the surge precursor capabilities. A generalization of H allows distinguishing between large and small oscillations, which could be used to detect the onset of system instabilities. More explanations on the Hurst exponent and the methods used to estimate it are given in the next chapter.

3 Fractals and the Hurst exponent

3.1 Fractals and self-similarity

3.1.1 Fractal dimensions and scaling laws

The dimension of a space is a familiar concept. It is a positive integer number corresponding to the degrees of freedom for the position of a point in this space. Thus, the dimension of a curve is one, the dimension of a plane is two, and so on. One way to determine the length of a curve is then by using a ruler along the curve. If the curve is a straight line, its length can be determined directly from the ruler. If the curve is not a straight line, however, this method will not give the exact curve length, but only a lower estimate. The length estimate can be improved by using several rulers of shorter length. Figure 3.1(a) shows an example of such a curve length estimate. The endpoints of each ruler are points on the curve. Using five instead of one rulers greatly improves the accuracy of the curve length estimate. The limit sum of infinitely many rulers of infinitesimal length $\mathrm{d}l$ gives the length of the curve L,

$$L = \lim_{N\to\infty} \sum_{i=1}^{i=N} \mathrm{d}l \ . \tag{3.1}$$

Equation (3.1) converges for e.g. smooth (continously differentiable) curves to a limit length. Each point on the curve can then be described by one value: a distance from some origin. The curve is one-dimensional.
There exist curves, however, for which the sum does not converge; that is, the ruler cannot be made small enough to capture all the details of the curve. An example of such a curve is the Koch curve, which will be described in the following. The Koch curve, named after Swedish mathematician Helge von Koch, can be constructed the following way [Bunde and Havlin, 2009]: In the zeroth iteration, a straight line of length l_K is drawn. In the next iteration, this line is replaced by four lines of length $l_K/3$. Of these, the first and fourth line correspond to sections of the line from the previous iteration. The second and third line replace the middle section by forming the hat of an equilateral triangle. Figure 3.1(b) shows iterations $n = 0, 1, 2, 5$. For an infinite number of iterations to construct the curve, Eq. (3.1) does not converge. As opposed to finitely long curves, the position along the Koch curve can thus not

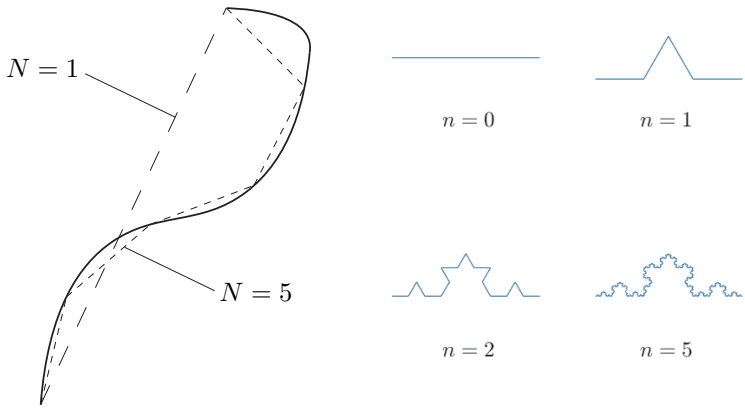

(a) Length of a curve as estimated by yardsticks of different length

(b) Different iterations of the Koch curve

Figure 3.1: Determining the lengths of different curves.

be determined by just one value. The section length between any two points on the curve is infinitely long. In order to characterize such curves, the box counting dimension d_{box} is introduced. The box counting dimension measures how the length of the curve changes with a reduction of the ruler length l:

$$d_{\text{box}} = \lim_{l \to 0} \frac{\log N}{\log 1/l} \ , \tag{3.2}$$

where N is the number of rulers needed, and thus a function of ruler length l. For the Koch curve, each iteration replaces a segment with 4 segments of $\frac{1}{3}$ length, and the box counting dimension is

$$d_{\text{box}} = \frac{\log 4}{\log 3} \approx 1.2619 \ . \tag{3.3}$$

Curves that have a non-integer ("fractional") dimension are called fractal curves. Fractal curves have a box counting dimension between 1 and 2. If the curve seems very smooth, the dimension will be close to 1, while rough looking curves have fractal dimensions close to 2. This concept is easily generalizable to higher dimensions: for a fractal surface, for example, the ruler is replaced with squares of side length l, and N determines how many squares are need to cover the whole surface. Its fractal dimension is between 2 and 3.
Let us briefly return to Eq. (3.2). The equation says that the number of rulers needed, N, scales with the ruler length l as

$$N(l) \sim l^{-d_{\text{box}}} \ , \tag{3.4}$$

i.e. it follows a power law. This type of law is also called scaling law; systems that follow a scaling law are called scale invariant.

3.1.2 Self-similarity, self-affinity, and the Hurst exponent

When constructing the Koch curve, each section is replaced by a small version of itself. When magnifying the Koch curve with the same factor in both the horizontal and vertical direction (isotropically), one finds always exactly the same geometric pattern; the Koch curve is exactly self-similar.
A generalization of self-similarity is self-affinity. For self-affinity, the demand of an isotropic magnification is relaxed. Now it will just be demanded that the ratio between the magnification in the horizontal direction, $x \to ax$ and the vertical direction $y \to by$ can be described by a power law. The exponent that describes the relation between scaling factors a and b,

$$H \equiv \frac{\log a}{\log b} \ , \tag{3.5}$$

is called the Hurst exponent [Bunde and Havlin, 2009]. The concept of self-affinity as opposed to self-similarity becomes clearer when investigating time series instead of fractal geometries. For a geometric object, an isotropic magnification can be defined easily, since both the x-axis and the y-axis have the same physical dimension. One can imagine it as putting a square over a part of the geometry, and magnifying the content of the square. For a time series of measured pressures, on the other hand, the dimensions of the axes are different. The concept of a square in the time-pressure space is meaningless [Mandelbrot, 1985].
In practice, exact self-similarity or self-affinity also happen only for curves that were mathematically constructed. Fractal curves that can be found in the real world, e.g. cauliflower and tree anatomy [ben Avraham and Havlin, 2009] or coast lines [Mandelbrot, 1967], mainly exhibit stochastic self-similarity or self-affinity instead. This means that certain statistical indicators, for example the variance or other moments around the mean, scale with the size of the observation. Following [Kantelhardt, 2011], time series will be called "fractal" if they are statistically self-affine, or if they become self-affine after integration.

3.2 Estimating the Hurst exponent

In the following sections, two different approaches to estimate Hurst exponents of fractal time series will be described. The first subsection deals with the rescaled range approach introduced by [Hurst, 1951], after whom the Hurst exponent is named. The second subsection explains Detrended Fluctuation Analysis (DFA) [Peng et al., 1994], which is used for the estimation of Hurst exponents of pressure time series.

3.2.1 Rescaled range approach

The rescaled range approach was developed by water engineer H.E. Hurst in order to estimate necessary reservoir storage sizes in the Nile river basin. His aim was to have a minimum amount of water available for irrigation every year for one century [Hurst, 1951]. The reservoir can be refilled in years where much water is available. The data records of the in- and outflow of the lakes in the Nile basin did not cover 100 years. Therefore, a way to estimate the range of cumulative in- and outflows (i.e. the reservoir content) over a longer time horizon was needed. The rescaled range approach goes as follows: First, the time series x_i of length $i = 1, 2, ..., N$ is split into segments of size w. The number of segments is $N_s = \text{floor}(w/N)$. If the time series length is not an integer multiple of the segment size, the number of segments can be doubled by processing the signal twice, once forward and once backward. This also makes sure that the data points at the end are not discarded entirely. In each segment ν, the mean of the time series is subtracted,

$$\tilde{x}_{\nu,k} = x_{\nu,k} - \langle x_{\nu,k} \rangle_k \ . \tag{3.6}$$

The index $k = 1, 2, ..., w$ counts locally within the segment, and $\langle \square \rangle_k$ is the mean over indices k. Then, the cumulative sum of the annual flows $\tilde{x}_{\nu,k}$ is calculated for each segment as

$$Y_{\nu,j} = \sum_{k=1}^{j} \tilde{x}_{\nu,k} \ . \tag{3.7}$$

In this equation, each Y_j thus corresponds to the water amount in a reservoir in year j, with observations $\nu = 1, 2, ..., N_s$. For each segment, the range of the cumulative sum R and the standard deviation σ of the underlying time series are calculated. The range is the difference between the maximum and minimum:

$$R_\nu = \max_k(Y_{\nu,k}) - \min_k(Y_{\nu,k}) \tag{3.8}$$

$$\sigma_\nu = \sqrt{\frac{1}{w} \sum_{k=1}^{w} \tilde{x}_{\nu,k}^2} \tag{3.9}$$

The rescaled range is given as the mean of the ratio between the range and the standard deviation over all segments of the same length w,

$$R/\sigma = \langle R_\nu / \sigma_\nu \rangle_\nu \ . \tag{3.10}$$

Hurst found that the rescaled range followed a scaling law with respect to the length of the observation w,

$$R/\sigma \sim w^H \ , \tag{3.11}$$

where H is today called Hurst exponent. It can be estimated using a least square fit in a double logarithmic plot,

$$\log(R/\sigma) = H \cdot \log(w) + K_0 \ , \tag{3.12}$$

where K_0 is a constant due to factors independent of w in Eq. (3.11). Hurst was thus able to estimate the required reservoir storage capacity R from the standard deviation of the in- and outflows σ and the target time scale w, here 100 years.

3.2.2 Detrended fluctuation analysis

Detrended Fluctuation Analysis (DFA) was introduces by Peng *et al.* [Peng et al., 1994] in order to find long-range correlations in DNA sequences. The procedure is as follows: First, the mean of the time series x_i is subtracted

$$\tilde{x}_i = x_i - \langle x_i \rangle \ . \tag{3.13}$$

Then the cumulative sum of the time series is calculated as

$$Y_j = \sum_{i=1}^{j} \tilde{x}_i \ , \tag{3.14}$$

generating a random walk with the underlying time series as step size. Y is also called a profile function. The cumulative time series is divided into segments $\nu = 1, 2, ..., N_s$, each of length w. In each segment, the linear trend is calculated by means of least square fit and subtracted

$$\tilde{Y}_{\nu,k} = Y_{\nu,k} - a_1 \cdot k - a_0 \ , \tag{3.15}$$

where a_1 and a_0 are the polynomial coefficients of the local linear trend, and k is the local index within the current segment. Equation (3.15) is valid for detrending of order 1 (DFA1). Polynomials of higher order can also be used for detrending. Due to the cumulative sum in Eq. (3.14), DFAm eliminates trends of order $m-1$ in the underlying time series [Kantelhardt, 2011]. After detrending, the variance of the values is calculated as

$$\left(\sigma_\nu^{\mathrm{DFA}}\right)^2 = \frac{1}{w} \sum_{k=1}^{w} \tilde{Y}_{\nu,k}^2 \ . \tag{3.16}$$

Figure 3.2 shows the division of the profile function into segments, the linear trends in each segments, and the standard deviation. The range R_ν of each segment, as used for the rescaled range approach described above, is also marked. The root mean of the detrended window variances is taken over all segments in order to estimate the average fluctuation,

$$F^{(2)}(w) = \left(\frac{1}{N_s} \sum_{\nu=1}^{N_s} \left(\sigma_\nu^{\mathrm{DFA}}\right)^2 \right)^{1/2} \ . \tag{3.17}$$

$F^{(2)}$ is called the fluctuation function. The superindex (2) here refers to the order of the root mean, since different orders will later also be used. The procedure

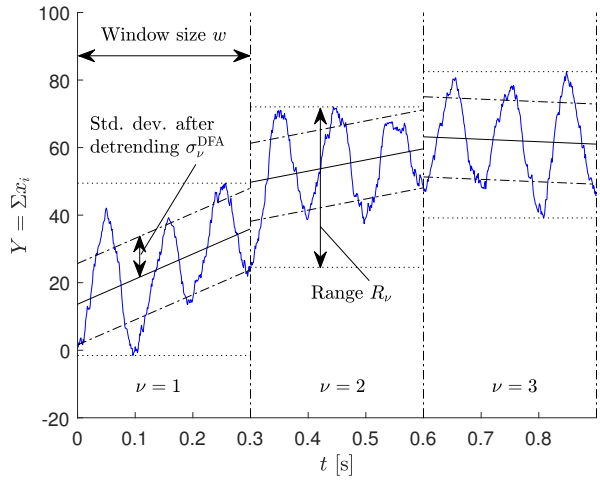

Figure 3.2: Range R_ν and standard deviation after detrending $\sigma_\nu^{\mathrm{DFA}}$ shown for three segments of the profile function Y. The underlying time series x_i is the sum of a sine wave with frequency $f = 10$Hz and a standard normally distributed noise.

is repeated for different segment sizes w. For self-affine fluctuations, the Hurst exponent determines the scaling law between the segment size and the fluctuation function,

$$F^{(2)} \sim w^H \ . \tag{3.18}$$

Figure 3.3 gives an example of the rescaled range, Fig. 3.3(a), and the fluctuation functions, 3.3(b), of three artificial signals. In white noise, no correlations are present per definition and the corresponding Hurst exponent is $H = 0.5$. Pink noise is long-term positively autocorrelated. This is reflected in the value of the Hurst exponent $H = 1$.
The picture is more complicated for the sine wave with added white noise. Both the rescaled range and the fluctuation function scale like white noise only at very small and very large time scales. At the time scale of one sine period, $w/f_s = 0.1\,\mathrm{s}$, one can see a clear knee in both function plots. This abrupt change in scaling behavior is called a crossover. For time scales slightly smaller than one full period, both the rescaled range and the fluctuation function increase strongly. The slope here is 1 for the rescaled range and 2 for the fluctuation function; these are both the maximum possible values as estimated by the respective method. For time scales larger than one full period, the functions are almost flat. A time series like this can therefore not be described by a single Hurst exponent. The reason is that the statistics of a sine wave do not change when increasing the time horizon from one to several periods. In the very long term, on the other hand, the noise becomes relatively more important, and the rescaled range and fluctuation function increase with the

square root of the time scale.

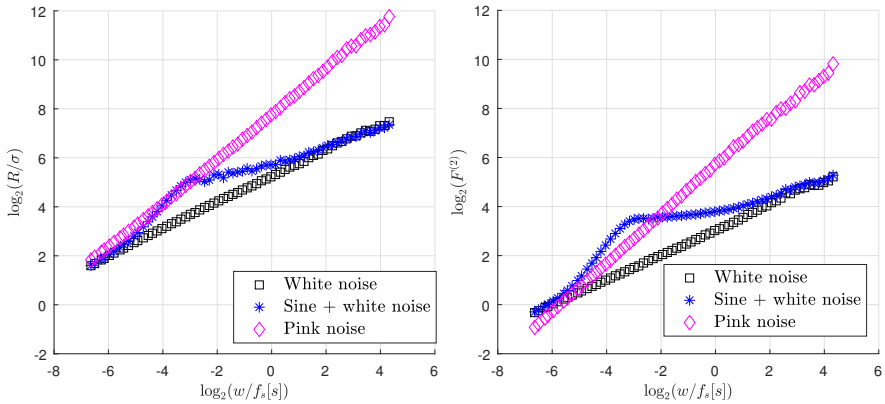

(a) Rescaled range R/σ (b) Fluctuation function $F^{(2)}$

Figure 3.3: Scaling laws for three different artificial signals: (1, black) Gaussian white noise, (2, blue) a sine wave with a frequency of 10 Hz and added Gaussian white noise, and (3, magenta) pink noise.

Using the rescaled range approach, Fig. 3.3(a), oscillations at window sizes slightly larger than one sine period can be seen. These are less pronounced in the fluctuation function return by DFA, Fig. 3.3(b). The estimate of the Hurst exponent through a linear fit has a smaller error. Since the time scales we are interested in are in this range as will be shown in Section 3.5, this gives the DFA algorithm better characteristics compared to the rescaled range approach. Other advantages include the possibility of explicitly removing trends and the generalization to multifractality shown in Section 3.2.4. Therefore, DFA will be used to estimate Hurst exponents for the remainder of this work.

3.2.3 Relation to spectral estimates

For time series that are stationary, the Hurst exponent can also be estimated from the power spectrum. R_{xx} is used to denote the autocorrelation of x and S_{xx} to denote its discrete Fourier transform, the power spectral density:

$$R_{xx}(t) = \langle x_i x_{i+t} \rangle_i = \frac{1}{N-t} \sum_{i=1}^{N-t} x_i x_{i+t} \tag{3.19}$$

$$S_{xx}(\omega) = \frac{1}{T} \sum_{t=0}^{T} R_{xx}(t) \cdot e^{-i\omega t} \ , \tag{3.20}$$

where t is a discrete time delay (in samples) and ω is a discrete frequency (in rad/sample). Time series that are long-term correlated have a power spectral density that scales with the frequency ω,

$$S_{xx} \sim \omega^{-\beta} \ . \tag{3.21}$$

An uncorrelated time series (white noise) has a value of $\beta = 0$. For positive long-term correlations, $\beta > 0$. The relation between Hurst exponent H and β is

$$H \approx \frac{1+\beta}{2} \ , \tag{3.22}$$

see [Kantelhardt, 2011]. [Heneghan and McDarby, 2000] discuss this relation and also present a way to estimate the Hurst exponent from the power spectrum.
Figure 3.4 gives an example of the power spectra of three artificial signals also shown in Fig. 3.3. White noise is characterized by equal signal power in all frequency bands, $S_{xx} = \text{const.}$, and thus $\beta = 0$. The power spectral density of pink noise decays anti-proportionally with the frequency, $S_{xx} \sim \omega^{-1} \Rightarrow \beta = 1$. Comparing Fig. 3.4 with Fig. 3.3, one can see that Eq. (3.22) is fulfilled for the white noise and pink noise shown. For signals that contain sine waves, the power spectrum shows a distinct peak at the sine frequency, and the slope β is hard to define; Eq. (3.22) is not valid in this case.

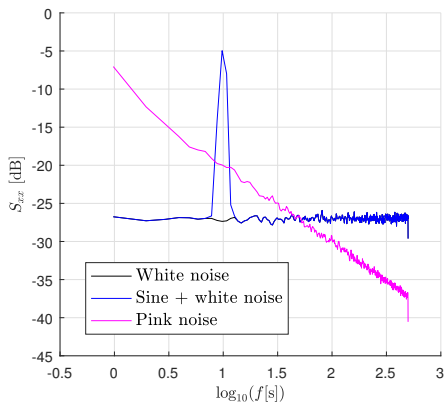

Figure 3.4: Power spectral density of three artificial signals: (1, black) Gaussian white noise, (2, blue) a sine wave with a frequency of 10 Hz and added Gaussian white noise, and (3, magenta) pink noise. (1) and (2) can be distinguished only at the sine frequency. (3) follows a different scaling law over all frequencies.

3.2.4 Multifractal detrended fluctuation analysis

As could be seen from Fig. 3.3, it is often not possible to describe the scaling law for the fluctuation function with a single exponent. The reason is a crossover in the

scaling behavior. There is, however, also another case where a single exponent is not sufficient: if the time series displays multifractal characteristics. Time series are called multifractal if small and large fluctuations scale differently. In order to investigate a time series for multifractality using DFA, Eq. (3.16) is generalized in the following way:

$$F^{(q)}(w) = \left(\frac{1}{N_s} \sum_{\nu=1}^{N_s} \left(\sigma_\nu^{\mathrm{DFA}} \right)^q \right)^{1/q} \tag{3.23}$$

where q is a real number. For $q = 2$, Eq. (3.23) is equivalent to Eq. (3.16). For $q > 2$, segments with large fluctuations are weighted more strongly in the averaging procedure. The estimated fluctuation function will thus describe the scaling behavior of large fluctuations. For $q < 2$, and especially negative q, the segments with small fluctuations will be weighted more strongly. The fluctuations function will thus describe the scaling behavior of small fluctuations. For $q = 0$, Eq. (3.23) is not defined and replaced by

$$F^{(0)}(w) = \exp \left\{ \frac{1}{2N_s} \sum_{\nu=1}^{N_s} \ln \left(\left(\sigma_\nu^{\mathrm{DFA}} \right)^2 \right) \right\} , \tag{3.24}$$

see [Kantelhardt, 2011]. Calculating a linear fit in the log-log plot of $F^{(q)}$ over w gives then $H^{(q)}$, which can be understood as a generalized Hurst exponent of order q. To avoid confusion, the order is always denoted in the remainder of this thesis. Henceforth the "normal" Hurst exponent will therefore be referred to as $H^{(2)}$.
As described above, a time series is monofractal if all fluctuations follow the same scaling law, i.e. $H^{(q)} \neq f(q)$. If, on the other hand, $H^{(q)} = f(q)$, the time series is multifractal. Figure 3.5 gives examples of the fluctuation functions of monofractal data and multifractal data. The monofractal data in Fig. 3.5(a) is a standard normally distributed random variable. The multifractal data in Fig. 3.5(b) is generated using the binomial multifractal model [Kantelhardt, 2011]. Although the absolute value of the fluctuation functions differs, the slope is approximately the same for all orders q, and thus the Hurst exponents $H^{(q)}$ are also the same. The slope depends on the order q.

3.3 A note on the performance of the algorithm

The runtime of the DFA algorithm depends strongly on its implementation. Appendix A shows how the code can be improved from a straightforward implementation of Eqs. (3.13) to (3.17). Table 3.1 compares the runtimes of four DFA algorithm implementations. The sample signal consisted of 100,000 standard normally distributed random values. The scaling of the fluctuation function was calculated over 48 logarithmically spaced window sized from 10 samples to $100,000/6 = 16,667$ samples. The normal and optimized MFDFA algorithms correspond to the MATLAB codes shown in Appendix A. The C++ implementation uses the Eigen template library

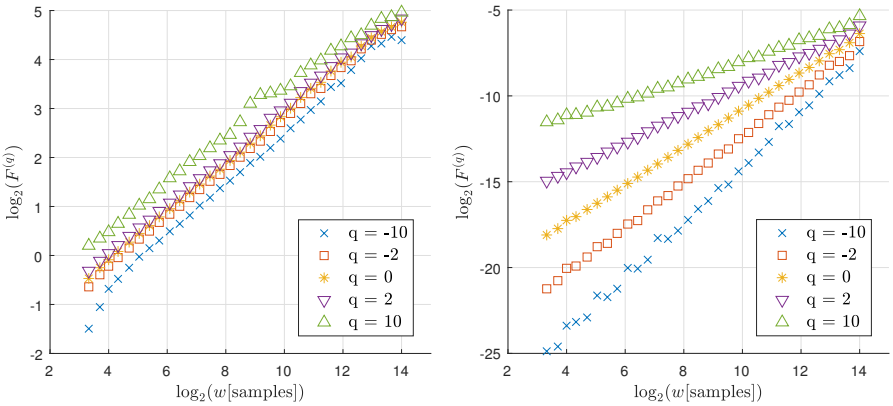

(a) Monofractal data (b) Multifractal data

Figure 3.5: Fluctuation functions of of monofractal (left) and multifractal (right) data. For monofractal data, the slope of the fluctuation function $H^{(q)}$ is the same for all q. For multifractal data, the slope depends on the order q.

[Eigen, 2016] to compute the fluctuation functions, but uses the same algorithm. The FastDFA implementation by [Little et al., 2006] and [Little, 2006], allows only DFA1 and does not compute orders of the Hurst exponent other than $H^{(2)}$; its advantage is that the linear least-square fit is hard-coded, allowing for a very fast calculation. The results from Table A.3 show that compiled code is also able to calculate Hurst exponents in real time for most sampling rates. If the window sizes over which the Hurst exponent is calculated are relatively large (as is the case for e.g. compressor surge due to the large time scales), the runtime improves significantly.

Algorithm/Implementation	Runtime [s]
Normal MFDFA (MATLAB)	62
Optimized MFDFA (MATLAB)	1.19
Optimized MFDFA (mex/C++)	0.118
FastDFA (mex/C++)	0.055

Table 3.1: Runtime of DFA1 for 100,000 samples on a single core (Intel Xeon, 3.40 GHz). The runtimes are averaged over 10 runs and rounded to the first significant digit of the runtime standard deviation.

3.4 The Hurst exponent in mechanical engineering applications

Probably the first application of the Hurst exponent to engineering problems was by Hurst himself as described in the beginning of subsection 3.2.1. While many of the investigations using the fractal methodologies and Hurst exponent since then were done in fields like physics (especially geophysics and biophysics) and finance, studies in the last 30 years have also started to focus on research topics from different fields of mechanical engineering. [Sreenivasan and Meneveau, 1986, Sreenivasan and Meneveau, 1988, Sreenivasan, 1991] investigated the fractal dimensions of different surfaces in turbulent flows (like the boundary between turbulent and laminar flow), as well as absolute values of vorticity and Reynolds stresses. He found that e.g. the surface mentioned above has fractal properties, and that multifractal sets can be used to describe the scaling of absolute vorticity and Reynolds stress in turbulent flows. [Gouldin, 1987, Gouldin et al., 1989] investigated fractal properties of flamelets and came to the conclusion that their surfaces can be described by fractals. More recently, [Nair et al., 2013, Nair and Sujith, 2014] used DFA to estimate Hurst exponents of pressure time series in combustors in order to detect the onset of instabilities. Their result is that the Hurst exponent has some advantages over traditional indicators such as the RMS in detecting the onset of instabilities, and that the pressure oscillations could more accurately be described as chaotic (as opposed to random). [Venkatramani et al., 2017] used the same methods to find precursors to blade flutter from an airfoil in a wind tunnel. They found multifractal properties of the plunge and pitch time series before the onset of flutter, and a monofractal behavior with a Hurst exponent $H^{(2)} \approx 0$ during blade flutter.

3.5 Application of the Hurst exponent as surge indicator

The principal idea behind the application of the Hurst exponent as surge indicator is analogous to the one used in [Nair and Sujith, 2014] for combustion instabilities. At stable operation, the pressure signals are dominated by turbulent pressure fluctuations and noise. These fluctuations are long-term autocorrelated, and the Hurst exponents should be in range $1 > H^{(2)} > 0.5$ over several orders of magnitude. As compressor operation moves closer to surge, pressure time series become more ordered. Small oscillations begin to appear with the system eigenfrequency, creating a crossover at a time scale of one mild surge period. The Hurst exponent for these time scales decreases, owing to the fact that the signal becomes negatively autocorrelated. Once the system reaches a limit cycle, the operation repeats periodically and the Hurst exponent is theoretically zero.

The application of the Hurst exponent to compressor surge is tested in the following chapters. Chapter 4 describes the experimental setup used. Chapter 5 gives an overview over the results, also published in papers I, II, III, and IV. The results are

concluded, and proposals for future work are presented in Chapter 6.

4 Experimental setup

As part of the investigations described in this thesis, several sets of measurement data are used: A light duty turbocharger run on a cold gas stand, a heavy duty turbocharger run on a cold gas stand, and a heavy duty turbocharger run on an engine. The experimental setup used to acquire data on the light duty turbocharger is described in this chapter. Further measurements on the same turbocharger on an acoustic test rig were carried out by [Kabral et al., 2013]. The data set for the heavy duty turbocharger on a cold gas stand was obtained by [Guillou, 2011, Gancedo, 2014] at the University of Cincinnati, and the reader is referred to their PhD theses for a description of the experimental setups. The data set for a heavy duty turbocharger on an engine was acquired as part of the project course in internal combustion engines. The experimental setup is described in the course report [Hamberg et al., 2015].

4.1 The cold gas stand

4.1.1 The CICERO lab

Turbocharger experiments were run in the CICERO lab located, located in the basement of the Fluid Physics Laboratory of the KTH Mechanics Department. The principal layout is sketched in Fig. 4.1. Two crew compressors located in a rock shelter, each capable of delivering $\dot{m} = 0.26\,\mathrm{kg/s}$ at a total pressure of $p_t = 5.5\,\mathrm{bar}$, feed a settlement chamber tank. From the rock shelter, the air is supplied into the test chamber. Mass flow into the test chamber is measured by a hot film type flow meter. It is regulated by two parallel pneumatic valves located downstream. The main valve leads through an electric heater to the cold gas stand. The bypass valve leads directly to the exhaust and allows for flow stabilization at low mass flows.
The heater has a rated power of $\dot{Q} = 18\,\mathrm{kW}$. It is thus not able to heat the air to exhaust-gas like temperatures. Its purpose is to increase the turbine air inlet temperature so that temperatures $T_{\mathrm{out}} > 0\,^{\circ}\mathrm{C}$ are achieved after expansion, in order to avoid icing at the turbine exit. The gases are then dumped into the exhaust collector.
The turbocharger hydrodynamic bearings are lubricated with the help of the oil supply circuit. The static pressure of the oil fed is regulated by a manual valve.

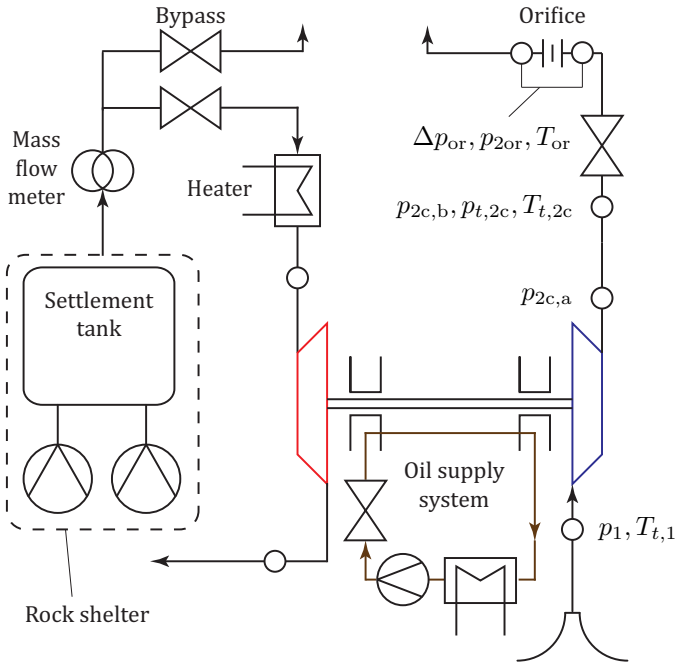

Figure 4.1: Layout of the facility

Its inlet temperature is also monitored and kept constant with the help of a small electric heater. Oil coming from the bearings is cooled down using a heat exchanger with room temperature water.

4.1.2 The turbocharger

The passenger car turbocharger used in the investigations is of type Garrett GT1752. Its impeller has six full blades and six splitter blades. The inducer tip diameter is $D_{1t} = 39.8\,\text{mm}$ and the exducer tip diameter is $D_2 = 52\,\text{mm}$, resulting in a TRIM value of

$$\text{TRIM} = \left(\frac{D_{1t}}{D_2}\right)^2 = 0.53\ . \tag{4.1}$$

The blades are backward swept at the exducer tip. Following the impeller is a vaneless space and a vaneless diffuser. At the outlet of the diffuser, a volute scroll collects the flow and guides it towards the exit. The compressor design corrected mass flow is $\dot{m}^*_{\text{corr}} = 115\,\text{g/s}$, which corresponds to a mass flow parameter of $\phi_{01} = 0.10$. The design blade Mach number is $\text{Ma}_{\text{u2}} = 1.09$ using inlet stagnation conditions. Maximum speed is $n_{\text{corr}} = 180\,\text{krpm}$, which corresponds to a Mach

number of $Ma_{u2} = 1.41$. The local flow Mach numbers are lower than that, since the air is heated up in the impeller.

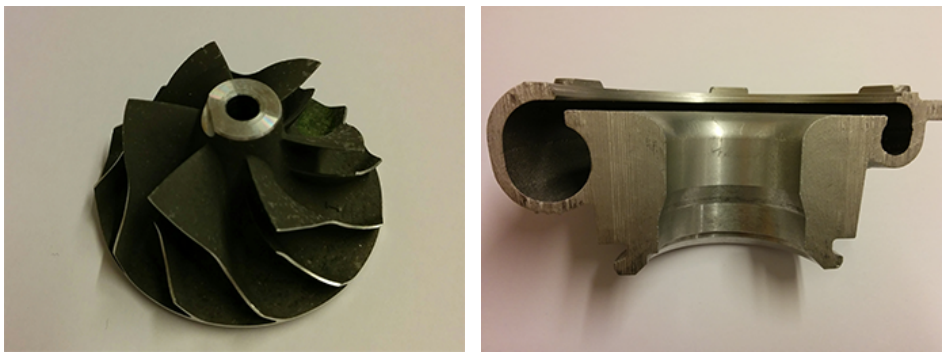

(a) Impeller (b) Stator (side-view)

Figure 4.2: GT1752 compressor components

4.2 Instrumentation and measurement

4.2.1 Sensors and positioning

The sensor positioning was done similar to the [SAE, 1995a] Turbocharger Gas Stand Test Code. Sensor locations are marked as white circles in Fig. 4.1. On the compressor inlet side, the flow is induced from the test chamber by a funnel. Total
the inlet duct. The inlet duct has a length of $L = 12...17\,D$, depending on inlet configuration. In the experiments where a 90 ° bend leads into the compressor, two further pressure measurements are taken after the bend at the same streamwise, but different circumferential locations. After the compressor, a straight pipe leads to the throttle $17\,D$ downstream the volute exit. An image of the compressor inlet and outlet piping for a configuration with a bend inlet is shown in Fig. 4.3.
There is no distinct compressible plenum, as described in the surge model in Section 2.3.2. This is done in order to keep the pressure oscillations amplitude relatively small during surge, which helps to avoid damaging the components. Time-resolved static wall pressure measurements are acquired $3\,D$ and $10\,D$ downstream the volute exit. Time-averaged static and total pressure as well as total temperature are measured $11\,D$ downstream the volute exit. Mass flows are estimated from the pressure drop over an orifice far downstream the throttle valve. The orifice method is chosen to achieve a high accuracy average in mass flow measurements even with mild surge oscillations present. A list over the sensors is given in Table 4.1.

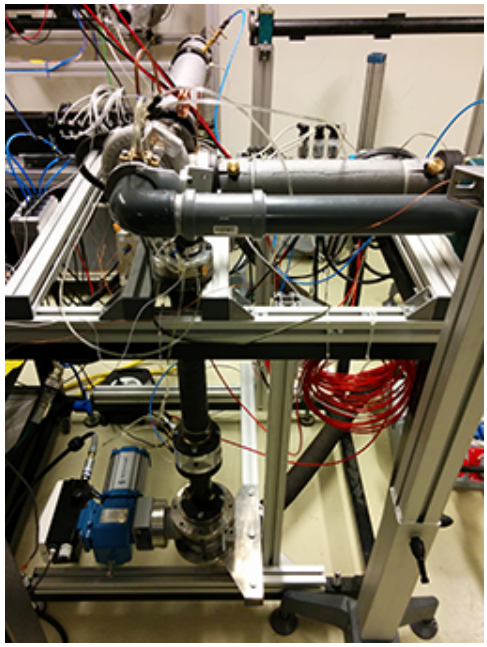

Figure 4.3: Inlet and outlet piping for the configuration with a bend at the compressor inlet.

4.2.2 Data acquisition

Compressor operating points are measured along a speedline from high mass flows towards the surge line, as proposed by the standard [SAE, 1995a]. The criterion for steady-state operation (in the non-surge points) is that the isentropic efficiency, Eq. (2.5), fluctuates with an amplitude of less than 0.3 %-points around a constant mean value. Sampling duration was at least 10 seconds for all operating points, but 90 seconds for the data points on which the Hurst exponent is calculated. This very long sampling time allows for the calculation of many Hurst exponents and thus also an accuracy estimate of the method.
Data is acquired with the help of a National Instruments compact RIO system, type cRio-9104. Table 4.2 lists which C module is used to sample the data for each sensor. A real-time program on the RIO system calculates pressures and the impeller speed from the voltage signals and stores them in three target-to-host direct memory access buffers, one for each fast sampling frequency. These buffers are read out periodically by a LabVIEW VI running on the host computer and further processed.

Meas.	Sensor type	Range	Accuracy	Sampl. freq.
p_{1c}	MPX2010	10 kPa diff.	±1.0% (max. lin.)	500 Hz
p_{2c}	MPX5050	50 kPa diff.	±2.5% (max. tot.)	500 Hz
$p_{t,2c}$	Gems 2200SGA6	0...6 bar gauge	±0.25% (typ. lin.)	500 Hz
p_{2or}	MPX5050	50 kPa diff.	±2.5% (max. tot.)	500 Hz
Δp_{or}	MPX5050	50 kPa diff.	±2.5% (max. tot.)	500 Hz
$p_{1c,a}$	Kulite WCT312	0...1.7 bar abs.	±0.5% (max. tot.)	10.24 kHz
$p_{1c,b}$	Kulite WCT312	0...1.7 bar abs.	±0.5% (max. tot.)	10.24 kHz
$p_{2c,a}$	Kistler 4045A5	0...5 bar abs.	±0.1% (typ. lin.)	10.24 kHz
$p_{2c,b}$	Kistler 4045A5	0...5 bar abs.	±0.1% (typ. lin.)	10.24 kHz
$T_{t,1c}$	Type K	−270...1260 °C	±2.2 °C	2 Hz
$T_{t,2c}$	Type K	−270...1260 °C	±2.2 °C	2 Hz
$T_{t,2or}$	Type K	−270...1260 °C	±2.2 °C	2 Hz
N	Micro-epsilon	–	–	$12N$

Table 4.1: Overview over the installed sensors. Note that the accuracy is defined differently for different suppliers and cannot be compared directly with each other.

Module	Channels	Resolution	Data sampled
NI 9205	16 (diff.)	16-Bit	Low-freq. pressure sampling
NI 9213	16	24-Bit	Thermocouples
NI 9234	4	24-Bit	High-freq. pressure sampling (built-in filter)
NI 9401	8	Digital	Impeller speed

Table 4.2: C series modules used to acquire data from the sensors.

4.2.3 Measurement accuracy and repeatability

The accuracies given in Table 4.1 are stated as specified in the respective data sheet of the measurement device and are not directly comparable. For the pressure sensors, they may include only the deviation of the true pressure - output voltage curve from a linear fit (marked as "lin."), or they may include other factors such as drift due to temperature and hysteresis effects (marked as "tot."). It further needs to be distinguished between errors that are specified as maximum error, and those specified as typical error. Errors in long-term drift are compensated for, since the sensors were calibrated before testing began and periodically re-calibrated.
Since one of the principle aims of this thesis is an investigation of the onset of surge, the mass flow is an important parameter. It is estimated using the pressure drop over and the local temperature after the orifice. The accuracy of the mass flow measurement can then be estimated using a Monte-Carlo simulation. $10,000$ artificial values, independent and identically distributed, are created of each input variable Δp_{or}, p_{2or}, and $T_{t,2or}$. They are assumed to be normally distributed

with a standard deviation of 1/3 of the uncertainty specified in Table 4.1, so that 99.73% of samples conform to the accuracy stated for the pressure sensor. Given the data sheet states the accuracy as maximum total, this can be considered a conservative assumption. For three typical mass flows, standard deviation and 95% confidence interval are given in Table 4.3. Since the estimate is not based on actual observations, these uncertainties can be considered a type B standard uncertainty [Coleman and Steele, 2009]. As can be seen from Table 4.3, uncertainties are larger at low mass flows, even in an absolute sense. This occurs because at low mass flows, the mean pressure difference Δp_{or} is small, but the variation is still the same (since the specified accuracy is relative to the full range). Especially at the lowest mass flow simulated, the assumption that the pressure sensor will return a signal of $\Delta p_{\mathrm{or}} = (5 \pm 0.417)\,\mathrm{kPa}$ seems very questionable. In order to get a better estimate of the measurement accuracy, the type A uncertainties were therefore also determined. The type A uncertainty is estimated by repeating measurements of the same com-

mean($\dot{m}$) [g/s]	std($\dot{m}$) [g/s]	std/mean [%]	95% conf. [g/s]
46.6	1.9	4.1	$[42.7, 50.2]$
84.5	1.1	1.3	$[82.3, 86.5]$
127.1	0.8	0.6	$[125.5, 128.6]$

Table 4.3: Type B uncertainties of the mass flow calculation from the orifice, calculated with a Monte-Carlo simulation using the sensor accuracies stated in Tab. 4.1.

pressor operating point at several occasions. In this case, three operating points were measured at least five times each over two days. The standard deviation of these mass flows is $s_{\mathrm{MF}} = 0.3...0.5\%$ of the mean, depending on the operating point. This is significantly better than the type B uncertainty estimated above. For the total pressure ratio $\mathrm{PR}_{\mathrm{t-t}}$, the type A uncertainty is estimated from the same operating points as $s_{\mathrm{PR}} \approx 0.15\%$ of the mean.

5 Results and discussion

5.1 Verification

5.1.1 The Hurst exponent as surge indicator

The first step in the verification of this method is to establish that the Hurst exponent can reasonably be defined for the given signal. This requires that the fluctuation function $F^{(2)}$ follows a scaling law with respect to the segment size w over one order of magnitude [Kantelhardt, 2011]. As a first step, the outlet pressure $p_{2\mathrm{ca}}$ at two operating points along a speedline $n_{\mathrm{corr}} = 120\,\mathrm{krpm}$ is evaluated for the light duty turbocharger compressor. The first point, denoted stable, is at a corrected mass flow of $\dot{m}_{\mathrm{corr}} = 91.3\,\mathrm{g/s}$, which corresponds approximately to the design mass flow at this speedline. The second point, denoted near surge, is at a corrected mass flow of $\dot{m}_{\mathrm{corr}} = 36.6\,\mathrm{g/s}$, and is on the surge line defined by subjective operator noise. This definition will be used throughout this chapter unless stated otherwise. Figure 5.1(a) shows excerpts of the both pressure signal time series. One can observe a clear difference already between the very small fluctuations in the stable case, and much larger, approximately harmonic oscillations that appear and disappear in the near surge case.
The fluctuation function is calculated first over all time scales. The smallest segment size is $w = 10$ samples. The largest one is chosen as 1/4 of the total signal length. Results are shown in Fig. 5.1(b). The Hurst exponent corresponds to the linear least square fit of $\log(F^{(2)})$ over $\log(w)$. It can be seen that a single Hurst exponent over all time scales cannot be defined, since the fluctuation functions do not have a constant slope. The description via a single Hurst exponent, however, is neither expected nor is it necessary. Instead, as was also shown for the artificial sine signal with added noise (cp. Fig. 3.3(b)), a crossover at one period of the oscillations is expected. The crossover, a sudden change in slope of the fluctuation function, can clearly be seen for a value of

$$\log_2(w/f_s[\mathrm{s}]) = -5 \quad \Rightarrow \quad \frac{w}{f_s} = \frac{1}{32}\frac{1}{\mathrm{s}}\,. \tag{5.1}$$

That means that as the segment size is extended beyond 1/32 s, the signal variance after detrending is almost independent of segment length, a typical effect of repeating

patterns in the signal. Over this range, the scaling law of both fluctuation functions can approximately be described using a single Hurst exponent. In the case of these measurements of the GT1752 compressor on the cold gas stand, the segment interval chosen to estimate $H^{(2)}$ is thus $[1/32, 8/32]$ seconds, see also [Kerres et al., 2016b]. The frequency of 32 Hz also is very similar to the compression system eigenfrequency estimated from a Helmholtz resonator model, cp. Section 2.3.2 and [Kerres et al., 2016a]. For other compression systems, a similar analysis was performed, and similar conclusions could be made [Kerres et al., 2017a, Kerres et al., 2017b].

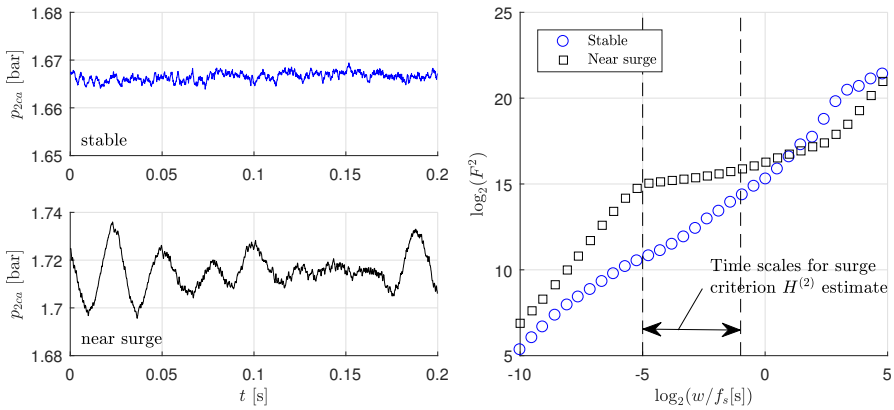

(a) Pressure signals (b) Fluctuation functions

Figure 5.1: Time series and fluctuation function of the compressor outlet pressure signal $p_{2\mathrm{ca}}$ at two mass flow on the speedline $n_{\mathrm{corr}} = 120\,\mathrm{krpm}$. The signals were split into parts of 2 seconds length in order to obtain 40 approximately independent samples; symbols show the mean and error bars the standard deviation of these samples.

Next, the analysis using the Hurst exponent will be extended to three speedlines with corrected speeds $n_{\mathrm{corr}} = \{80,\ 100,\ 120\}\,\mathrm{krpm}$. Pressure measurements both from the cold gas stand and the acoustic test rig, cp. [Kabral et al., 2013], are used. As a benchmark surge indicator based on pressure measurements, the Root Mean Square (RMS) of the pressure fluctuations normalized with the inlet stagnation density $\rho_{\mathrm{t},1}$ and impeller tip speed u_2 is employed,

$$p_{\mathrm{rms,rel}} = \frac{\mathrm{RMS}(p')}{\rho_{\mathrm{t},1} u_2^2} \ . \tag{5.2}$$

Figure 5.2(a) shows the resulting RMS values, and Fig. 5.2(b) the Hurst exponents over the mass flow parameter ϕ_{01}. The error bars show the standard deviation. They were generated by dividing the signal into segments of 2 seconds sampling

length and performing the respective calculation on each segment.
The relative pressure fluctuation RMS values of cold gas stand operation, Fig. 5.2(a), are around $p_{\mathrm{rms,rel}} = 0.3\%$ for mass flow parameters $\phi_{01} \geq 0.08$. If operation is throttled further from this operation point, they increase exponentially towards ca. $p_{\mathrm{rms,rel}} = 2.2...2.5\%$ at the surge line. The error bars are small except at the surge line, where small envelopes of mild surge occur, cp. Fig. 5.1(a).
On the acoustic test rig, the similar RMS values are observed at high ϕ_{01}. At the surge line, however, the values are much lower at $p_{\mathrm{rel,rms}} < 1\%$. This is due to the fact that silencers are mounted at the inlet and outlet of the compression system, dampening acoustic pressure oscillations. On the acoustic rig, error bars are small even in near surge operation; alternating periods of larger and smaller mild surge oscillations such as displayed in Fig. 5.1(a) on the cold gas stand are not present here.

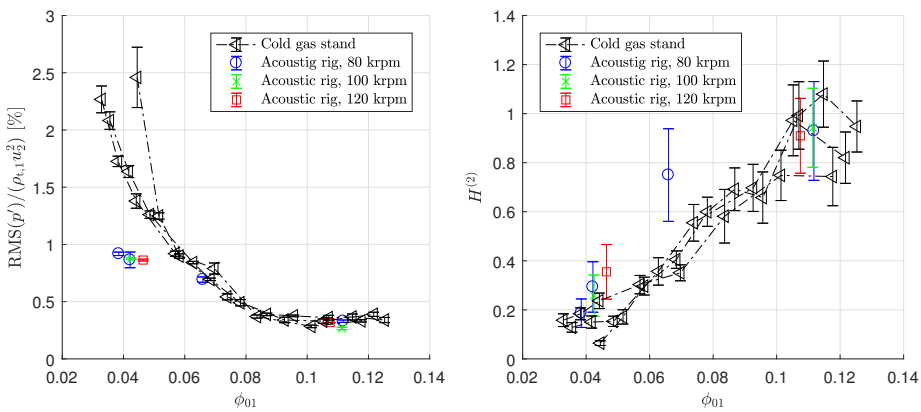

(a) Pressure fluctuation RMS (b) Hurst exponent

Figure 5.2: Fluctuation RMS value and Hurst exponent over the system natural frequencies for the compressor outlet pressure signal $p_{2\mathrm{ca}}$ at the speedlines $n_{\mathrm{corr}} = \{80, 100, 120\}$ krpm.

The Hurst exponents for the same data points are shown in Fig. 5.2(b). At high mass flow parameters, $\phi_{01} \geq 0.11$, their values are $H^{(2)} = 0.8...1$, with standard deviations of approximately 0.1. The decrease of $H^{(2)}$ towards surge starts earlier than the corresponding increase in the RMS values. This indicates that the Hurst exponent could be more useful to detect surge precursors. The decrease towards surge is approximately linear, reaching values as low as $H^{(2)} = 0.06$ at the surge line for $n_{\mathrm{corr}} = 120$ krpm. The error bar spread decreases the closer operation moves to surge. The near-surge Hurst exponents of gas stand and acoustic rig operation are similar with $H^{(2)}$ from the acoustic rig being slightly higher. A clear disagreement

between both test rigs can be seen for the data point $\phi_{01} = 0.065,\ n_{\mathrm{corr}} = 100\,\mathrm{krpm}$. The reason for that is that there are strong oscillations with a higher frequency ($f \approx 150\,\mathrm{Hz}$) in the operating point on the acoustic rig. The oscillations increase the RMS value, but do not decrease the Hurst exponent since these are calculated over different time scales.

For the heavy duty turbocharger, a similar investigation is performed. Since it is combined with a sensitivity analysis with respect to sensor location, the results are shown in the next section in Fig. 5.5. For this part of the investigation, it should suffice to observe the outlet pressure signal p_{out}. At the top of these figures, the sign of the local compressor speedline slope is stated. As shown in Section 2.3.2, this slope is important for compression system stability. Since the local throttle slope is unknown, the exact stability criteria on this test bench could not be evaluated; assuming it to be large, $\partial\psi_{\mathrm{T}}/\partial\phi_{\mathrm{T}} \gg 1$, leads to an onset of dynamic instability at mass flows slightly lower than the peak $\mathrm{PR}_{\mathrm{tt}}$ mass flow.
For this compressor, the RMS values at high mass flows are around $p_{\mathrm{rms,rel}} \approx 0.9\%$. At $\phi_{01} = 0.45$, the RMS increases to $p_{\mathrm{rms,rel}} \approx 1.3\%$. There is no steady increase towards the surge line as could be observed for the passenger car compressor. This means that it would be difficult to implement a surge warning based on $p_{\mathrm{rms,rel}}$ for this compressor. Deep surge, which is also shown in Fig. 5.5(a), is characterized by pressure fluctuations of approximately 10% of the reference value $\rho_{\mathrm{t},1}u_2^2$.
The Hurst exponents, cp. Fig. 5.5(e), show a very similar behavior for the large compressor as for the light duty one. In stable operation, $H^{(2)}$ values are slightly lower. This is mainly due to the much shorter sampling time – 5 seconds – for the heavy duty compressor; therefore, long-term trends due to system drift are less pronounced. The approximately linear decrease of the Hurst exponents towards surge looks comparable to the one for the light duty compressor, but the surge line values are higher. Deep surge is characterized by very low Hurst exponents in the range $H^{(2)} \approx 0.05$.

This comparison of the results for the light duty compressor, tested in two different compression systems, as well as the heavy duty compressor shows that the Hurst exponent has potential for surge detection and classification in two ways. The limit value of $H^{(2)} = 0$ for pure oscillations is system-independent, while values around $H^{(2)} = 0.5...1$ have been found for stable operation on three compression systems. The second possible advantage over traditional signal characteristics such as RMS is that there seems to be a steady decrease towards 0 between stable operation and the onset of instabilities, at least at lower compressor speeds. This could be beneficial when developing a surge precursor detection algorithm.

5.1.2 Mono- and multifractality near surge

As described in Section 3.2.4, DFA also allows to distinguish between oscillations of different amplitudes by applying a weight to the local fluctuations. This methods

returns a set of Hurst exponents $H^{(q)}$ for a range of q as different orders. For $q < 0$, $H^{(q)}$ is dominated by the small fluctuations, while for $q > 2$, it is dominated by the large fluctuations. The idea here is that the compression system oscillations are expected to be large compared to hydrodynamic turbulent fluctuations and signal noise, and thus more information about system stability can be gained by evaluating a set of Hurst exponents.
A common way to present this set of Hurst exponents is via the singularity spectrum. This spectrum decomposes the signal into a set of interwoven fractals. It is generated by first calculating a Renyi scaling exponent [Kantelhardt, 2011]

$$\tau(q) = H^{(q)}q - 1 \ , \tag{5.3}$$

and then using the Legendre transform to change from the $q - \tau(q)$ space to a new space defined by

$$\alpha = \frac{\mathrm{d}\tau(q)}{\mathrm{d}q} = H^{(q)} + q\frac{\mathrm{d}H^{(q)}}{\mathrm{d}q} \tag{5.4}$$

$$f(\alpha) = q\alpha - \tau(q) \tag{5.5}$$

In this equation, α is the singularity strength and $f(\alpha)$ is the dimension of the signal parts characterized by this strength. For $q = 0$, $\tau(q) = -1$, $\alpha = H^{(0)}$ and $f(\alpha) = 1$. For a monofractal signal, all $H^{(q)} \equiv H$ are the same and thus $\alpha = H$ and $f(\alpha) = 1$, that is, the singularity spectrum collapses into a single point. For the singularity spectrum to be defined over a range of α, the Renyi scaling exponent $\tau(q)$ needs to have a unique slope in each point. This is the case for concave and convex functions.

Renyi scaling exponents are plotted in Fig. 5.3 for the light duty turbocharger. On the left side, Fig. 5.3(a), are the results from the acoustic test rig. All points measured are plotted there. On the right side, Fig. 5.3(b), one speedline $n_{\mathrm{corr}} = 120\,\mathrm{krpm}$ from the cold gas stand measurements is plotted. The color indicates the mass flow parameter, with warm colors for high mass flows, and cold colors for low mass flows. On both test setups, near surge mass flows are characterized by a concave $\tau(q)$ function, i.e. a multifractal pressure signal at system natural time scales. Most stable operating points, on the other hand, show a monofractal outlet pressure signal. An interpretation is that at stable operation, both large and small fluctuations come from the same sources, e.g. noise and turbulence. At instable operation, small fluctuations mainly come from these sources, while large fluctuations are due to system instability and are characterized by a lower Hurst exponent.

The corresponding singularity spectra are shown in Fig. 5.4. Four approximately comparable operating points near surge are shown for both rigs; given that the compression systems are significantly different, however, it is not given that these points represent same system stability. A wide spectrum means that the pressure signal is characterized by many fractals of different strength, while a narrow spectrum means

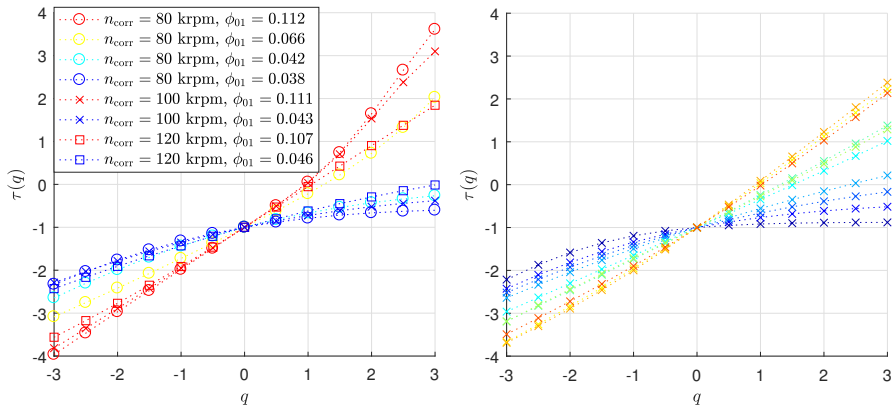

(a) Acoustic test rig

(b) Cold gas stand, $n_{corr} = 120\,\text{krpm}$

Figure 5.3: Order q and Renyi scaling exponent $\tau(q)$ for the light duty compressor run on the acoustic test rig (all points), and along the speedline $n_{corr} = 120\,\text{krpm}$ on the cold gas stand.

that it is closer to a single fractal. The operating points at $n_{corr} = 80\,\text{krpm}$ show similar singularity spectra for both compression systems, although the signals look very different in both time and frequency domain. At the two higher speedlines, results from the cold gas stand show wider spectra. The increase in width happens on the left hand side of the maximum and corresponds to positive orders q. The spectra extend almost until $\alpha = 0$; higher orders q would lead to $\alpha < 0$. Negative α values can for example be found if the oscillation amplitude is not constant over time, but alternates between weak and strong oscillations (see [Mandelbrot, 1988] for a derivation of this phenomenon, where they are called "virtual α"). As can be confirmed from Fig. 5.1(a), this is indeed the case for the operating point $n_{corr} = 120\,\text{krpm}$, $\phi_{01} = 0.044$.

5.2 Validation

In order to validate that the Hurst exponent can indeed be used as a surge indicator, it is tested for its sensitivity with respect to several parameters. These are the sensor positioning, the sampling duration, and the sampling frequency. Benchmarking is done against two other signal properties that give information about the fluctuations in the pressure signal: the normalized fluctuation RMS, see above, and the signal power in the surge range, see Eq. (2.58). The tests presented in the following are based on the data for the truck-sized compressor. Analyses regarding the best sensor position for the light duty turbocharger compressor are found in paper I.

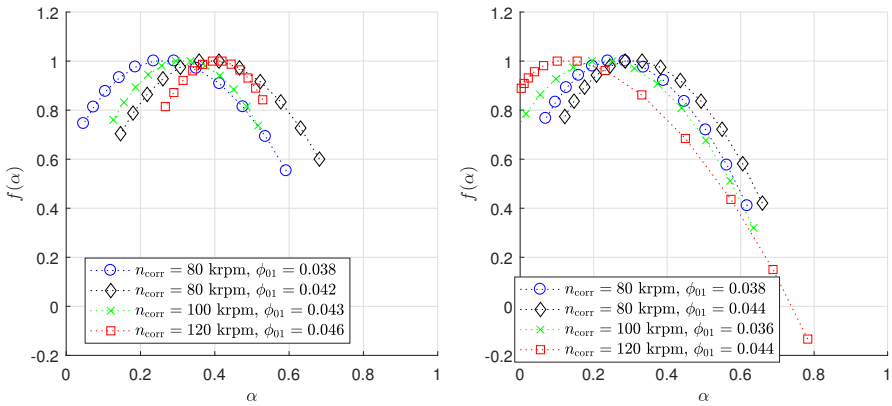

(a) Acoustic test rig (b) Cold gas stand

Figure 5.4: Singularity spectra of selected operating points on the acoustic test rig and the cold gas stand.

5.2.1 Benchmarking and sensor positioning

Pressure fluctuation RMS, signal power P, and Hurst exponents for different sensor positions within the truck-sized compressor at two speedlines are shown in Fig. 5.5. The pressure sensor locations are denoted "D" if they are in the diffuser backplate, and "V" if they are in the volute, radially inwards. The number indicates the circumferential position, where position "0" refers to the volute tongue, and positive numbers increase with the impeller rotational direction. Detailed information about the test setup can be found un the PhD theses by [Guillou, 2011] and [Gancedo, 2014].

The general trends were described in the previous section 5.1.1. Here, the focus will be on differences between the sensor locations. For a good surge indication, desired characteristics of a good position include clearly distinguishable ranges for the indicator value between stable operation and surge, as well as a gradual change when changing from stable to unstable operation. An evaluation of the RMS shows that the pressure at the outlet is suited best, giving a relatively low values in stable operation and increasing the most as operation moves towards the surge line. Pressure sensors in the volute are also well suited; the ones in the diffuser backplate, on the other hand, have higher RMS values even in stable operation. A possible explanation could be their proximity to the impeller outlet blades, where the jet-wake structure from the passing blades creates high-frequency fluctuations. However, for all sensor positions, the RMS values between stable operation and at the surge line do not differ by much.

The Hurst exponent is generally better suited as a surge indicator for this speedline, as described above. It is characterized by a relatively linear decline towards surge,

and a well-defined lower bound $H^{(2)} = 0$. With respect to the sensor position, sensors that are located at the outlet or closely upstream (negative or high positive position number) seem better suited. Not recommendable for this analysis are sensor locations V1 and D1, which are located under the volute tongue. This could be due to the fact that backwards traveling waves from the throttle downstream have to travel almost one circumference in the compressor until they reach these positions, giving more opportunity for a damping of their amplitudes.
A similar analysis is performed for a high speedline, $n_{\mathrm{corr}} = 88\,\mathrm{krpm}$. The relative fluctuation RMS, Fig. 5.5(b), are at a value of around $p_{\mathrm{rel,rms}} \approx 2\%$ for most of the stable operation for all pressure sensors within the compressor itself. Interestingly, the sensors D-2 and V4 show very high oscillations near the highest measured mass flows at $p_{\mathrm{rel,rms}} \approx 3\%$. Only the outlet pressure sensor has significantly lower fluctuations of around 1%. These increase at the last two operating points before the surge line.
The corresponding Hurst exponents, Fig. 5.5(f), show a two-step behavior towards surge. The first step occurs at peak $\mathrm{PR_{tt}}$, where a drop by about 0.2 can be observed for all sensors. The second step is located at $\phi_{01} = 0.055$, where the Hurst exponents for all sensors almost collapse; the drop is very steep, with a change in Hurst exponent by $\Delta H^{(2)} \approx 0.3$ over a change in mass flow of $\Delta\phi_{01} = 0.002$. As for the lower speedline, cp. Fig. 5.5(e), sensor locations V1 and D1 have lower $H^{(2)}$ during stable operation and are thus suited less well for the detection of instabilities with this criterion.

The signal power P is calculated within the frequency interval $f = [20, 40]\,\mathrm{Hz}$ in order to obtain a better measurement of the oscillations with the system natural frequency, which is around $f_{\mathrm{sys}} = 30\,\mathrm{Hz}$. Results are shown in Figs. 5.5(c) for the lower speedline $n_{\mathrm{corr}} = 64\,\mathrm{krpm}$ and 5.5(d) for the higher speedline $n_{\mathrm{corr}} = 88\,\mathrm{krpm}$. A reference pressure of 1 Pa was used for the conversion to decibel.
Considering the lower speedline, the signal power increases exponentially towards surge for all sensors, although the decibel itself is already a logarithmic unit. In contrast to the fluctuation RMS over all frequencies, the highest values can be found at the compressor outlet pressure. This is not unexpected, since it is a measure of the pressure oscillations with the system natural frequency in the compressible plenum. The RMS, on the other hand, is a measure of all oscillations and thus strongly affected by the unsteadiness of the flow in the compressor stage.
At the higher speedline, Fig. 5.5(d), the signal power increases from the highest mass flow until peak $\mathrm{PR_{tt}}$. It then mirrors the Hurst exponents, with an approximately constant value until the sharp increase closely before the surge line. The values are consistently higher than at the lower speed, which is mainly a result of not normalizing them. If one subtracts the difference between the kinetic energy of the two impeller speeds,

$$\Delta P_{\mathrm{imp}} = 20 \cdot \log_{10}\left(\frac{88}{64}\right)^2\,[\mathrm{dB}] \approx 5.5\,\mathrm{dB}\ , \tag{5.6}$$

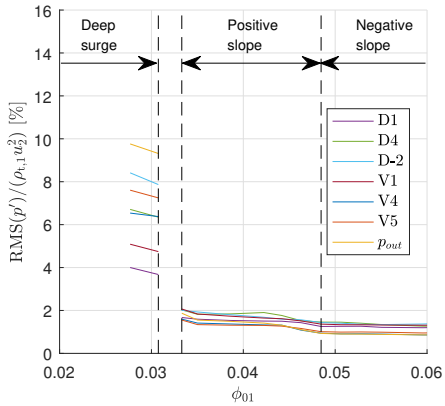

(a) RMS, $n_{\text{corr}} = 64\,\text{krpm}$

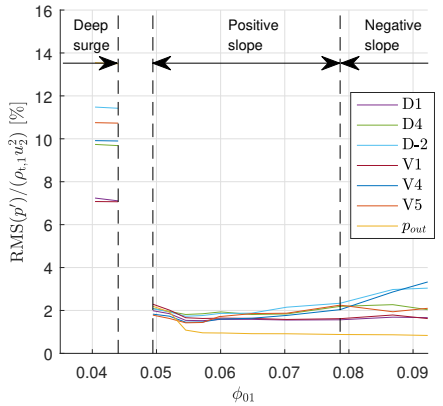

(b) RMS, $n_{\text{corr}} = 88\,\text{krpm}$

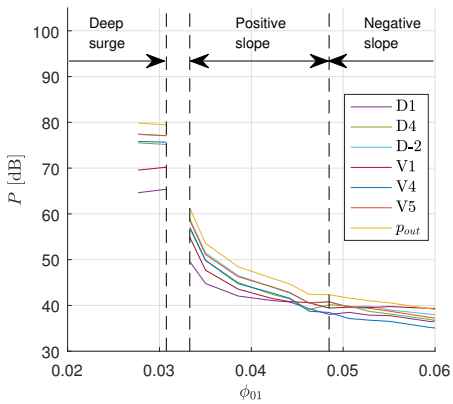

(c) P, $n_{\text{corr}} = 64\,\text{krpm}$

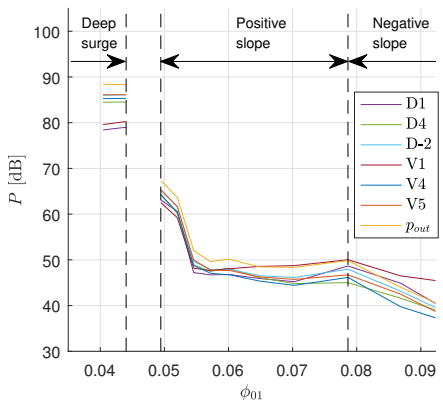

(d) P, $n_{\text{corr}} = 88\,\text{krpm}$

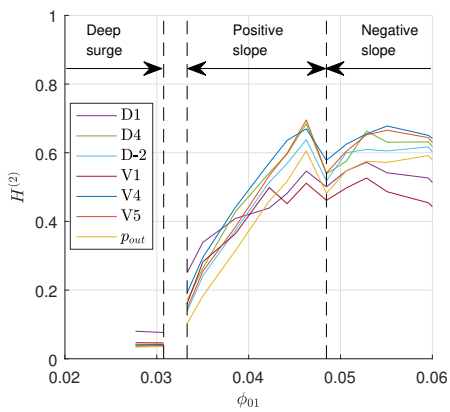

(e) $H^{(2)}$, $n_{\text{corr}} = 64\,\text{krpm}$

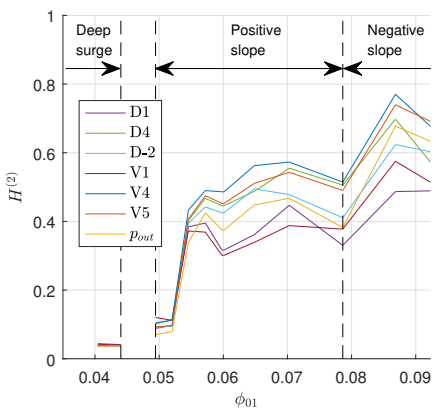

(f) $H^{(2)}$, $n_{\text{corr}} = 88\,\text{krpm}$

Figure 5.5: Stability analysis for the truck sized turbocharger using different criteria.

the signal power values are also within the same range for both speedlines. Both the signal power and the Hurst exponent indicate that at the lower speed, this compressor approaches unstable operation more gradual, while at high speeds, there is a sudden change in operating regime. The investigation suggests that the Hurst exponent and the signal power can be considered equivalent as surge indicators; as mentioned, the defined lower limit of 0 is an additional advantage of the Hurst exponent, while the faster computation and the widespread use of power spectra are arguments in favor of the signal power.

5.2.2 Sampling frequency

A sensitivity analysis is performed on the large compressor with respect to the required sampling frequency. The original sampling frequency was $f_s = 32768\,\mathrm{Hz}$. From this frequency, the signal is digitally downsampled by factors of $\{1/32, 1/64, 1/128\}$ Hz, resulting in new sampling frequencies $f_s = \{1024, 512, 256\}$. A lowpass filter is applied in order to avoid aliasing effects in the downsampled signal. Results are shown in Fig. 5.6 for the speedline $n_{\mathrm{corr}} = 64\,\mathrm{krpm}$, using the compressor outlet pressure which has previously been identified as a good sensor location. In this plot, all mass flow parameters from the choke line to deep surge are shown. The dashed vertical lines distinguish between different speedline slopes, as before.
One can observe that the lines for sampling frequencies 32768 Hz and 1024 Hz almost collapse into a single line, meaning that a sampling frequency of 1024 Hz is sufficient provided a lowpass filter is applied when sampling. A sampling frequency of 512 Hz results in slightly lower Hurst exponents at high mass flows. The difference to the higher sampling frequencies is, however, small, and the values are still in the range that indicates stability. A different picture emerges for $f_s = 256\,\mathrm{Hz}$. The values are significantly lower during stable operation. This is caused by the filter: since the oscillations at higher frequencies are removed, there are not enough fluctuations left in the signal to find the long-term correlations. If this filter is removed, the values of $H^{(2)}$ increase in the stable range. Unfortunately, they also increase close to surge, and the signal sampled with this frequency has clearly worse properties for surge indication via the Hurst exponent.

5.3 Application

5.3.1 Analyzing a compressor map

The system analysis is now extended to whole compressor maps for both the light duty and the heavy duty compressors. Figure 5.7 shows both maps as measured on the respective cold gas stand. For the light duty compressor, Fig. 5.7(a), only the left half of the map is shown. For the heavy duty compressor, the highest speedline also does not extend until compressor choke. In this map, there are also two points in deep surge shown, which can easily be distinguished by the sharp pressure drop at the surge line. The mass flow and TPR are of course time-averages, with the real

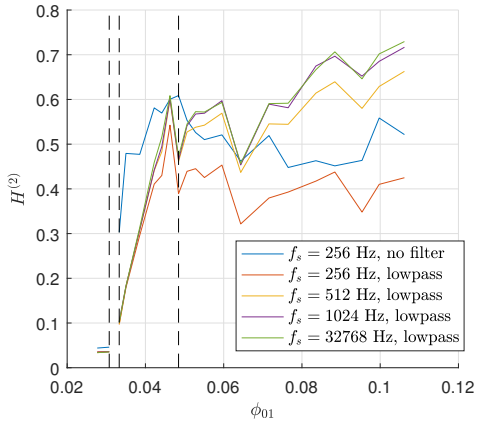

Figure 5.6: Hurst exponent using the compressor outlet pressure for different sampling frequencies along the speedline $n_{\mathrm{corr}} = 64\,\mathrm{krpm}$

operation following a limit cycle around these points in the compressor map. The Hurst exponents of the outlet pressure are imposed as a contour. The marker of each measurement point indicates the shape of the Renyi scaling exponent $\tau(q)$. Both compressor maps show similar Hurst exponents of ca. $H^{(2)} = 0.2$ close to the surge line. At the highest mass flows shown and high speeds, the Hurst exponents are in the range $H^{(2)} = 0.8...1$ for both maps, while they are a bit lower at high mass flows and low speeds. In the light duty compressor map, the slope of the higher speedlines is close to zero or positive for large parts of the shown operating range. The compressor operates close to its theoretical stability limit. Consequently, the Hurst exponents in this operating range are also low.

The heavy duty compressor is equipped with ports in the shroud, a passive flow device to extend its range by allowing the reverse flow to bypass the inducer and mixing upstream with the incoming flow. The compression system operates more stable close to the surge line. The decrease of $H^{(2)}$ towards zero close to the surge line occurs more abrupt, especially at higher speeds as could also be seen from Figs. 5.5(e) and 5.5(f).

The switch from a not concave $\tau(q)$ shape to a concave $\tau(q)$ shape can be used as an additional binary indicator about system stability. At high mass flows, the function is not concave, meaning that the data is monofractal or that the higher order Hurst exponents are larger than the lower order ones. The switch appears approximately at peak TPR for high speedlines, which is consistent with the theoretical stability estimates for both compressors. At low mass flows, the switch appears where the speedline slope is still negative, and the system is thus theoretically stable. This indicator could therefore have potential as precursor at low compressor speeds.

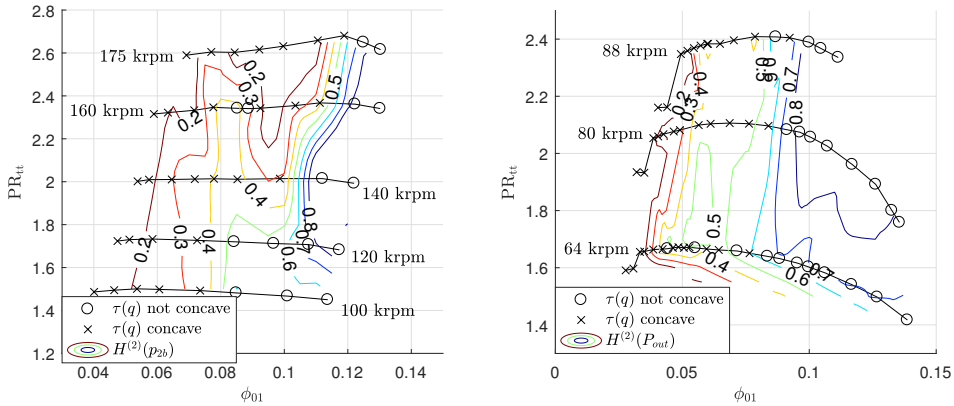

(a) Light duty compressor

(b) Heavy duty compressor

Figure 5.7: Compressor maps of the light duty compressor and the heavy duty compressor with Hurst exponents as contour markers indicating the shape of the $\tau(q)$ function.

5.3.2 Bend positioning at the compressor inlet

Maps for turbocharger compressors are commonly measured and provided by the turbocharger supplier on a hot gas stand. The standard for these measurements is [SAE, 1995a], which prescribes long straight inlet pipes to achieve fully developed flow. On the engine, however, packaging limitations prescribe bended inlets. Several authors [Galindo et al., 2011, Serrano et al., 2013, Marelli et al., 2016] have found that these bends shift the surge line towards lower mass flows, resulting in a wider operating range. For the light duty compressor used in this thesis, studies concerning the effect of an inlet bend are presented in papers I and V and will be shortly summarized in the remainder of this section. The studies concern the installation of a 90° bend with a ratio of the centerline curvature radius to the inner radius of $2r_c/D = 1.04$. The B parameter was kept approximately constant for both systems. Figure 5.8(a) gives an overview over the positioning of the bend. The bend was installed $2D$ upstream the impeller nut. Since the flow in the compressor stage is not axisymmetric at lower mass flows – the volute acts as a diffuser – the relative orientation of the bend to the compressor axis was also changed.
The resulting compressor maps for the straight inlet and the bend inlet in position 9 o'clock are shown in Fig. 5.8(b). The rightmost point shown corresponds to the highest efficiency for that speedline. The last stable point displayed for each surge line is on the deep surge line. There is an uncertainty associated with these points due to the accuracy of the compressor outlet valve actuator; its sensor shows fluctuations of ca. ±0.3% of the full valve range. The smallest step chosen when throttling the compressor towards surge was therefore 0.5% of the full range, which corresponds

to a mass flow parameter uncertainty of approximately $\varepsilon(\phi_{SL}) = 0.003...0.004$ at the surge line.
Comparing the straight inlet with the bend inlet speedlines, the differences at low impeller speeds are very small. They can mainly be found at the surge line, where the bend inlet gives a consistently small improvement in surge margin, although the uncertainty described above needs to be kept in mind here. At higher speeds, the largest differences are at the high mass flows. The bend inlet results in significantly lower PR_{tt} here. This difference can be almost entirely explained by the pressure losses in the bend, which are not compensated for, see [Kerres et al., 2016a]. At the highest speedline of $n_{corr} = 175\,krpm$, the deep surge margin is much improved with a bend inlet.
Over parts of the maps shown in Fig. 5.8(b), the compression systems are operating

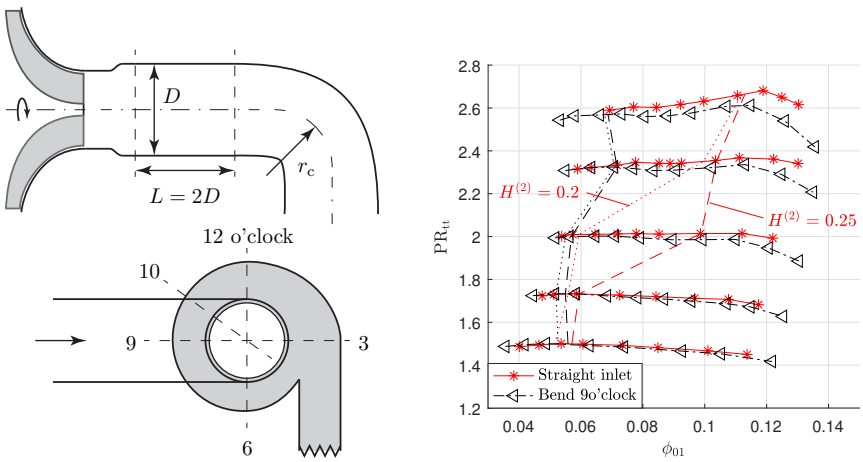

(a) Bend positioning (b) Compressor maps

Figure 5.8: Comparison of resulting surge lines for a straight pipe and a bend at the compressor inlet using a Hurst exponent surge criterion.

in mild surge. The Hurst exponent criterion is used to distinguish between stability and instability. For each map, two iso-lines of constant $H^{(2)} = \{0.2, 0.25\}$ are drawn. If a given value of $H^{(2)}$ is found several times on the same speedline, see e.g. Fig. 5.7(a) for the straight inlet map, the highest mass flow parameter is used. The criterion shown that in fact, the bend inlet compression system is more stable over wide ranges at high impeller speeds. The straight inlet compression system reaches peak PR_{tt} at mass flow parameters $\phi_{01} \geq 0.11$, with a positive speedline slope at lower mass flows. Noteworthy is also that the bend inlet system does not display these instabilities, even at the highest speed and peak PR_{tt} where its speedline slope is also positive. This could be due to the change in throttle slope for the combined bend and throttle, which gives a larger range of dynamic stability, cp. Eq. (2.44),

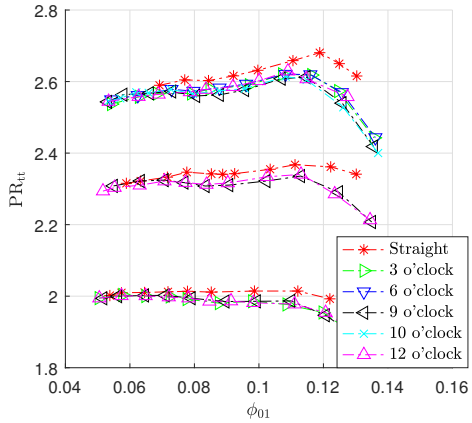

Figure 5.9: Higher speedlines of the compressor map for the straight inlet and bend inlet in different clocking positions.

given the similar B values.

The results of the additional investigation regarding the relative bend positioning at the inlet of the light duty compressor are shown in Fig. 5.9. The highest speedline, $n_{\text{corr}} = 175\,\text{krpm}$, was measured first, since the largest differences between different inlet configurations were found for this configuration. The total pressure ratios are slightly lower for the inlet position 9 o'clock; the maximum difference, however, is only $\Delta\text{PR}_{\text{tt}} = 0.02$, which is a relative difference of 0.77%. It is found between the positions 12 and 9 o'clock. This difference is outside the uncertainty range – the type 1 uncertainty is $s_{\text{PR}} \approx 0.15\%$ – but small nevertheless. A small difference is also observed at $n_{\text{corr}} = 160\,\text{krpm}$, where the 9 o'clock position again shows a slightly more pronounced camel-back shape. At $n_{\text{corr}} = 140\,\text{krpm}$, all differences in PR are within the margin of error. With respect to the surge margin, no discernible difference could be found due to the uncertainty in outlet valve opening.

5.3.3 On-engine application

As described in Chapter 1, the compressor surge line limits engine BMEP at low speeds. Due to the uncertainty associated with the exact location of the surge line, a safety margin is usually accounted for in the engine calibration. This margin can be exceeded, however, if a sudden engine load drop occurs. The fast reduction of the engine air inflow flow, e.g. through throttle valve closing on a SI engine, moves the compressor operating point into the surge region. A bypass of the compressor that recirculates air can keep the mass flow through the compressor at higher levels. However, a criterion is needed when to open the bypass valve. If this criterion is hard-coded as a static calibration, it needs to be more conservative compared to a

real-time detector on the engine.

It was tested whether it is possible to use the DFA method to detect surge on an engine by analyzing the compressor housing vibrations. This method was selected because a normal production knock sensor can be used for detection. The knock sensor is a reasonable cheap accelerometer; its additional cost of a few Euros could be motivated from a cost-benefit perspective for a production series engine. The drawback, of course, is that it does not measure oscillations of the flow, but rather all possible kinds of housing vibrations.
Figure 5.10 gives an example of different frequency oscillations present in a knock sensor signal. Shown are the spectrograms of the knock sensor voltage for two engine transient load reductions from full load to zero load. The engine speed is constant at $n_{\mathrm{eng}} = 1300\,\mathrm{rpm}$. The load reduction starts at $t = 0.5\,\mathrm{s}$. In the left plot, Fig. 5.10(a), the load reduction occurs over a time of 3 seconds. The compressor does not enter surge. In the right plot, Fig. 5.10(b), the load reduction occurs over 0.2 seconds and the compressor enters surge. Only frequencies from 0 to 100 Hz are shown, although higher frequency oscillations are of course also present in the signal.

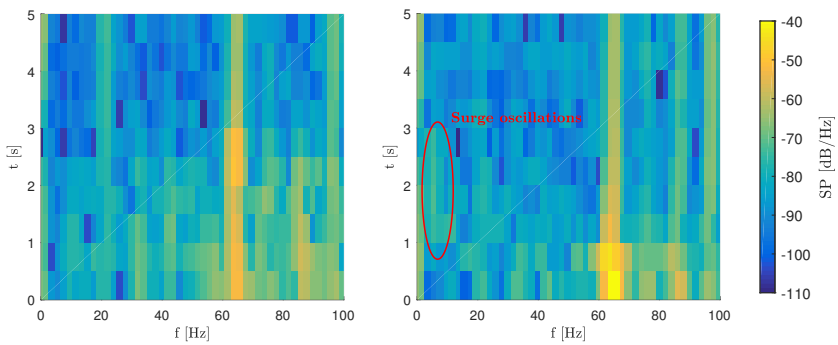

(a) Slow load reduction, no surge (b) Fast load reduction, surge

Figure 5.10: Spectrograms of the knock sensor signal mounted on a compressor housing for a fast and a slow load reduction at constant engine speed of $n_{\mathrm{eng}} = 1300\,\mathrm{rpm}$.

In both cases, the frequency band containing the highest power is clearly the engine firing frequency, which is

$$f_{\mathrm{eng,f}} = \frac{n_{\mathrm{eng}} z_{\mathrm{cyl}}}{2} = 65\,\mathrm{Hz}\ . \tag{5.7}$$

While engine load is high, most other frequency bands shown also contain a relatively large amount of signal power. After the load drop, surge occurs for approximately 2

seconds in case of the fast transient; this was evaluated by visually observing the intake filter and air system for large vibrations, and by measuring the inlet temperature increase [Hamberg et al., 2017]. What are very likely the surge oscillations – in the range of 6 Hz – is marked in Fig. 5.10(b). These would be hard to find, however, without prior knowledge where to look in the spectrogram.

In paper IV, it is investigated how different methods perform in detecting surge from these knock accelerometer signals. The methods selected are the RMS, the signal power, the Hurst exponent, and a related fluctuations scaling exponent better suited to detect changes in the scaling behavior from [Staudacher et al., 2004]. In this section, however, it shall suffice to show why the Hurst exponent is very difficult to use as a surge indicator on the engine.
One drawback of the Hurst exponent is that sampling duration is relatively long: [Kantelhardt, 2011] recommends a signal length at least for times of the largest segment size in DFA. Calculating the Hurst exponent as fit of the fluctuation function from one to eight surge periods as done here results then in 32 surge periods for an accurate estimate of the Hurst exponent, which is very long compared to what the Fourier transform and related algorithms require. This signal length can be reduced by estimating the Hurst exponent over a smaller range of scales; the cost is then a loss of accuracy in the estimate.
For a time-resolved estimate of the Hurst exponent, the signal can be split into parts and, and DFA is performed on each part. This is e.g. done in papers I and IV, and works in principle. On the engine, a different problem is much more significant: Even during stable compressor operation, the signal consists of periodic repetitions of engine-related cycles. On the compressor housing, vibrations induced by cylinder firing are much stronger than surge oscillations as could be seen from Fig. 5.10. Thus, the fluctuation function is mainly dominated by these oscillations. This is shown in Fig. 5.11. Plotted are the fluctuation function for different segments of the knock sensor signals. Both time series are split into parts of 1 second length with 75% overlap, and DFA is performed on each part. Fluctuation functions plotted in red are for engine operation at steady-state with $n_{\mathrm{eng}} = 1000\,\mathrm{rpm}$ and 50% load. Those plotted in blue are for a fast engine transient at $n_{\mathrm{eng}} = 1300\,\mathrm{rpm}$, where surge is provoked for around 2 seconds out of 5 seconds total signal length. The detrending order used was $m = 2$, so that quadratic trends in the integrated time series and therefore linear trends in the underlying time series are removed.
For the steady-state engine case, a cross-over is seen at

$$\log_2(t_s) \approx -5 \quad \Rightarrow \quad t_s \approx \frac{1}{32}\mathrm{s}\,. \tag{5.8}$$

The firing frequency, however, is $f_{\mathrm{eng,f}} = 50\,\mathrm{Hz}$ at 1000 rpm. The reason this crossover is shifted is due to the higher detrending order m, see [Kantelhardt, 2011]. For all time scales larger than the crossover, the Hurst exponent is approximately zero.
For the fast transient engine case, the general shape of the fluctuation function

is similar. The differences between the parts of the signal (i.e. blue lines) are larger, since some lines represent full load, and some zero load. The Hurst exponent of approximately zero can also be found for all of these lines, however. For a surge detection algorithm as used above on the gas stand, one would need a clear distinction in slope for large time scales as indicated by the dashed line. What is observed, on the other hand, is only a very small difference showcased in the black circle.

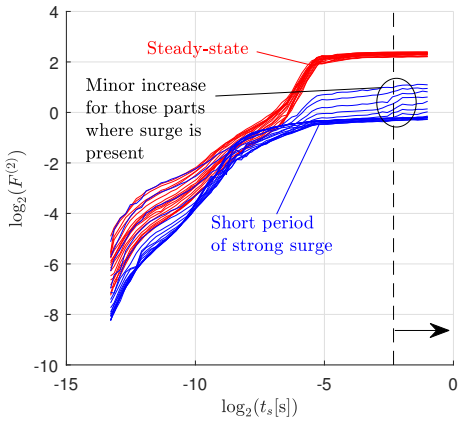

Figure 5.11: Fluctuation functions of the compressor housing vibrations for a steady-state and a transient load engine operating point. The engine operation point is symbolized by the color. Different lines in the same color represent fluctuation functions calculated over small parts of the signal.

Some of these problems with the Hurst exponent can be solved by choosing a related method, Progressive DFA (PDFA), see [Staudacher et al., 2004]. This method was derived from DFA in order to detect changes in the scaling law, originally to distinguish between different phases of sleep by means of heart-rate monitoring. Even that method, however, cannot avoid the underlying problem of using compressor housing accelerations for surge detection: Especially during transient engine operation, changes in housing vibrations are dominated by other factors than surge. In paper IV, it is found that one can design a relatively accurate surge detection mechanism based on PDFA and the knock sensor; but this mechanism is not based on a physical connection to surge, but rather on the change in scaling law due to the engine load drop.

5.4 Summary of the advantages and drawbacks

The investigations into the Hurst exponent as a surge indicator have revealed some advantages and some drawbacks compared to other surge indicators, which are summarized here. Probably the most important strength is the lower limit of $H^{(2)} = 0$

for exactly repeating oscillations, which is a mathematical property. Very low Hurst exponents of the order $H^{(2)} \leq 0.05$ could be confirmed for surge operation for a light duty and a heavy duty turbocharger compressor, operated on cold gas stands. The extension of this method to higher order Hurst exponents $H^{(q)}$ showed potential as early surge precursor, giving a warning already on the negatively sloped part of the compressor characteristic speedline. The singularity spectra of the pressure signals were shown to be very similar for compressor operation in very different test rigs with correspondingly very different surge behavior. A further possible advantage of DFA, not investigated here, is the possibility to remove polynomial trends from the signal by using higher order DFA.

The previous paragraph mentioned several parameters that allow one to investigate different properties of the signal, and customize the calculation of the Hurst exponent: Besides the aforementioned DFA order m and Hurst exponent order q, the time scales over which it is calculated should also be mentioned here. These possibilities, however, also contain the danger that one overfits the surge detection algorithm based on the Hurst exponent. This can result in very good properties for the system investigated, but lacking generality. A disadvantage of the Hurst exponent compared to the signal power P used here (and other indicators that can be based on the Fast Fourier Transform algorithm) is the longer calculation time. This drawback could alleviated for real-time calculation, since the results from older segments $\sigma_\nu^{\mathrm{DFA}}$ in DFA can be reused.
A major problem for a Hurst exponent based surge indicator is if other, stronger harmonic oscillations with a frequency in the same order of magnitude are present. These are easy to ignore if one uses indicators based on the Fourier transform. The fluctuation function requires a larger bandwidth between oscillations of different frequencies in order to be able to distinguish between them. This was found to inhibit the application of the Hurst exponent as surge indicator for on-engine surge detection. Filtering away the disturbances is not straightforward, since a certain randomness is required to obtain $H^{(2)} \geq 0.5$ in stable operation.

6 Conclusions and future work

The aim of this thesis was to investigate the destabilization of turbocharger compressors at low mass flows. Research questions were grouped into four areas. The following paragraphs will summarize the results for each area and give possible directions for future work.

The first group deals with the introduction of a new stability indicator for compression systems, based on the Hurst exponent of the pressure signal. They should establish its general usability for gas stand measurements. For three experimental setups on a gas stand, it was found that the Hurst exponent calculated over time scales from one to several system characteristic time scales can be used as surge indicator. Values of $H^{(2)} \geq 0.5$ indicate stability on all compression systems, while the value decreases as the system becomes less stable. At the edge to deep surge, values in the range $H^{(2)} = 0.1...0.2$ were found; in deep surge, they are around $H^{(2)} \approx 0.05$. As was shown on the acoustic test rig, however, if there is a system instability with a significantly different characteristic frequency, it will not be detected by this algorithm. An extension of the algorithm to higher order Hurst exponents revealed additional possibilities as a surge precursor by considering only large amplitude fluctuations. Especially interesting is that this indicated the onset of instabilities where the compression system was still classified as theoretically stable using linear stability analysis, since the compressor characteristic slope was negative.
The Hurst exponent was compared to two other stability indicators based on the pressure signal, namely the normalized fluctuation RMS and the signal power in the system eigenfrequency range. For all three setups, the Hurst exponent was found to be superior to the RMS as a surge indicator; advantages are its approximately system-independent values for stable operation and near surge, and the steady decline at least at low compressor speeds. Benchmarked against the signal power, both concepts show advantages and disadvantages, and the preferred indicator is case-dependent.
This idea has been tested on three compression systems, two for the light duty turbocharger and one for the heavy duty turbocharger. The two gas stands, however, are similar in their layout with outlet piping without a dedicated compressible volume leading to the throttle. Their B values at medium speed are in the range of $B = 0.5...0.6$. It is generally accepted that large B systems show a different surge

behavior, where deep surge looks less like a strong version of mild surge, but is instead characterized by a distinct blow-down phase. In addition, this algorithm could be applied to the impeller speed signal instead of the pressure, which is sometimes used as surge indicator.
The extension to higher order Hurst exponents can be helpful for a better understanding of surge onset. It would be interesting to connect it to other methods from chaos theory, e.g. by investigating the presence of attractors in the pressure time series.

The second research question category is about the applicability of the Hurst exponent as surge indicator on an engine. For this investigation, compressor housing acceleration instead of pressure fluctuations were used. This was found to be problematic since many other factors influence housing vibrations, especially the cylinder firing events. However, even if one uses compressor outlet pressure, it is expected that the Hurst exponent will be close to zero during to stable operation. The pressure pulses generated by the intake valves dominate the correlations present in the signal. Since they are also periodically repeating and with a frequency close to the surge frequency, the Hurst exponent can be expected to be around zero independent of compressor stability. A way out could the PDFA: The occurrence of surge leads to a change in scaling behavior of the fluctuation function, which this method detects faster and more reliable than the normal DFA. An alternative is the wavelet transform, a popular method to detect oscillations in non-stationary time series.

The third group of research questions is concerned with the installation of a bended inlet pipe at the compressor, and its influence on the performance and operating range. Both the Hurst exponent and the signal power were used to investigate these questions. Results show that a bend at the inlet improves the surge margin of the compressor, mainly at high impeller speeds, compared to a straight inlet pipe. A degradation in total pressure ratio can be attributed to the bend losses. These losses also stabilize the compression system, as predicted by the lumped parameter model and experimentally confirmed for a straight pipe with a lossy diffuser in [Kerres et al., 2016a]. The orientation of the bend towards the compressor does not have a major influence on pressure ratio or operational range.
Given that both theory and experiments suggest that a pressure loss is mainly responsible for the increase in operating width, an obvious follow-up would to try to connect these results by modeling the inlet system using transfer matrices for the bend and the straight pipes. Recent attempts at modeling inlet conditions via this model have been made by e.g. by [Brun et al., 2014] and [Schäfer et al., 2016]. Other work could focus on the asymmetric flow field after the bend: In the experiments described in this thesis, the bend located was two diameters upstream the impeller. Moving it close could reduce the homogenization of the flow before it enters the impeller, and thus accentuate any effects on the compressor map which could be be proven here.

The fourth group of research questions is related to the accuracy of lower order models for compressor performance prediction. For the light duty turbocharger compressors investigated, it is found that RANS performs significantly better than 1D models at off-design conditions, especially at lower speeds and lower mass flows. Good predictions are achieved on the design line. At higher mass flows, both the RANS and the 1D model prediction are saddled with large errors. The component model that produces the largest deviations between 1D model and RANS is the vaneless diffuser at low mass flows and the volute at high mass flows.
These results have to be interpreted carefully, however, since they rest on the assumption that the CFD flow field prediction is correct if its pressure ratio prediction is correct. For future work, the component losses should be measured directly by temperature and pressure measurements at the respective stations. Since one component is dependent on the inlet conditions imposed from the outlet of the previous component, a sensitivity analysis could reveal whether these models perform inherently worse at off-design, or if prediction errors are propagated and amplified through the system. The attempt to further distinguish between different impeller losses in the CFD by a control volume approach in [Kerres et al., 2017c, Sundström et al., 2017] gave some surprisingly good agreements, although based on very strong assumptions; it could be worthwhile to investigate this approach further, maybe using more accurate CFD results like those from LES.

7 Appended papers and authors' contributions

Paper I

Bertrand Kerres (BK), Vineeth Nair (VN), Andreas Cronhjort (AC), Mihai Mihaescu (MM). Analysis of the Turbocharger Compressor Surge Margin Using a Hurst-Exponent-based Criterion.*SAE Int. J. Engines 9 (3).*

The Hurst exponent is introduced as a surge indicator for a light duty turbocharger compressor. Focus is on the introduction of DFA as methodology to the reader, and a general validation of the method.
BK set up and ran the experiments, and performed the analysis after an idea by VN. BK wrote the paper under supervision by AC and MM. BK presented the paper at the SAE 2016 World Congress, 12-14 April, 2016, Detroit, MI, USA.

Paper II

Bertrand Kerres (BK), Mihai Mihaescu (MM), Matthieu Gancedo (MG), Ephraim Gutmark (EG). Optimal Pressure Based Detection of Compressor Instabilities Using the Hurst Exponent. *SAE Int. J. Engines 10 (4).*

In order to increase confidence in the method introduced in paper I, it is repeated for a second compression system. Some sensitivity studies with respect to sensor positioning, sampling frequency and sampling duration are presented.
MG and EG run the experiments and provided the data. BK did the analysis and wrote the paper under supervision by MM. BK presented the paper at the SAE 2017 World Congress Experience, 4-6 April, 2017, Detroit, MI, USA.

Paper III

Bertrand Kerres (BK), Raimo Kabral (RK), Vineeth Nair (VN), Mats Åbom (MÅ). The Hurst Exponent as a model-free precursor to centrifugal compressor surge. *to be submitted to ASME J Turbomach.*

The focus of this paper in mainly on the methodology and theoretical aspects. The use of the singularity spectra is introduced for compressor surge, and a comparison with theoretical stability estimates is performed.
BK and RK ran the respective experiments. BK performed the analysis and wrote most parts of the paper, with the description of the acoustic test rig contributed by RK and the method section contributed by VN. Supervision by MÅ.

Paper IV

Bertrand Kerres (BK), Andreas Cronhjort (AC), Mihai Mihaescu (MM). A Comparison of On-Engine Surge Detection Algorithms Using Knock Accelerometers. *submitted to the SAE 2017 International Powertrain, Fuels and Lubricants Meeting.*

It is attempted to use the methodology developed in papers I to III on compressor housing vibrations on an engine. The paper shows that the application of the method on-engine is very challenging.
The experimental data was gathered by MSc students as part of their project course, under supervision by AC and Ola Stenlåås. BK analyzed the data and wrote the paper under supervision by AC and MM.

Paper V

Bertrand Kerres (BK), Andreas Cronhjort (AC), Mihai Mihaescu (MM). Experimental investigation of upstream installation effects on the turbocharger compressor map. *Proceedings of the 12th International Conference on Turbochargers and Turbocharging, London, UK, 17-18 May, 2016.*

The effects of a bend at the compressor inlet on compressor performance and the surge line are investigated. Furthermore, an assessment of the impact of bend clocking positions is made.
BK ran the experiments, performed the analysis and wrote and presented the paper. Supervision by AC and MM.

Paper VI

Bertrand Kerres (BK), Sergio Sanz (SS), Elias Sundström (ES), Mihai Mihaescu (MM). A Comparison of Performance Predictions Between 1D Models and Numerical Data for a Turbocharger Compressor. *Proceedings of the 12th European Conference on Turbomachinery Fluid dynamics and Thermodynamics, Stockholm, Sweden, 3-7 April, 2017.*

The accuracy of 1D model and RANS computations pressure ratio predictions is compared for the map of a small light duty turbocharger compressor. A method is presented to distinguish between different impeller losses in CFD data using a

control volume approach.
BK started the implementation of the 1D model, which was finished by SS under supervision by BK. SS implemented the data comparison codes under supervision by BK. ES provided the RANS CFD data. BK wrote the paper under supervision by MM and with input from ES and SS. ES presented the paper at the conference.

Paper VII

Elias Sundström (ES), Bertrand Kerres (BK), Mihai Mihaescu (MM). Evaluation of Centrifugal Compressor Performance Models Using Large Eddy Simulation Data. *Proceedings of the ASME 2016 Turbo Expo Turbomachinery Technical Conference and Exposition, Seoul, South Korea, 13-17 June, 2016.*

It is investigated how losses should be accounted for in a compressor with a ported shroud using LES simulations and a 1D model.
ES ran the Large Eddy Simulation and implemented the 1D model. The method of comparison was jointly developed by ES and BK. BK wrote parts of the results and discussion sections and provided the schematic drawings. ES wrote the other parts of the paper and presented the results at the conference. Supervision by MM.

Paper VIII

Elias Sundström (ES), Bertrand Kerres (BK), Sergio Sanz (SS), Mihai Mihaescu (MM). On the Assessment of Centrifugal Compressor Parameters by Theoretical and Computational Models. *Proceedings of the ASME 2017 Turbo Expo Turbomachinery Technical Conference and Exposition, Charlotte, NC, USA, 26-30 June, 2017.*

A follow-up to paper VI, tested on a larger light duty turbocharger compressor. It is found that some discrepancies between 1D model and RANS data disappear at a slightly larger, but geometrically similar compressor and are therefore likely related to model tuning parameters.
ES ran the RANS simulations. BK and SS implemented the 1D model code. BK ran the 1D model and created the results plots. The paper was written by ES under supervision by MM.

Abbreviations and symbols

Abbreviations

BMEP	Brake mean effective pressure
CFD	Computational fluid dynamics
DFA	Detrended fluctuation analysis
DFT	Discrete Fourier transform
EU	European Union
FMEP	Friction mean effective pressure
HP	High-pressure
IMEP	Indicated mean effective pressure
IRS	Impeller rotating stall
LP	Low-pressure
PMEP	Pump mean effecitive pressure
PS	Pressure side
RANS	Reynolds-Averaged Navier Stokes
RMS	Root mean square
SS	Suction side
TEIS	Two elements in series
VDRS	Vaneless diffuser rotating stall
VI	Virtual Instrument

Latin letters

C	Compressor transfer matrix
D	Duct transfer matrix
E	Identity matrix
P	Plenum transfer matrix
p	polynomial coefficients vector
T	Throttle transfer matrix
V	Vandermonde matrix
x	index vector
y	value vector
DF	Diffusion factor
Ma	Mach number
PR	Pressure ratio
Re	Reynolds number
SP	Stability parameter
SM	Surge margin
A	Area
a	Speed of sound
B	Greitzer B parameter
b	Diffuser width
C	Coefficient
c	Flow velocity in stationary system; heat capacity
D	Diameter
d	Dimension
F	Force; fluctuation function
f	Frequency [cycles/time]
H	Hurst exponent

h	Specific enthalpy
i	Imaginary unit
J	Moment of inertia
k	Coefficient
L	Length
l	Ruler length
m	Mass; detrending order
N	Discrete series length [samples]
n	Rotational speed [revolutions/time]
P	Signal power
p	Pressure
Q	Heat
q	Fluctuation order
R	Specific gas constant; range; autocorrelation
r	Radius
S	Entropy; Spectral density
s	Specific entropy; sample standard deviation
T	Temperature; Discrete time series length [samples]
t	Time; Discrete time index
u	Impeller blade speed [distance/time]
V	Volume
W	Work
w	Flow velocity in relative system; segment length
Y	Integrated time series
Z	Number of blades
z	Number of cylinders

Greek letters

α	Flow angle to tangent in absolute system; singularity strength
β	Flow angle to tangent in relative system; scaling exponent
δ	Boundary layer thickness
$\Delta\square$	Difference in $\square$
δ_1	Displacement thickness
δ_2	Momentum loss thickness
η	Isentropic efficiency
κ	Ratio of specific heat $c_\mathrm{p}/c_\mathrm{v}$
λ	Loss coefficient
ϕ	Mass flow parameter
ν	kinamatic viscosity
Ω	System rotation frequency [angle/time]
ω	Frequency [angle/time]
ψ	Work coefficient
ρ	Density
σ	Slip factor; population standard deviation
τ	Torque; Renyi scaling exponent
ζ	Damping coefficient

Subindices

∞	free-stream value
θ	tangential direction
1	compressor inlet; before
2	impeller outlet; after
3	diffuser inlet
4	diffuser exit

5	volute
bl	blade
C	Compressor; Coriolis
c	centerline
cc	crankcase
corr	corrected
cr	critical
cyl	cylinder
d	dissipation
eng	engine
exh	exhaust
gr	gross
H	Helmholtz
id	ideal
imp	impeller
in	inlet
inc	incidence
int	intake
jw	jet-wake
m	meridional direction
MF	mass flow
mf	mean friction
mi	mean indicated
mp	mean pump
net	net
OP	operating point
or	orifice

out	outlet
P	plenum
p	isobaric
PR	pressure ratio
r	radial direction
red	reduced
ref	reference
rms	root mean square
rt	return flow appearance
s	isentropic; sampling; segment; surge
sf	skin friction
SL	surge line
st	stall
sw	swirl; swept
sys	system
T	Throttle
t	total; tip
th	throat
v	isochoric
x	axial direction; signal

Superindices

(q)	Order q
T	Transpose
DFA	After detrending

Operators

$\angle$	Angle between

$\dot{\square}$	Total derivative in time, i.e. $\mathrm{d}\square/\mathrm{d}t$
$\langle\square\rangle$	Mean value of $\square$
$\square'$	Fluctuation around mean value of $\square$
$\square^*$	Design conditions
$\tilde{\square}$	mean-subtracted
$\vec{\square}$	Vector in Cartesian 3D space

Bibliography

[Abdelhamid, 1980] Abdelhamid, A. (1980). Analysis of rotating stall in vaneless diffusers of centrifugal compressors. In *ASME Paper 80-GT-184, Proceedings of the 1980 ASME Gas Turbine Conference and Products Show, New Orleans, March 10-13*.

[Abdelhamid, 1981] Abdelhamid, A. (1981). Effects of vaneless diffuser geometry on flow instability in centrifugal compression systems. In *ASME Paper 81-GT-10, Proceedings of the 1981 ASME Gas Turbine Conference and Products Show, Houston, March 9-12*.

[ACEA, 2017a] ACEA (2017a). European automobile manufactures association: Consolidated registrations - by country.

[ACEA, 2017b] ACEA (2017b). European automobile manufactures association press release: Alternative fuel vehicle registrations.

[Andersen et al., 2008] Andersen, J., Lindström, F., and Westin, F. (2008). Surge definitions for radial compressors in automotive turbochargers. *SAE International Journal of Engines*, 1:218–231.

[Aungier, 1995] Aungier, R. (1995). Mean streamline aerodynamic performance analysis of centrifugal compressors. *Journal of Turbomachinery*, 117(3):360–366.

[Aungier, 2000] Aungier, R. (2000). *Centrifugal Compressors: A Strategy for Aerodynamic Design and Analysis*. ASME Press, New York.

[ben Avraham and Havlin, 2009] ben Avraham, D. and Havlin, S. (2009). *Encyclopedia of Complexity and Systems Science*, chapter Introduction to Fractals and Multifractals, pages 3846–3847. Springer, Berlin, Heidelberg, New York.

[Bergmann and Parma, 2016] Bergmann, M. and Parma, P. (2016). The e-drive: An isentropic compressor performance test rig. In *Proceedings of the 12th International Conference on Turbochargers and Turbocharging, May 17-18, 2016, London, UK*.

[BIL Sweden, 2017] BIL Sweden (2017). Pressmeddelande: Definitiva nyregistreringar under 2016.

[Bozza and De Bellis, 2010] Bozza, F. and De Bellis, V. (2010). Steady and unsteady modeling of turbocharger compressors for automotive engines. SAE Technical Paper 2010-01-1536, University of Naples.

[Brennen, 1994] Brennen, C. (1994). *Hydrodynamics of Pumps*. Concepts ETI, Inc. and Oxford University Press.

[Bright et al., 1995] Bright, M., Qammar, H., and Hartley, T. (1995). Attractor dimension analysis of a single stage high speed compressor. In *Proceedings of SPIE - The International Society for Optical Engineering, Vol 2494*, volume 2494, pages 14–20.

[Bright et al., 1999] Bright, M., Qammar, H., and Wang, L. (1999). Investigation of pre-stall mode and pip inception in high-speed compressors through the use of correlation integral. *Journal of Turbomachinery*, 121 (4):743–750.

[Bright et al., 1997] Bright, M., Qammar, H., Weigl, H., and Paduano, J. (1997). Stall precursor identification in high-speed compressor stages using chaotic time series analysis methods. *Journal of Turbomachinery*, 119:491–499.

[Brun et al., 2014] Brun, K., Nored, M., and Kurz, R. (2014). Impact of piping impedance and acoustic characteristics on centrifugal compressor surge and operating range. *Journal of Engineering for Gas Turbines and Power*, 137(3).

[Bunde and Havlin, 2009] Bunde, A. and Havlin, S. (2009). *Encyclopedia of Complexity and Systems Science*, chapter A Brief Introduction to Fractal Geometry, pages 3700–3720. Springer, Berlin, Heidelberg, New York.

[Coleman and Steele, 2009] Coleman, H. and Steele, W. (2009). *Experimentation, Validation, and Uncertainty Analysis for Engineers*. John Wiley & Sons, Inc., 3rd edition.

[Cormerais et al., 2009] Cormerais, M., Chesse, P., and Hetet, J.-F. (2009). Turbocharger heat transfer modeling under steady and transient conditions. *International Journal of Thermodynamics*, 12(4):193–202.

[Cumpsty, 2004] Cumpsty, N. (2004). *Compressor Aerodynamics*. Krieger Publishing Company.

[De Jager, 1995] De Jager, B. (1995). Rotating stall and surge control: A survey. In *Proceedings of the 34th Conference on Decision & Control New Orleans, LA - December 1995*.

[Dean and Senoo, 1960] Dean, R. and Senoo, Y. (1960). Rotating wakes in vaneless diffusers. *Journal of Basic Engineering*, 82(3):563–570.

[Dean and Young, 1977] Dean, R. and Young, L. (1977). The time domain of centrifugal compressor and pump stability and surge. *Journal of Fluids Engineering*, 99 (1):53–59.

[Dehner et al., 2013] Dehner, R., Figurella, N., Selamet, A., Keller, P., Becker, M., Tallio, K., Miazgowicz, K., and Wade, R. (2013). Instabilities at the low-flow range of a turbocharger compressor. *SAE International Journal of Engines*, 6.

[Dehner et al., 2011] Dehner, R., Selamet, A., Keller, P., and Becker, M. (2011). Prediction of surge in a turbocharger compression system vs. measurements. *SAE International Journal of Engines*, 4 (2).

[Dehner et al., 2016] Dehner, R., Selamet, A., Keller, P., and Becker, M. (2016). Simulation of deep surge in a turbocharger compression system. *Journal of Turbomachinery*, 138:111002.

[Denton, 1993] Denton, J. (1993). The 1993 igti scholar lecture: Loss mechanisms in turbomachines. *Journal of Turbomachinery*, 115(4):621–656.

[Eckardt, 1975] Eckardt, D. (1975). Instantaneous measurements in the jet-wake discharge flow of a centrifugal compressor impeller. *Journal of Engineering for Gas Turbines and Power*, 97 (3):337–345.

[Eckardt, 1976] Eckardt, D. (1976). Detailed flow investigations within a high-speed centrifugal compressor impeller. *Journal of Fluids Engineering*, 98(3):390–399.

[Eckardt, 1979] Eckardt, D. (1979). Flow field analysis of radial and backswept centrifugal compressor impellers part i: Flow measurements using a laser velocimeter. In *Performance Prediction of Centrifugal Pumps and Compressors; Proceedings of the 25th Annual International Gas Turbine Conference and Exhibit and 22nd Annual Fluids Engineering Conference, New Orleans, La., March 9-13, 1980.*

[Eckert and Schnell, 1961] Eckert, B. and Schnell, E. (1961). *Axial- und Radialkompressoren.* Springer, 2nd edition.

[Eigen, 2016] Eigen (2016). Eigen template library. http://eigen.tuxfamily.org. Retrieved 2016-10-21.

[Emmons et al., 1955] Emmons, H., Pearson, C., and Grant, H. (1955). Compressor surge and stall propagation. *Transactions of the ASME*, pages 455–469.

[European Commission, 2017] European Commission (2017). Climate action: Reducing co2 emissions from passenger cars.

[Figurella et al., 2015] Figurella, N., Dehner, R., Selamet, A., Miazgowicz, K., Karim, A., and Host, R. (2015). Effect of aerodynamically induced pre-swirl on centrifugal compressor acoustics and performance. *SAE International Journal of Passenger Cars - Mechanical Systems*, 8(3):995–1002.

[Fink et al., 1992] Fink, D., Cumpsty, N., and Greitzer, E. (1992). Surge dynamics in a free-spool centrifugal compressor system. *Journal of Turbomachinery*, 114:321–332.

[Frigne and van den Braembussche, 1984] Frigne, P. and van den Braembussche, R. (1984). Distinction between different types of impeller and diffuser rotating stall in a centrifugal compressor with vaneless diffuser. *Journal of Engineering for Gas Turbines and Power*, 106:468–474.

[Frigne and van den Braembussche, 1985] Frigne, P. and van den Braembussche, R. (1985). A theoretical model for rotating stall in the vaneless diffuser of a centrifugal compressor. *Journal of Engineering for Gas Turbines and Power*, 107:507–513.

[Galindo et al., 2011] Galindo, J., Arnau, F. J., Tiseira, A., Lang, R., Lahjaily, H., and Gimenes, T. (2011). Measurement and modeling of compressor surge on engine test bench for different intake line configurations. SAE Technical Paper 2011-01-0370, Universidad Politecnica de Valencia.

[Galindo et al., 2008] Galindo, J., Serrano, J. R., Climent, H., and Tiseira, A. (2008). Experiments and modelling of surge in small centrifugal compressor for automotive engines. *Experimental Thermal and Fluid Science*, 32:818–826.

[Galindo et al., 2005] Galindo, J., Serrano, J. R., Guardiola, C., and Cervello, C. (2005). Surge limit definition in a specific test bench for the characterization of automotive turbochargers. *Experimental Thermal and Fluid Science*, 30:449–462.

[Galvas, 1974] Galvas, M. (1974). Fortran program for predicting off-design performance of centrifugal compressors. Technical report, NASA Technical Note D-7487, NASA Lewis Research Center, Cleveland, Ohio, USA.

[Gancedo, 2014] Gancedo, M. (2014). *Effect of Self Recirculation Casing Treatment on the Performance of a Turbocharger Centrifugal Compressor*. PhD thesis, School of Aerospace Systems, College of Engineering and Applied Science, University of Cincinatti, OH, USA.

[Gancedo et al., 2012] Gancedo, M., Guillou, E., Gutmark, E., and Mohamed, A. (2012). Dynamic features and their propagation in a centrifugal compressor housing with ported shroud. SAE Technical Paper 2012-01-0706, SAE Technical Paper 2012-01-0706.

[Gouldin, 1987] Gouldin, F. (1987). An application of fractals to modeling premixed turbulent flames. *Combustion and Flame*, 68(3):249–266.

[Gouldin et al., 1989] Gouldin, F., Bray, K., and Chen, J.-Y. (1989). Chemical closure model for fractal flamelets. *Combustion and flame*, 77(3):241–259.

[Gravdahl and Egeland, 1999] Gravdahl, J. T. and Egeland, O. (1999). Centrifugal compressor surge and speed control. *IEEE Control Systems*, 7(5):567–579.

[Gravdahl et al., 2004] Gravdahl, J. T., Willems, F., De Jager, B., and Egeland, O. (2004). Modeling of surge in free-spool centrifugal compressors: Experimental validation. *Journal of Propulsion and Power*, 20:849–857.

[Greitzer, 1976a] Greitzer, E. (1976a). Surge and rotating stall in axial compressors i: Theoretical compression system model. *Journal of Engineering for Gas Turbines and Power*, 98:190–198.

[Greitzer, 1976b] Greitzer, E. (1976b). Surge and rotating stall in axial compressors ii: Experimental results and comparison with theory. *Journal of Engineering for Gas Turbines and Power*, 2:199–211.

[Greitzer, 1981] Greitzer, E. (1981). The stability of pumping systems - the 1981 freeman scholar lecture. *Journal of Fluids Engineering*, 103:194–242.

[Greitzer et al., 2004] Greitzer, E., Tan, C., and Graf, M. (2004). *Internal Flow - Concepts and Applications*. Cambridge University Press.

[Guillou, 2011] Guillou, E. (2011). *Flow Characterization and Dynamic Analysis of a Radial Compressor with Passive Method of Surge Control*. PhD thesis, Department of Aerospace Engineering and Engineering Mechanics, University of Cincinnati.

[Gysling, 1993] Gysling, D. (1993). *Dynamic Control of Rotating Stall in Axial Flow Compressors Using Aeromechanical Feedback*. PhD thesis, Gas Turbine Laboratory, Massachussets Institute of Technology, Cambridge, MA, USA.

[Hamberg et al., 2015] Hamberg, R., Linschoten, P., Puttige, A., and Reddy, G. (2015). Surge detection using knock sensors in a heavy duty diesel engine. Project report, Department of Machine Design, KTH Royal Institute of Technology.

[Hamberg et al., 2017] Hamberg, R., Linschoten, P., Puttige, A., Reddy, G., Cronhjort, A., and Stenlåås, O. (2017). Surge detection using knock sensors in a heavy duty diesel engine. In *Submitted to the 13th International Conference on Engines and Vehicles, Capri, Italy, 10-14 September*.

[Hansen et al., 1981] Hansen, K., Joergensen, P., and Larsen, P. (1981). Experimental and theoretical study of surge in a small centrifugal compressor. *Journal of Fluids Engineering*, 103(3):391–395.

[Harley et al., 2013] Harley, P., Spence, S., Filsinger, D., Dietrich, M., and Early, J. (2013). Assessing 1d loss models for the off-design performance prediction of automotive turbocharger compressors. In *ASME Paper GT2013-94262, Proceedings of the ASME Turbo Expo 2013, San Antonio, TX, USA, June 3-7*.

[Heneghan and McDarby, 2000] Heneghan, C. and McDarby, G. (2000). Establishing the relation between detrended fluctuation analysis and power spectral density analysis for stochastic processes. *Physical Review E*, 62 (5).

[Howard and Lennemann, 1971] Howard, J. and Lennemann, E. (1971). Measured and predicted secondary flows in a centrifugal impeller. *Journal of Engineering for Power*, 93:126–132.

[Hurst, 1951] Hurst, H. (1951). Long-term storage capacity of reservoirs. *Transactions of the American Society of Civil Engineers*, 116 (1):770–799.

[Ihlen, 2012] Ihlen, E. (2012). Introduction to multifractal detrended analysis in matlab. *Frontiers in Physiology*, 3.

[Jansen, 1964] Jansen, W. (1964). Rotating stall in a radial vaneless diffuser. *Journal of Basic Engineering*, 86 (4):750–758.

[Japikse and Baines, 1998] Japikse, D. and Baines, N. (1998). *Diffuser Design Technology*. Concepts ETI.

[Japikse et al., 2006] Japikse, D., Marscher, W., and Furst, R. (2006). *Centrifugal Pump Design and Performance*. Concepts NREC, White River Junction, VT, USA.

[Johnston, 1973] Johnston, J. (1973). The suppression of shear layer turbulence in rotating systems. *Journal of Fluids Engineering*, 95(2):229–235.

[Johnston and Dean, 1966] Johnston, J. and Dean, R. (1966). Losses in vaneless diffusers of centrifugal compressors and pumps. *Journal of Engineering for Power*, 88(1):49–60.

[Kabral et al., 2013] Kabral, R., Rammal, H., and Åbom, M. (2013). Acoustical methods for investigating turbocharger flow instabilities. SAE Technical Paper 2013-01-1879, KTH Royal Institute of Technology.

[Kantelhardt, 2011] Kantelhardt, J. (2011). *Mathematics of Complexity and Dynamical Systems*, chapter Fractal and Multifractal Time Series, pages 463–487. Springer, New York.

[Karim et al., 2015] Karim, A., Miazgowicz, K., and Lizotte, B. (2015). Automotive turbochargers compressor onset of surge prediction using computational fluid dynamics. SAE Technical Paper 2015-01-1280, Ford Motor Co.

[Kerres, 2012] Kerres, B. (2012). Numerische untersuchung der clocking-effekte einer in den passagen-diffusor einer radialverdichterstufe eingetauchten tandemrückführbeschaufelung. Master's thesis, Institute of Jet Propulsion and Turbomachinery, RWTH Aachen University.

[Kerres et al., 2016a] Kerres, B., Cronhjort, A., and Mihaescu, M. (2016a). Experimental investigation of upstream installation effects on the turbocharger compressor map. In *Proceedings of the IMechE 12th International Conference on Turbochargers and Turbocharging, London, UK, 17-18 May.*

[Kerres et al., 2017a] Kerres, B., Mihaescu, M., Gancedo, M., and Gutmark, E. (2017a). Optimal pressure based detection of compressor instabilities using the hurst exponent. *SAE International Journal of Engines*, 10(4).

[Kerres et al., 2016b] Kerres, B., Nair, V., Cronhjort, A., and Mihaescu, M. (2016b). Analysis of the turbocharger compressor surge margin using a hurst-exponent-based criterion. *SAE International Journal of Engines*, 9(3).

[Kerres et al., 2017b] Kerres, B., Nair, V., and Kabral, R. (2017b). The hurst exponent as a model-free precursor of centrifugal compressor surge. submitted to ASME Journal of Turbomachinery.

[Kerres et al., 2017c] Kerres, B., Sanz, S., Sundström, E., and Mihaescu, M. (2017c). A comparison of performance predictions between 1d models and numerical data for a turbocharger compressor. In *Proceedings of the 12th European Turbomachinery Conference, Stockholm, Sweden, April 3-7.*

[Kinoshita and Senoo, 1985] Kinoshita, Y. and Senoo, Y. (1985). Rotating stall induced in vaneless diffusers of very low specific speed centrifugal blowers. *Journal of Engineering for Gas Turbines and Power*, 107:514–519.

[Kämmer and Rautenberg, 1982] Kämmer, N. and Rautenberg, M. (1982). An experimental investigation of rotating stall flow in a centrifugal compressor. In *Proceedings of the ASME 1982 International Gas Turbine Conference and Exhibit*, volume 1: Turbomachinery.

[Kämmer and Rautenberg, 1986] Kämmer, N. and Rautenberg, M. (1986). A distinction between different types of stall in a centrifugal compressor stage. *Journal of Engineering for Gas Turbines and Power*, 108:83–92.

[Korpela, 2011] Korpela, S. (2011). *Principles of Turbomachinery.* Wiley and Sons, Hoboken, NJ.

[KPMG, 2017] KPMG (2017). Global automotive executive survey 2017. online.

[Lennemann and Howard, 1970] Lennemann, E. and Howard, J. (1970). Unsteady flow phenomena in rotating centrifugal impeller passages. *Journal of Engineering for Power*, 92:65–72.

[Lieblein et al., 1953] Lieblein, S., Schwenk, F., and Broderick, R. (1953). Diffusion factor for estimating losses and limiting blade loadings in axial-flow-compressor blade elements. NACA research memorandum.

[Little, 2006] Little, M. (2006). Fastdfa. http://www.maxlittle.net/software/. Retrieved 2017-01-30.

[Little et al., 2006] Little, M., McSharry, P., Moroz, I., and Roberts, S. (2006). Nonlinear, biophysically-informed speech pathology detection. In *Proceedings of the ICASSP, Toulouse, France, 2006, pp. II-1080-II-1083.*

[Mandelbrot, 1967] Mandelbrot, B. (1967). How long is the coast of britain? statistical self-similarity and fractional dimension. *Science*, 156(3775):636–638.

[Mandelbrot, 1985] Mandelbrot, B. (1985). Self-affinity and fractal dimension. *Physica Scripta*, 32:257–260.

[Mandelbrot, 1988] Mandelbrot, B. (1988). Limit lognormal multifractal measures. In Gotsman, E., Ne'eman, Y., and Voronel, A., editors, *Frontiers of Physics: Proceedings of The Landau Memorial Conference, Tel Aviv, Israel, 6-10 June*, pages 308–340.

[Marelli et al., 2016] Marelli, S., Carraro, C., Moggia, S., and Capobianco, M. (2016). Effect of circuit geometry on steady flow performance of an automotive turbocharger compressor. *Energy Procedia*, 101:630–637.

[Marelli et al., 2017] Marelli, S., Gandolfi, S., and Capobianco, M. (2017). Heat transfer effect on performance map of a turbocharger turbine for automotive application. SAE Technical Paper 2017-01-1036.

[Mizuki et al., 1978] Mizuki, S., Kawashima, Y., and Ariga, I. (1978). Investigation concerning rotating stall and surge phenomena within centrifugal compressor channels. In *Proceedings of the ASME 1978 International Gas Turbine Conference, London, UK, April 9-13, 1978*, volume 1A: General.

[Moore, 1973] Moore, J. (1973). A wake and an eddy in a rotating, radial-flow passage part 1: Experimental observations. *Journal of Engineering for Gas Turbines and Power*, 95 (3):205–212.

[Nair and Sujith, 2014] Nair, V. and Sujith, R. (2014). Multifractality in combustion noise: Predicting an impending combustion instability. *Journal of Fluid Mechanics*, 747:635–655.

[Nair et al., 2013] Nair, V., Thampi, G., Karuppusamy, S., Gopalan, S., and Sujith, R. (2013). Loss of chaos in combustion noise as a precursor of impending combustion instability. *International journal of spray and combustion dynamics*, 5(4):273–290.

[Oh et al., 1997] Oh, H., Yoon, E., and Chung, M. (1997). An optimum set of loss models for performance prediction of centrifugal compressors. *Proceedings of the IMechE, Part A: Journal of Power and Energy*, 211(4):331–338.

[Peng et al., 1994] Peng, C.-K., Buldyrev, S. V., Havlin, S., Simons, M., Stanley, H. E., and Goldberger, A. L. (1994). Mosaic organization of dna nucleotides. *Physical Review E*, 49:1685–1689.

[Pischinger, 2013a] Pischinger, S. (2013a). *Internal Combustion Engines 1 Lecture Notes*. Professorial Chair for Combustion Engines, RWTH Aachen University.

[Pischinger, 2013b] Pischinger, S. (2013b). *Internal Combustion Engines 2 Lecture Notes*. Professorial Chair for Combustion Engines, RWTH Aachen University.

[SAE, 1995a] SAE (1995a). J1826: Turbocharger gas stand test code.

[SAE, 1995b] SAE (1995b). J922: Turbocharger nomenclature and terminology.

[Schäfer et al., 2016] Schäfer, C., Sandor, I., Klaus, M., and Baar, R. (2016). Influence of the hot gas test bench piping system on the surge line of an automotive turbocharger compressor. In *Proceedings of the 12th International Conference on Turbochargers and Turbocharging, London, UK, May 17-18*.

[Schlichting and Gersten, 2017] Schlichting, H. and Gersten, K. (2017). *Boundary-Layer Theory*. Springer, Berlin, Heidelberg, New York, 9th edition.

[Schneider et al., 2015] Schneider, M., Bühler, J., Hanna, M., Leichtfuß, S., and Schiffer, H.-P. (2015). Analytical loss prediction for turbocharger compressors. In *Proceedings of the 11th European Conference on Turbomachinery Fluid dynamics and Thermodynamics, ETC11, Madrid, Spain, March 23-27*.

[Schröder, 2004] Schröder, W. (2004). Fluidmechanik.

[Semlitsch and Mihaescu, 2016] Semlitsch, B. and Mihaescu, M. (2016). Flow phenomena leading to surge in a centrifugal compressor. *Energy*, 103:572–587.

[Senoo et al., 1979] Senoo, Y., Hayami, H., Kinoshita, Y., and Yamasaki, H. (1979). Experimental study on flow in a supersonic centrifugal impeller. *Journal of Engineering for Power*, 101:32–39.

[Senoo and Kinoshita, 1977] Senoo, Y. and Kinoshita, Y. (1977). Influence of inlet flow conditions and geometries of centrifugal vaneless diffusers on critical flow angle for reverse flow. *Journal of Fluids Engineering*, 99 (1):98–102.

[Senoo and Kinoshita, 1978] Senoo, Y. and Kinoshita, Y. (1978). Limits of rotating stall and stall in vaneless diffuser of centrifugal compressors. In *Proceedings of the ASME 1978 International Gas Turbine Conference, London, UK, April 9-13, 1978*.

[Serrano et al., 2013] Serrano, J. R., Margot, X., Tiseira, A., and Garcia-Cuevas, L. (2013). Optimization of the inlet air line of an automotive turbocharger. *International Journal of Engine Research*, 14:92–104.

[Shaaban and Seume, 2012] Shaaban, S. and Seume, J. (2012). Impact of turbocharger non-adiabatic operation on engine volumetric efficiency and turbo lag. *International Journal of Rotating Machinery*.

[Skoch, 2003] Skoch, G. (2003). Experimental investigation of centrifugal compressor stabilization techniques. In *Proceedings of the ASME Turbo Expo 2003, Atlanta, GA, USA, June 16-19, 2003*.

[Skoch, 2005] Skoch, G. (2005). Experimental investigation of diffuser hub injection to improve centrifugal compressor stability. *Journal of Turbomachinery*, 127:107–117.

[Sreenivasan, 1991] Sreenivasan, K. (1991). Fractals and multifractals in fluid turbulence. *Annu. Rev. Fluid Mechanics*, 23:539–604.

[Sreenivasan and Meneveau, 1986] Sreenivasan, K. and Meneveau, C. (1986). The fractal facets of turbulence. *Journal of Fluid Mechanics*, 173:357–386.

[Sreenivasan and Meneveau, 1988] Sreenivasan, K. and Meneveau, C. (1988). Singularities of the equations of fluid motion. *Physics Review A*, 38:6287–6295.

[Staudacher et al., 2004] Staudacher, M., Telser, S., Amann, A., Hinterhuber, H., and Ritsch-Marte, M. (2004). A new method for change-point detection developed for on-line analysis of the heart beat variability during sleep. *Physica A: Statistical Mechanics and its Applications*, 349:582–596.

[Sundström et al., 2016] Sundström, E., Kerres, B., and Mihaescu, M. (2016). Evaluation of centrifugal compressor performance models using large eddy simulation data. In *Proceedings of the ASME 2016 Turbo Expo Turbomachinery Technical Conference & Exposition, Seoul, South Korea, 13-17 June.*

[Sundström et al., 2017] Sundström, E., Kerres, B., Sanz, S., and Mihaescu, M. (2017). On the assessment of centrifugal compressor parameters by theoretical and computational models. In *Proceedings of the ASME Turbo Expo 2017: Turbomachinery Technical Conference and Exposition, June 26-30, Charlotte, NC, USA*, number GT2017-65230.

[The Mathworks, Inc., 2016] The Mathworks, Inc. (2016). Matlab documentation.

[Theotokatos and Kyrtatos, 2001] Theotokatos, G. and Kyrtatos, N. P. (2001). Diesel engine transient operation with turbocharger compressor surging. SAE Technical Paper 2001-01-1241, National Technical University of Athens.

[Toyama et al., 1977] Toyama, K., Runstadler, P., and Dean, R. (1977). An experimental study of surge in centrifugal compressors. *Journal of Fluids Engineering*, 99:115–131.

[Traupel, 1982] Traupel, W. (1982). *Thermische Turbomaschinen: Zweiter Band. Geanderte Betriebsbedingungen, Regelung, Mechanische Probleme, Temperaturprobleme.* Springer Verlag, Berlin, Heidelberg, New York, 3 edition.

[Traupel, 2001] Traupel, W. (2001). *Thermische Turbomaschinen: Erster Band. Thermodynamisch-strömungstechnische Berechnung.* Springer Verlag, Berlin, Heidelberg, New York, 4 edition.

[van den Braembussche, 2013] van den Braembussche, R. (2013). *Centrifugal Compressor Analysis and Design*. Von Karman Insitute for Fluid Dynamics.

[Venkatramani et al., 2017] Venkatramani, J., Nair, V., Sujith, R., Gupta, S., and Sarkar, S. (2017). Multi-fractality in aeroelastic response as a precursor to flutter. *Journal of Sound and Vibration*, 386:390–406.

[Watson and Janota, 1982] Watson, N. and Janota, M. (1982). *Turbocharging the Internal Combustion Engine*. Springer, New York, Heidelberg, Berlin.

[Westin, 2005] Westin, F. (2005). *Simulation of turbocharged SI-engines - with focus on the turbine*. PhD thesis, KTH Industrial Engineering and Management.

[Yoshinaka, 1977] Yoshinaka, T. (1977). Surge responsibility and range characteristics of centrifugal compressors. In *Proceedings of the 1977 Tokyo Joint Gas Turbine Congress*.

A DFA Performance

The most computationally expensive part of DFA is the calculation and removal of the local trends for each chunk. The trends are calculated using least-square fit. The algorithm was implemented in MATLAB at first. A straightforward implementation using the built-in `polyfit()` and `polyval()` functions of Eq. (3.15) and Eq. (3.17) would thus look like this (see also [Ihlen, 2012]):

```
SE = zeros (Ns, 1);
% v counts through all segments of size w
for v = 1 : Ns
    idx = (v-1)*w+1 : v*w;          % Indices in Y vector
    Yv = Y(idx);

    % Detrending (order m)
    p1 = polyfit (idx, Yv, m);
    % Sum of squared error of the segment
    SE(v) = sum((Yv - polyval(p1, idx)).^2) / w;
end
% Average over all segments and store in fluctuation function matrix
qidx = 1;
for q = qvector
    if q ~= 0
        F2(widx, qidx) = (mean(SE.^(q/2))).^(1/q);
    else
        F2(widx, qidx) = exp(1/2*mean(log(SE)));
    end
    qidx = qidx + 1;
end
```

However, the performance can be significantly improved by avoiding the repeated execution of many steps in the least-square fit algorithm. MATLABs `polyfit(x,y,m)` algorithm [The Mathworks, Inc., 2016] creates a Vandermonde matrix $\mathbf{V}$

$$\mathbf{V} = \left(\mathbf{x}^m \ \mathbf{x}^{m-1} \ ... \ \mathbf{x}^0\right) \tag{A.1}$$

where $\mathbf{x}$ is a column vector and the power operator operates element-wise. The condition number of the matrix $\mathbf{V}$ is estimated and its QR decomposition is computed as

$$\mathbf{V} = \mathbf{QR} \tag{A.2}$$

with $\mathbf{Q}$ being a unitary matrix and $\mathbf{R}$ an upper triangular matrix. The polynomial coefficients $\mathbf{p}$ are the computed for each segment by

$$\mathbf{p} = \mathbf{R}^{-1}(\mathbf{Q}^T\mathbf{y}) \tag{A.3}$$

In the example code above, $\mathbf{V}$ thus consists of the powers of the indices `idx`. This is not optimal both from a numerical accuracy and computational efficiency point of view. From a numerical point of view, $\mathbf{V}$ might become badly conditioned for high indices $\mathbf{x}$ and high orders m. From a computational efficiency point of view, it is unnecessary to compute $\mathbf{V}$ for every call of `polyval()`. Since we're only interested in the error between the data and the trend, $\tilde{Y}$, we can choose any linearly spaced vector $\mathbf{x}$. A good choice here also eliminates the need for an estimate of the condition number. A much faster implementation of DFA would therefore look for example like this:

```
SE = zeros (Ns, 1);
% Create evenly spaced vector x
x = linspace (-1, 1, w);
% Create Vandermonde matrix
V = zeros (w, m+1);
V(:,m+1) = ones (w, 1);
for j = m:-1:1
   V(:,j) = x .* V(:,j+1);
end
% QR decomposition
[Q,R] = qr (V, 0);

% v counts through all segments of size w
for v = 1 : Ns
    idx = (v-1)*w+1 : v*w;          % Indices in Y vector
    Yv = Y(idx);

    % Detrending (order m)
    p1 = R \ (Q'*Yv);                    % Polyfit coefficients
    SE(v) = sum ((Yv - V*p1).^2) / w;    % Sum of squared error
end

% Average over all segments and store in fluctuation function matrix
qidx = 1;
for q = qvector
    if q ~= 0
        F2(widx, qidx) = (mean(SE.^(q/2))).^(1/q);
    else
        F2(widx, qidx) = exp(1/2*mean(log(SE)));
    end
    qidx = qidx + 1;
end
```

From the code snippets above, we can also see that calculating the set of generalized Hurst exponents $H^{(q)}$ is not much more computationally intensive than calculating only $H^{(2)}$, since the detrending does not have to be repeated. Using a

higher order of detrending m, on the other hand, increases the computational cost since Eq. (A.3) becomes more expensive. Equation A.3 is executed once per segment.

B Errata

Paper I and Paper V

The signal power in these papers should be calculated according to Eq. (2.58):

$$P = 10 \cdot \log_{10} \left(\frac{1}{p_{\text{ref}}^2} \int_{\omega_s - \Delta\omega}^{\omega_s + \Delta\omega} S_{xx} \mathrm{d}\omega \right) \text{ [dB]} , \tag{B.1}$$

where the reference pressure is stated as $p_{\text{ref}} = 20\,\mu\text{Pa}$. However, it was forgotten to square the reference pressure in the actual calculation. Therefore, all signal power values given in these papers are too low by a difference of

$$\Delta P = 10 \cdot \log_{10} \left(20 \cdot 10^{-6} \right) \approx 47\,\text{dB} . \tag{B.2}$$

Alternatively, the values are correct if a reference pressure of

$$p_{\text{ref}} = \sqrt{20 \cdot 10^{-6}}\,\text{Pa} \approx 4.472\,\text{mPa} \tag{B.3}$$

is assumed. Since these values are only compared to each other, the outcome of the analyses is not affected.